UNIVERSITÀ DEGLI STUDI DI PADOVA
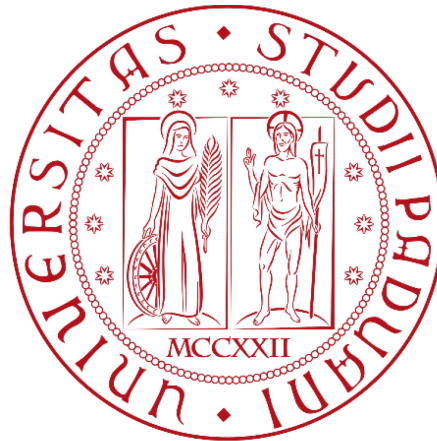
Department of

Civil, Environmental, and Architectural Engineering

Water and Geological Risk Engineering Program

Master Thesis

Modeling Land Subsidence and Fault Reactivation Due to Groundwater Pumping in the Alaşehir-Sarıgöl Sub-Basin, Turkey.

Can Yuksel

(2042279)

Supervisor

Prof. Eng. Pietro Teatini

Department of Civil, Environmental and Architectural Engineering

Co-Supervisor

Dr. Andrea Franceschini

Department of Civil, Environmental and Architectural Engineering

Academic Year 2023/2024

Acknowledgments

I would like to express my deepest gratitude to my supervisor, Prof. Eng. Pietro Teatini, whose expertise, understanding, and patience have greatly enriched my graduate experience. I appreciate his vast knowledge and skills in many areas and his help in writing this thesis.

I also thank my co-supervisor, Dr. Andrea Franceschini, for his invaluable guidance, encouragement, and insightful suggestions throughout my research. His advice and feedback were instrumental in refining my work and achieving my research goals.

I extend my special thanks to Dr. Yueting Li, whose support and assistance were instrumental in my research. Her help and guidance often exceeded expectations, and I am deeply grateful for her contributions.

Finally, I would like to thank my family, especially my mother and father, for their unconditional love and support. Their belief in me has been a constant source of inspiration and has given me the confidence to pursue and complete this thesis.

Abstract

The Gediz River basin in Turkey (GBS) and its Alaşehir-Sarıgöl sub-basin (ASSB) are highly valuable for agriculture due to the presence of river sediments. Heavy agricultural irrigation has resulted in significant water stress in ASSB, leading to reduced groundwater levels, aquifer compaction, and land subsidence. It is important to note that there are primary and secondary faults present in ASSB as well. Tectonic movements have a significant impact on the ASSB area. Sentinel-1 SAR images taken between 2016 and 2020 have revealed a significant land subsidence in ASSB, with maximum rates of over 5 cm/year, affecting both urban areas and farmland. Subsided areas are visible in particular in the Alaşehir-Sarıgöl plain, mostly in the eastern part of the study area, where land subsidence is accompanied by earth fissuring). This research investigates the relationship between pressure changes, land subsidence, and aseismic fault reactivation. The pressure evolution in the aquifer system over the past decade has been investigated based on available piezometric records and previous modeling analyses and the continuous (i.e., land subsidence) and discontinuous (i.e., earth fissures) displacement fields in the studied region have been simulated using the GEPS3D simulator, a three-dimensional geomechanical model developed at the Department of ICEA, Padova University. The final aim is to understand if the observed earth fissures are likely associated with anthropogenic activities, i.e. aquifer over-exploitation, or aseismic fault sliding due to natural tectonic regime. The modeling results allow us to conclude that the observed earth fissures are most likely due to anthropogenic activities, specifically aquifer over-exploitation. This comprehensive understanding will aid in developing better management strategies to mitigate land subsidence and its associated risks in the ASSB.

Table of Contents

List of Figure

List of Table

Chapter 1

1. Introduction

The Gediz River Basin (GRB) in Turkey, particularly its Alaşehir-Sarıgöl sub-basin (ASSB), is a region of substantial agricultural importance due to its fertile river sediments. However, this area is experiencing significant environmental challenges due to human activities. Agriculture is the dominant economic activity in the area, accompanied by secondary activities such as animal husbandry, industrial production, geothermal energy production, and mining, along with hosting densely populated municipalities (Çakmak, et al., 2018).This practice has led to notable water stress, resulting in decreased groundwater levels, which is thought to cause aquifer compaction and, therefore consequent land subsidence and earth fissures.

One of the most pervasive hydrogeological phenomena induced by human activity over the 20th century is land subsidence due to groundwater withdrawal, which has had a significant impact on numerous major cities and regions worldwide (Herrera-García, et al., 2021). In some peculiar geological settings, land subsidence is also accompanied by the aseismic rupture of the land surface, the so-called earth fissure. The generation and propagation of ruptures requires the development of failure conditions, that is, tensile and/or shear stress not supported by shallow alluvial sediments. Stress fields of these kinds have been documented by several modeling analyses aimed at understanding the rupture occurrence at specific sites in Mexico ((Carreón-Freyre, et al., 2016; Ochoa-González, et al., 2018), China (Ye, et al., 2018; Li, et al., 2021) and Nevada (Hernandez-Marin & Burbey, 2010) and Arizona (Jachens & Holzer, 1979) (Jachens & Holzer, 1982) in the USA. Understanding the generation of earth fissures and modeling their occurrence and propagation is still today far to be achieved. The density, shape, length, depth, aperture, and dislocation of the fissures vary greatly between areas. In some places, only a few isolated fissures have formed, whereas elsewhere many fissures occur. Arizona's fissures total about 170 miles today. (AZGS, 2015). Up to 15 km long, 1–2 m wide, 15–20 m deep, and more than 2 m vertically dislocated fissures have been reported.

Türkiye is situated on the Anatolian microplate in the eastern Mediterranean, a region renowned for its complex tectonic activity. The interaction between the Anatolian microplate and three adjacent plates—the Eurasian, African, and Arabian plates—has resulted in significant

deformations and tectonic activity, including earthquakes, especially along the North Anatolian Fault Zone (Navarro-Hernández, et al., 2023; Tatar, et al., 2012). The Alaşehir-Sarıgöl sub-basin (ASSB), located within the Gediz River Basin (GRB), is one of the aforementioned tectonic valleys. Situated in western Türkiye, it developed from regional extension horst-graben systems. The geological complexity of the ASSB, with its primary and secondary faults, serves to exacerbate these issues, rendering the region highly susceptible to tectonic influences.

Poyraz et al. (2019) employed GNSS benchmarks to assess vertical displacements at various valley locations between 2013 and 2015. Their findings revealed a maximum displacement rate of -90 mm/year along the Sarıgöl fault. Furthermore, Poyraz and Hastaoğlu (2020) Utilized TerraSAR-X synthetic aperture radar (SAR) images obtained between May 2014 and November 2015 to monitor the valley using interferometric synthetic aperture radar (InSAR). They observed a maximum displacement rate of -50 mm/year in the line of sight (LOS) direction. Previous research indicates that groundwater extraction may have contributed to some of the land subsidence observed in the region. It is not possible to attribute the subsidence solely to tectonic creep movement (Navarro-Hernández, et al., 2023). Land subsidence affects both urban and agricultural zones, particularly in the eastern part of the Alaşehir-Sarıgöl plain, manifesting as ground fissuring and earth slicing. These changes pose significant risks to the region's infrastructure and agricultural productivity.

The relationship between land subsidence, pressure changes, and earth fissures in the absence of significant tectonic plate movements remains a critical area of study. Previous research has highlighted the importance of understanding these dynamics in order to develop effective management strategies for subsurface resources and to mitigate associated risks. Franceschini et al. (2016) introduced a novel Lagrangian approach for the stable numerical simulation of fault and fissure mechanics, emphasizing the importance of reliable discontinuous geomechanical models in predicting fault behaviors due to groundwater withdrawal. In addition, Navarro-Hernández et al. (2023) addressed the topic of monitoring land subsidence caused by groundwater extraction and tectonic activity in the study area. This emphasizes the necessity of integrated techniques that consider hydrological and geomechanical aspects. Moreover, the utilization of geomechanical simulations, such as the GEPS3D simulator developed at the Department of ICEA at the University of Padua, has been demonstrated to be of significant value in the simulation of displacement fields and the comprehension of the long-term geophysical alterations in these areas.

The objective of this study is to gain a deeper understanding of the intricate interactions that occur within the ASSB between pressure fluctuations, land subsidence, and aseismic earth fissures occurring along the projection of deeper fault systems. By utilizing the GEPS3D simulator to simulate the land displacement fields over the past decades, this study aims to elucidate the underlying mechanisms driving these changes and contribute to the development of strategies for sustainable groundwater management and land subsidence mitigation.

The structure of this thesis is as follows: Chapter 1 introduces the study, outlining its background, objectives, and significance. Chapter 2 provides a detailed description of the study area, including its geological-hydrostratigraphic properties, tectonic activities, and land use patterns. Then, the mathematical and numerical models used to describe and solve the flow and geomechanical problems are introduced in Chapter 3. In Chapter 4, the application of the geomechanical model is presented, with a focus on mesh definition. The model calibrations and results obtained from the model simulations are discussed in Chapter 5. Chapter 6 provides a comprehensive discussion of the findings and presents the conclusions drawn from the study. Finally, the references and appendices are included for further reading and detailed data supporting this study.

Chapter 2

2. Site Description

The Gediz River Basin is one of the most important and stressed river basins in Turkey and it is located in the Aegean region between 26° 42' - 29° 45' eastern longitude and 38° 04' - 39° 13' northern latitude coordinates. It has a catchment area of 17034 km^2 and covers about 2.2% of Turkey's total land area. The basin extends from Manisa to Pamukkale and the Gediz River, which has given its name to the basin, is located here for about 400 km. The river comes from several large springs in Mount Murat, which is northeast of the basin, and Mount Bozdağ, which is 2159 m above sea level. The river finally discharges into the Aegean Sea after passing through a variety of morphological settings and lush agricultural areas. Figure 2.1 shows a topographical map of the GRB. It is the largest of Turkey's 25 legally recognized watersheds. (Elçi, et al., 2015).

Figure 2.1. Map of the Gediz River Basin, the alluvial aquifer (Elçi, et al., 2015)

The region has a typical Mediterranean climate with hot, dry summers and relatively cold winters. The basin experiences an average annual temperature of 15.6C and precipitation of 635 mm (Yılmaz & Atmaca, 2017). Agriculture dominates land use in this part of the basin, covering

over 80% of the area. Vineyards represent the main crop type, occupying approximately 70% of the cultivated surface. The main residential areas are concentrated in Salihli, Alaşehir, Yeşilyurt, and Sarıgöl, with a population of over 250,000 inhabitants. The continuous urban fabric covers approximately 1.8 km^2, and the discontinuous urban fabric covers 1542 km^2 (Navarro-Hernández, et al., 2023; Copernicus, 2018).

2.1. Study Area

The reference pilot site (borders are determined by the RESERVOIR project) (Figure 2.2) is located in the eastern portion of the GRB alluvial aquifer, which is characterized by extensive and abundant groundwater in some areas. The alluvial aquifer is mainly developed in the west-northwest and east–southeast directional Gediz graben areas. The GRB alluvial aquifer accounts for a significant portion of the total groundwater potential of the basin (DSI, 2014).

The study area is located in the Sarıgöl district between mountain ranges in the northeast and southwest, which are roughly 10 km apart and have boundaries in the northwest and southeast transecting the Sarıgöl Plain.
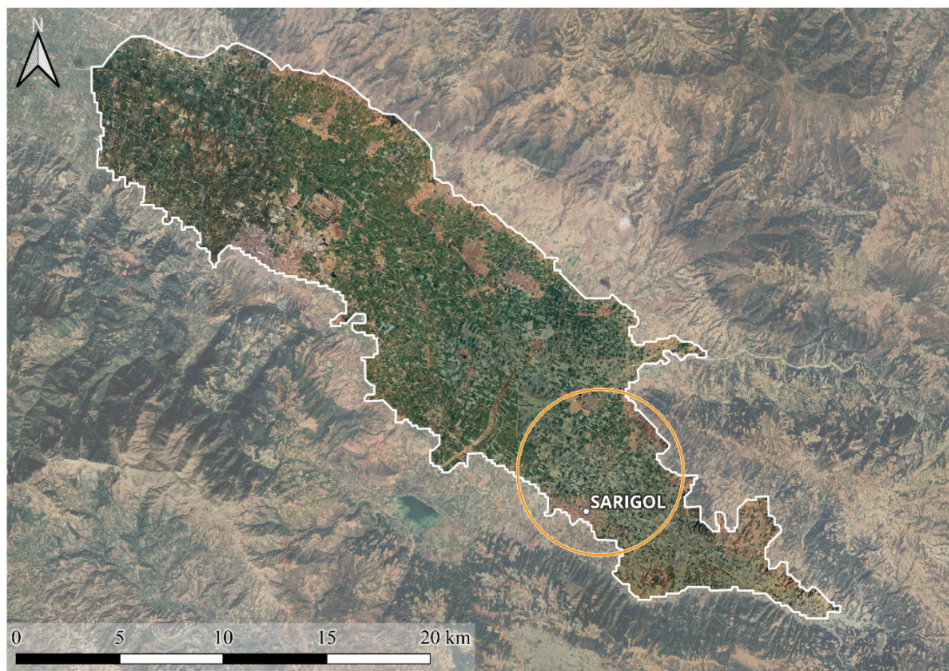
Figure 2.2 GRB alluvial basin. White polygon: border of reference pilot area. Orange polygon: study area.

The study area was determined following a field visit in November 2023. During the field trip, the locations of the most visible points of earth fissures were recorded and photographs were taken. Figure 2.3 illustrates the path created by the locations of each photograph in Figure 2.4. The photographs demonstrate that the land has been displaced significantly, resulting in notable differential movement of the ground level.

Figure 2.3. Locations of earth fissure photos.

Figure 2.4. Visible earth fissure photos from Sarıgöl district (photos by Can Yüksel, 2023)

The processing of Sentinel-1 SAR images between 2016 and 2020 using the P-SBAS method has revealed an important land subsidence in the Alaşehir-Sarıgöl sub-basin (Turkey), with maximum rates of more than 5 cm/year. Navarro-Hernández at. al. (2023) show that the computed vertical displacement is displayed in Figure 2.5-a, with most of the displacement occurring within the basin and centered at the southeast boundary. In the meantime, the regional tectonic trend is towards the west (points in red and orange) and is associated with the continental crustal Aegean expansion, as depicted in Figure 2.5-b. The measuring stations are in both the mountains and the sub-basin. All these measurement spots are situated within the graben, and the points shown in blue indicate east horizontal displacement. Given that most of these displacements occur along dip angle faults, it is possible that they are connected to a local tectonic process related to the history of the Gediz Graben.
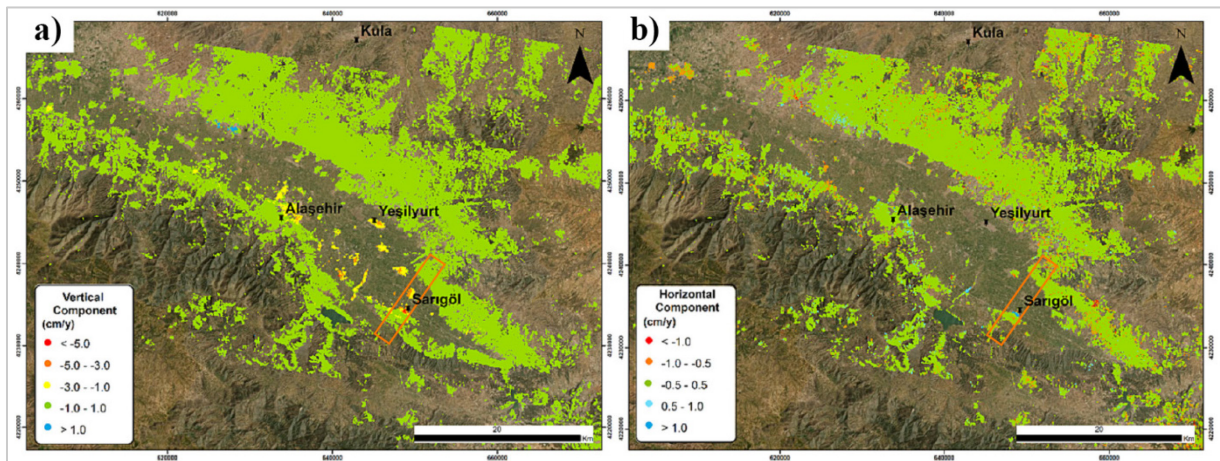
Figure 2.5. P-SBAS displacement rates. Vertical displacement rates V_u (a) and east-west horizontal displacement rates, V_e (b) (Navarro-Hernández, et al., 2023). The orange polygon represents the study area.

2.2. Geological Properties

The study area is located within the Gediz Graben, also known as the Alaşehir Graben. This graben has a WNW-ESE directional arc-shaped structural pattern, with a length of 140 km and a width of 10-15 km. It is located in the Western Anatolian region and is characterized by active tectonic extension, which has resulted in the formation of North-South trending grabens and normal faults that bound these grabens (Sözbilir, 2002).

The study area is located in the Gediz Graben, one of the best-developed and morphologically well-defined grabens in Western Anatolia (Üner & Dogan, 2021). The light-yellow color in Figure 2.5 indicates the Quaternary material filling the basin (uppermost unit). This material consists mainly of fluvial sediments from the present-day Gediz River. On the other hand, the Neogene (Miocene and Pliocene) filling of the basin refers to sedimentary sequences consisting of fluvial-alluvial, alluvial-fan, debris- and clay-rich intervals of very low permeability (Navarro-Hernández, et al., 2023). The rock units in the Gediz Basin consist of two main groups: the basement and sedimentary cover (Hacıoğlu, et al., 2021).
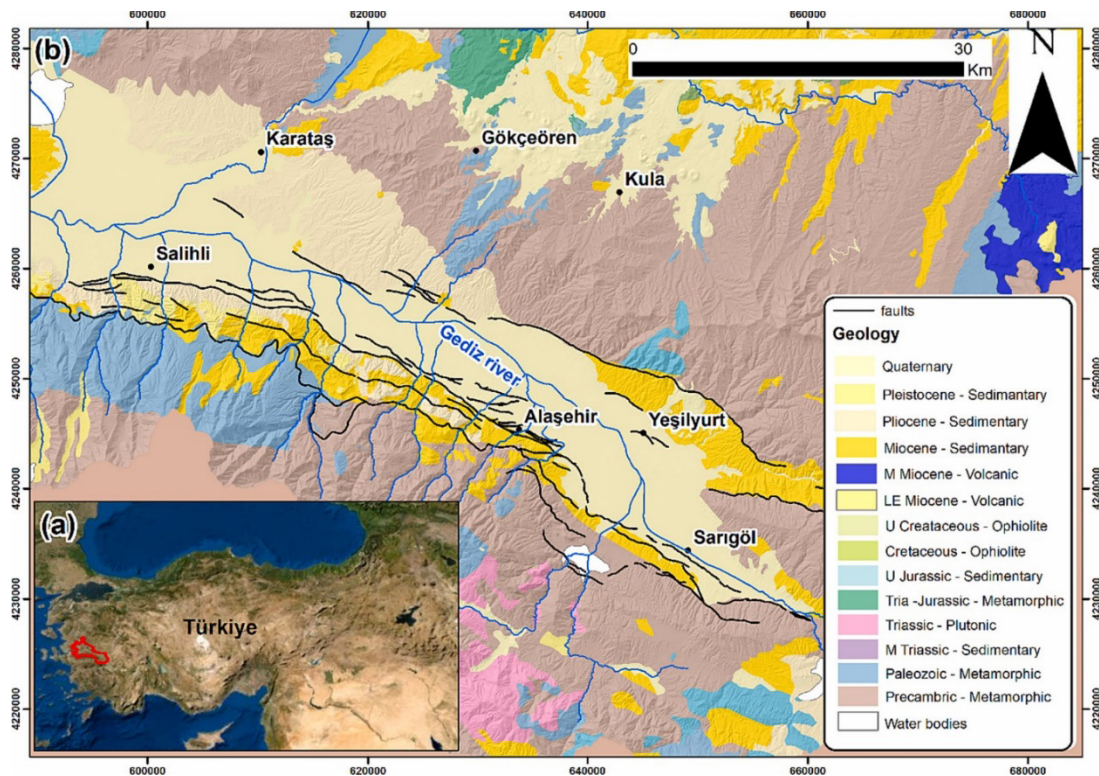
Figure 2.6: (a) Location of the ASSB (red polygon). (b) Geological map of the study area with delineation of regional faults. (Navarro-Hernández, et al., 2023)

The Pre-Neogene basement (i.e. Menderes Massif) is made up of metamorphic rocks and is overlain by Neogene-Quaternary sedimentary cover up to 2-3 km thick. The Gediz detachment fault is a major fault that separates the metamorphic basement in the footwall from the older Miocene fill in the hanging wall (Hacıoğlu, et al., 2021). The basement mainly consists of spotted gneiss at the bottom and various types of schist. Gneiss is mostly found on the hanging part of the horst south of Sarıgöl, Alaşehir, and Salihli, while schists are located south of Salihli and Alaşehir and east of Urganlı (Yılmazer, et al., 2010).

The plain is covered by unconsolidated deposits from the Quaternary period. The sedimentary sequences in the basin consist mainly of lacustrine, fluvial-alluvial, alluvial-fan, and debris-flow deposits from the lower Miocene to the lower Pliocene, as well as fluvial, lacustrine, alluvial units, and travertine from the Pliocene to the Quaternary (Hacıoğlu, et al., 2021; Seyitoğlu, et al., 2000). Some clay-rich intervals in the Neogene Basin have very low permeability, which makes them suitable as cap rocks for geothermal systems in the area. The graben fill comprises of three formations. The oldest and lowest formation is the Alaşehir Formation, which consists of conglomerates, sandstones, siltstones, and organic-rich shales. The uppermost units are Quaternary alluviums, which are made up of fluvial sediments.

These deposits consist of clay, clayey sands, and gravel (Seyitoğlu, et al., 2000) and can reach a thickness of up to 320 m in the study area. Figure 2.7 shows an isopach map indicating the thickness of the alluvial layer (Bonì, et al., 2022).
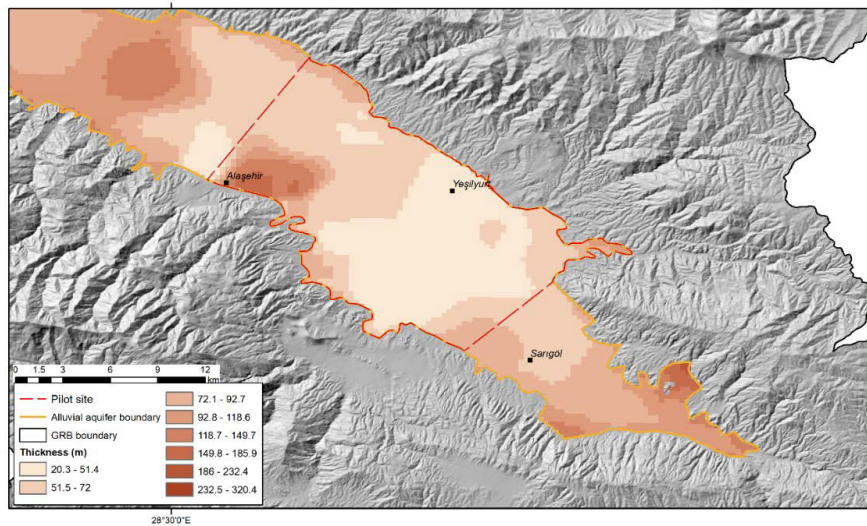
Figure 2.7: Thickness of alluvial layer in GRB study area (Bonì, et al., 2022).

2.3. Tectonic and Seismic and Aseismic Activities

Turkey is situated within the Alpine-Himalayan orogenic belt, which is a seismic belt. Turkey is one of the most seismically active regions globally, with a high level of seismic activity and it is influenced by the movement of tectonic plates relative to each other, including the Eurasian-African-Arabian plate. As a result, Turkey is undergoing a complex structural process and rapid tectonic deformation (Poyraz & Hastaoğlu, 2020).

The Horst-Graben morphology-dominated West Anatolia region, which includes Gediz Graben, is being controlled by oblique-slip normal faults (Figure 2.9) that are causing the geological formations to extend at a rate of approximately 2.5–3.0 cm per year in the north-east to south-west direction (Arikan, et al., 2010). The region of Western Anatolia has a history of experiencing destructive earthquakes, which have played a role in the development of numerous civilizations. A total of approximately thirteen earthquakes have been documented in the surrounding area over the historical era (F., et al., 2019). For example, the Salihli earthquake in 1965, with a magnitude of 5.8, the Alaşehir earthquake in 1969, with a magnitude of 6.5, and the Gediz earthquake in 1970, with a magnitude of 7.2 (Selim & Yanik, 2009). The Gediz Graben is part of the Aegean Horst Graben system, bounded to the south by the currently inactive low angle (~10∘) Gediz detachment fault, which is the most important structural element of the system, separating the Neogene sediments from the metamorphic basement corresponding to the Menderes Massif (Navarro-Hernández, et al., 2023; F., et al., 2019). A second structural and important element in the study area are the E-W oriented high angle oblique and active faults that cross the detachment faults (Sözbilir, 2002; Üner & Dogan, 2021) as a result of the development of the Horst Graben system. Currently, most of the seismic activity occurs along these faults (Navarro-Hernández, et al., 2023; Poyraz & Hastaoğlu, 2020).

The unconsolidated young alluvial, fluvial, and lacustrine sediments and the dominant active normal faults that control these sediments form the Western Anatolian Extension Zone, one of the most suitable areas in the world for the development of aseismic surface deformation (F., et al., 2019; Özkaymak, et al., 2017). Over the past 20 years, the Sarıgöl-Manisa region (Gediz Graben) in the Western Anatolian Extension Zone has shown evidence of surface deformation that has evolved without devastation. It is known that seismic deformation still occurs along the faults that control the southwestern part of the Gediz Graben. As a result of the lowering of groundwater levels due to human activities, the unconsolidated sediments below the surface are compressed and cause settlement-related deformations that, geometrically controlled by the fault planes at depth, can result in surface aseismic ruptures of the land surface with consequences on the urban structures and infrastructures (Figure 2.8) (Koca, et al., 2011).

Figure 2.8. Damage to buildings in the Sarıgöl district caused by earth fissure (photos by Can Yüksel, 2023).

Figure 2.9. Part of the active fault map for Western Anatolia. The red outline represents part of the Gediz Graben, which includes the study area (Emre, et al.).

13

2.4. Hydrostratigraphic Setting

The hydrostratigraphic setting of the valley has been characterized by a number of boreholes and geophysical sections scattered throughout the valley (Navarro-Hernández, et al., 2023). The multi-aquifer comprises five hydrogeological units. Beginning from the top, the uppermost layer (L1) represents a permeable unconfined aquifer consisting of silty sand materials. Layer L2, situated beneath L1, comprises clays and sandy clay materials, forming a confining layer. The subsequent aquifer layer (L3) is permeable, and primarily composed of sand and gravel. Below L3, layer L4 acts as a confining layer made up of sandy clay. The deepest aquifer unit (L5) is a clayey gravel layer. This representation of the alluvial system has been used in the RESERVOIR Project funded by the EU (Elçi, et al., 2022) to develop a groundwater flow model of the entire valley (Figure 2.10).
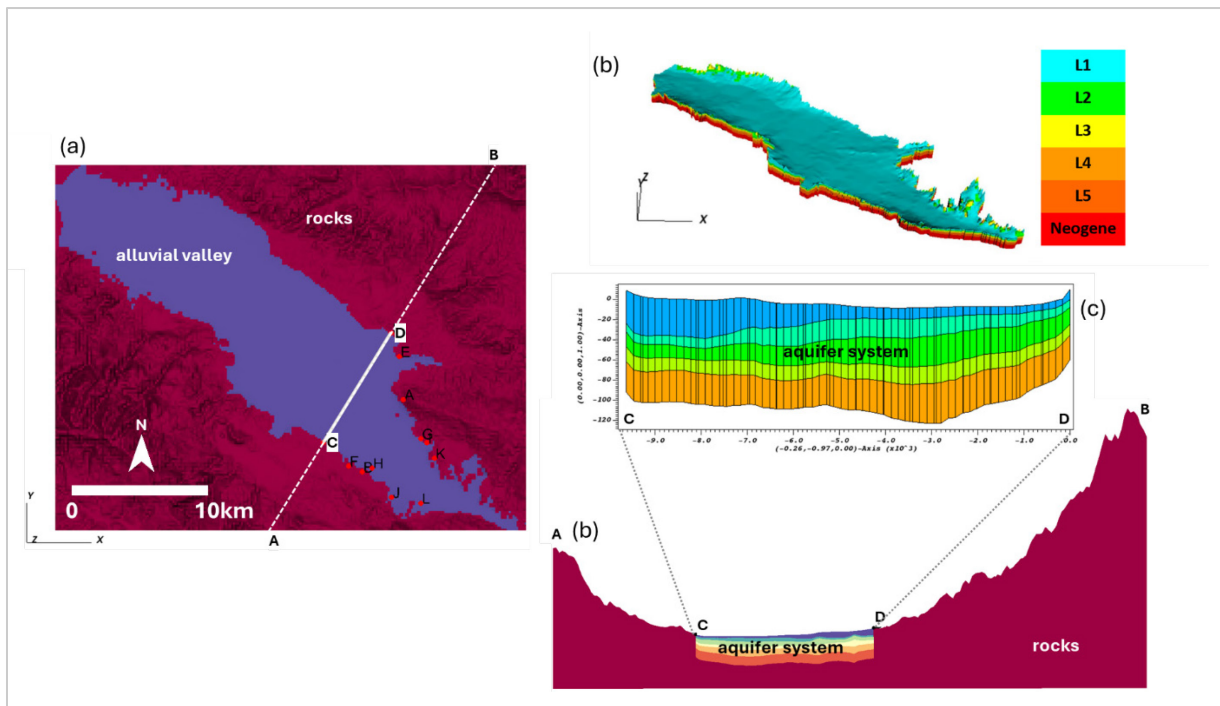
Figure 2.10. Hydrogeological setting of the GRB aquifer system. (a): Horizontal view of compressible (alluvial valley) and incompressible (rocks) materials. (b) Vertical section of the domain along alignment AB depicted in (a). (c) Aquifer system layering, and discretization as implemented in a basin-scale groundwater flow model developed by Elçi et al. (2022) along alignment CD depicted in (b). (d) Basin-scale reconstruction of the alluvial aquifer system as represented in Elçi et al. (2022).

The objective of representing the complex mechanics associated with fissure generation as a consequence of fault reactivation accompanying groundwater pumping has necessitated the use of more detailed stratigraphic representations. This has been achieved through geophysical acquisitions conducted within the valley and, in particular, across the Sarıgöl Plain. Figure 2.6-b demonstrates the presence of faults at depth running almost parallel to the mountain foothills, along the southern boundary of the alluvial valley. Specifically, the outcomes of two surveys are available:

1) Hydrogeologic section based on geoelectrical acquisitions (Figure 2.11)
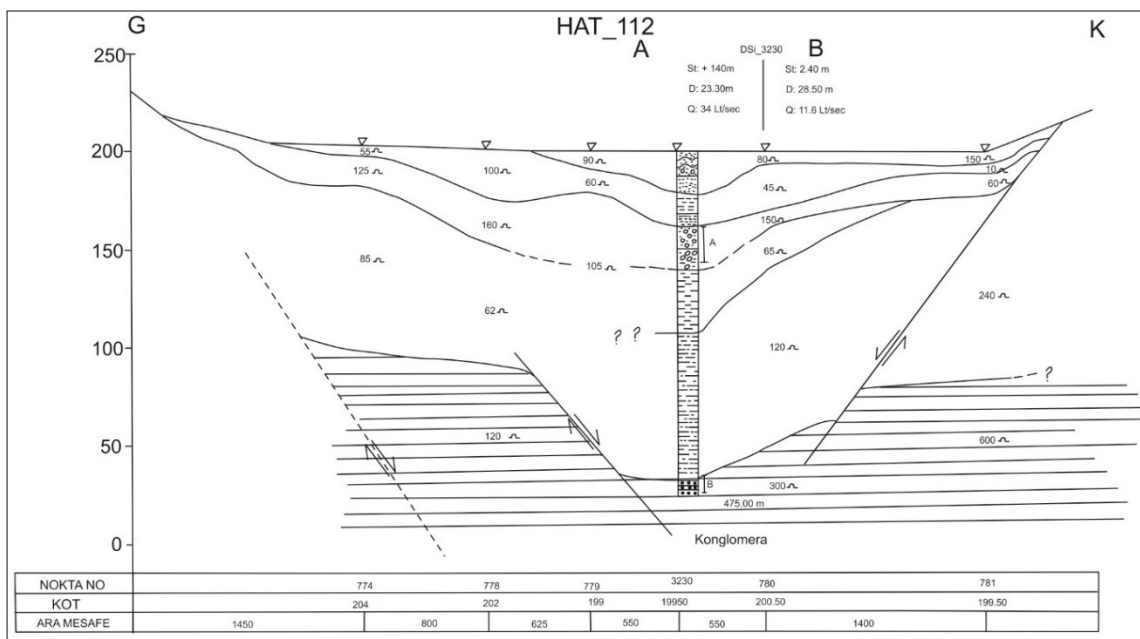
Figure 2.11. Layer profile from hydrogeoelectrical survey conducted in the Alaşehir-Sarıgöl Plain (DSI, 2014).

The borehole drilling log was analyzed in detail to develop stratigraphic profiles for the study area, which further facilitated the identification of conceptual model layers. Figure 2.12 illustrates the scanned images of the drilling logs.

15

Figure 2.12. Groundwater borehole profile (log) for well no:3230 (DSI, 2014).

2) Geologic section based on a seismic survey (Figure 2.13)
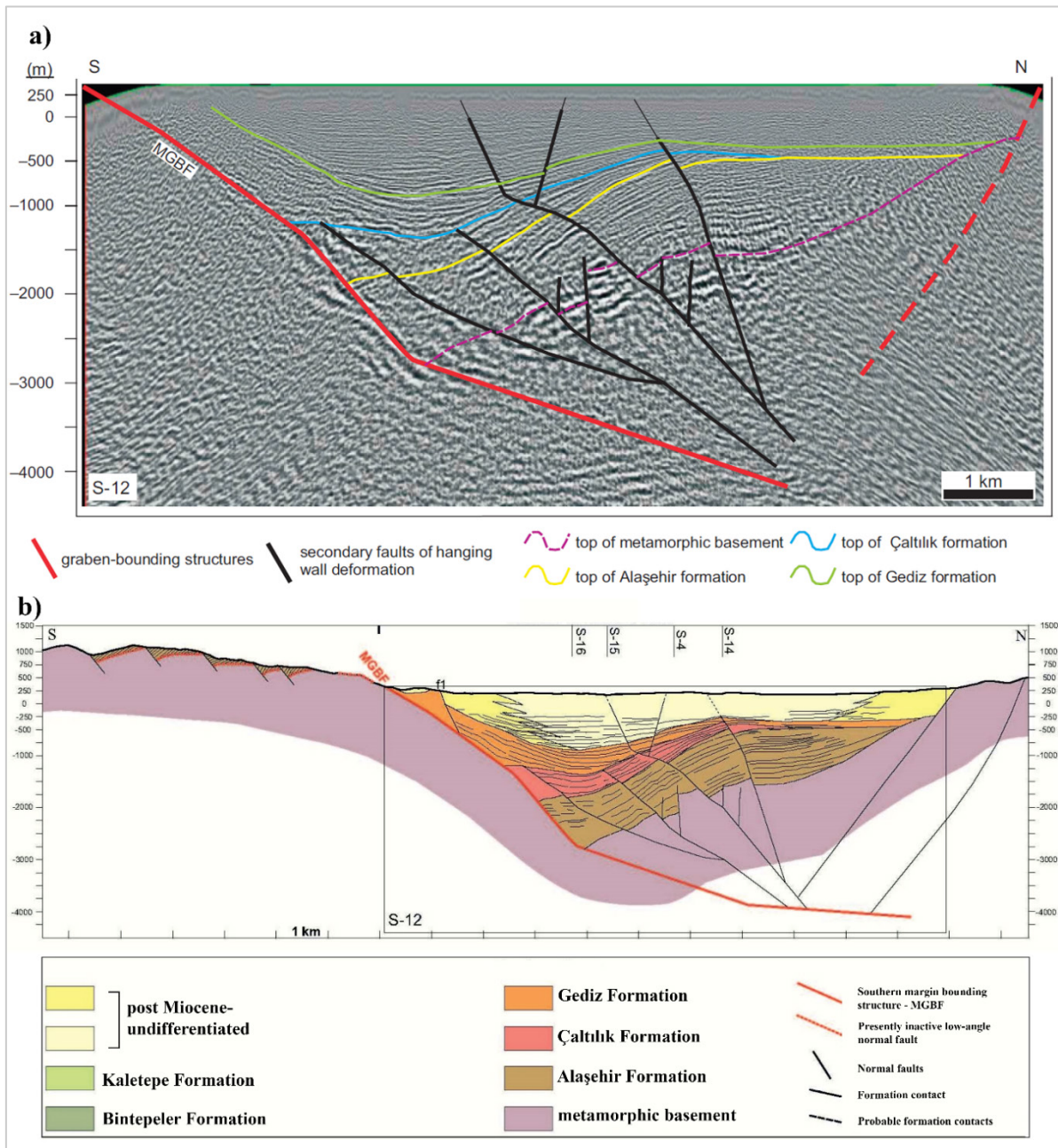
Figure 2.13. Transverse geological cross-section portraying the architecture of the Gediz Graben. a) The interpreted seismic reflection profile. b) The geologic interpretation (Ciftci & Bozkurt, 2010).

Both the hydrogeological section based on geoelectrical surveys (Figure 2.11) and the geological section based on a seismic survey (Figure 2.13) present cross sections of the subsurface with dipping layers that vary in thickness and are disrupted by faults, using vertical exaggeration to highlight geological features and clearly label layers and faults. However, the

hydrogeological section focuses on shallow subsurface layers and does not show faults extending to the surface. This makes it less useful for studies of faults. In contrast, the geological section from the seismic survey provides a deeper profile and clearly delineates major faults that extend to the surface at steep angles. This could make the seismic survey more valuable for understanding fault mechanics and the potential for fissures.

2.5. Land Use

The Gediz River Basin in Turkey is a region characterized by diverse land use and significant economic activities that impact its environment. In 2016, 483 thousand people were living in the countryside inside the GRB's borders, and 1.34 million people living in towns and cities. The basin is also a hub for other economic activities, including animal husbandry, the food industry, textile manufacturing, geothermal energy production, and mining. The quantity and quality of groundwater resources are significantly impacted by these activities, as well as by natural processes. Figure 2.14 illustrates the registered pumping wells for GRB, 52 of which are for irrigation (estimated average groundwater discharge rate: 74.71 Mm^3/year) and 66 of which are for public water supply (estimated average groundwater discharge rate: 6.952 Mm^3/year). Figure 2.15 displays the land use distribution based on the CORINE-2018 database. The following is a breakdown of land use classes for the entire basin: lands and semi-natural areas make up 45% (761,972 ha), wetlands make up 0.3% (381 ha), water bodies make up 0.8% (12,965 ha), and agricultural areas make up 52% (894,546 ha). Artificial surfaces make up 2% (34,093 ha). The area is primarily used for agriculture within the limits of the alluvial aquifer (Bonì, et al., 2022).
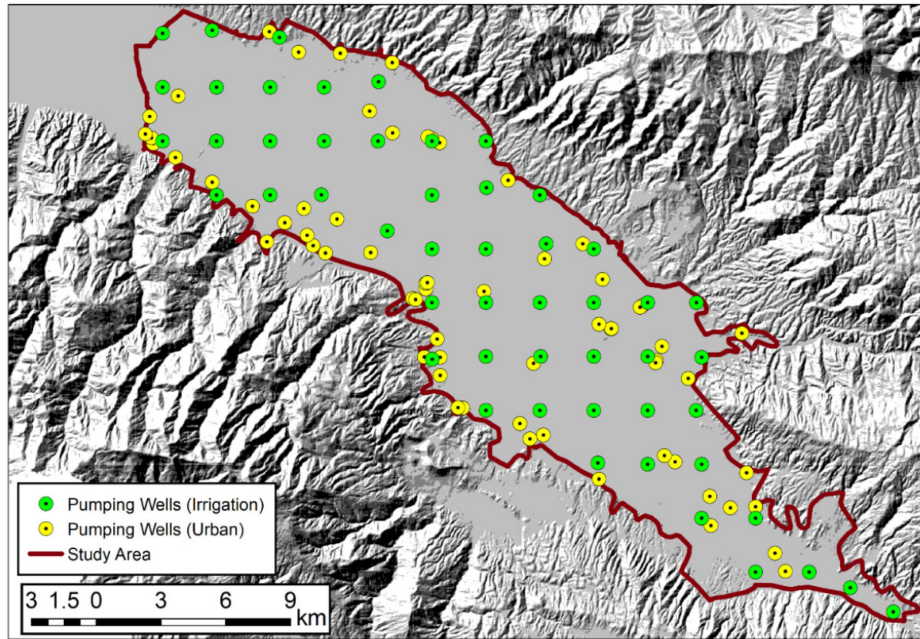
Figure 2.14. Location of pumping wells as defined in the GRB flow model developed in the RESERVOIR Project (Elçi, et al., 2022)
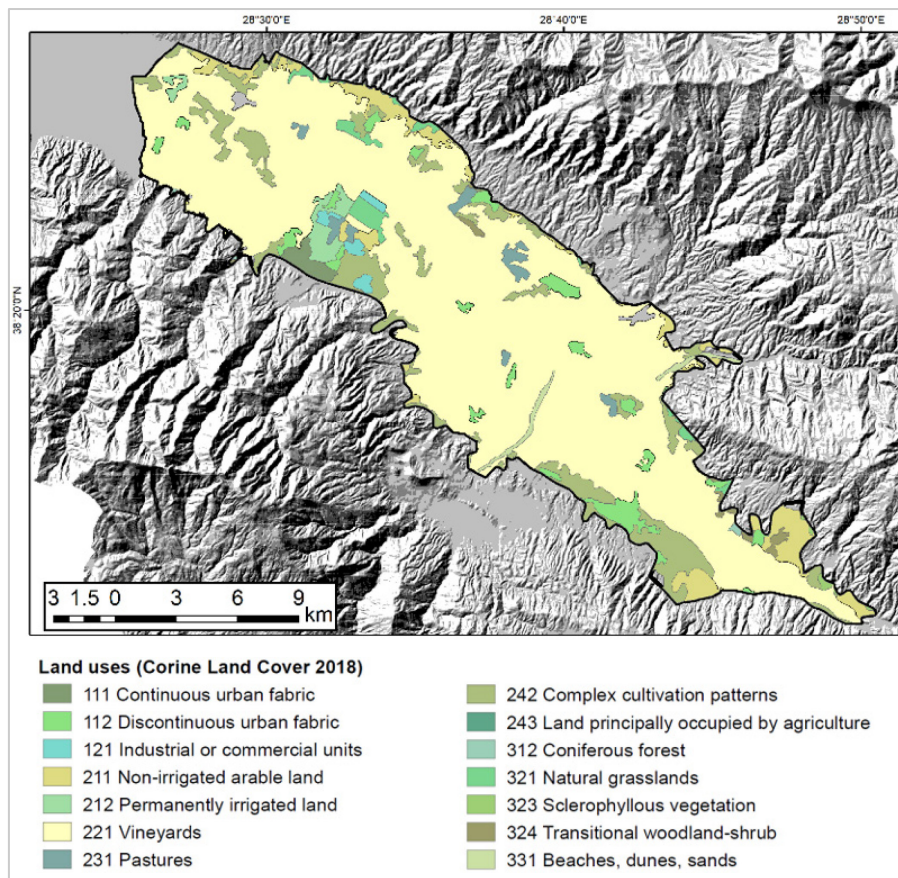
Figure 2.15. Land use coverage in the model domain area based on the CORINE-2018 database (Bonì, et al., 2022).

Chapter 3

3. Theory and Methods

3.1. Poro-Elasticity

In the field of materials science, a porous medium is defined as a material that contains interconnected pores or voids, allowing the passage of fluids, whether gases or liquids. The properties of porous media, including pore size distribution, porosity, and permeability, significantly impact fluid flow behaviors within them. These versatile materials have applications across various disciplines, including hydrology, geology, engineering, and environmental science. Therefore, soil can be considered a porous medium.

Poro-elasticity is a branch of mechanics that concerns materials with a solid matrix and fluid phase that deform elastically while allowing fluid flow through their porous structure. It relies on porosity to quantify the volume fraction not occupied by solid constituents. This concept is of great importance in disciplines such as civil engineering and hydrogeology, as it provides a framework for understanding how fluids and solids interact mechanically. The volumetric fractions of solid and fluid phases, as studied by poro-elasticity, offer insights into the coupled behavior of these materials. The notion of pore space within a solid frame or skeleton that can be filled with an arbitrary fluid is the basis of the term "poro-elasticity", which was coined by Geertsma (1966). The formal foundation of the concept as it is currently employed was, however, established earlier by Biot (1964) from a continuum perspective, building upon the work of Terzaghi (1943; 1943) in the context of soil mechanics and Fillunger (1936) from the standpoint of fundamental concepts of mixture theory (Steeb & Renner, 2019).

The objective of the analysis is to characterize the alterations within the soil volume, specifically in terms of displacements, strains, and stresses across the entire domain. From a mathematical perspective, this means determining the components of the displacement vector and the two tensors representing strains and stresses:

$$\boldsymbol{u} = \begin{bmatrix} u \\ v \\ \omega \end{bmatrix} \quad \epsilon = \frac{1}{2}(\nabla \boldsymbol{u} + \nabla \boldsymbol{u}^T) = \begin{bmatrix} \epsilon_x & \gamma_{yx} & \gamma_{zx} \\ \gamma_{xy} & \epsilon_y & \gamma_{zy} \\ \gamma_{xz} & \gamma_{yz} & \epsilon_z \end{bmatrix} \quad \boldsymbol{\sigma} = \begin{bmatrix} \sigma_x & \tau_{yx} & \tau_{zx} \\ \tau_{xy} & \sigma_y & \tau_{zy} \\ \tau_{xz} & \tau_{yz} & \sigma_z \end{bmatrix} \quad (3.1)$$

The conservation of angular momentum is a fundamental principle in physics that states that the total angular momentum of a system remains constant in the absence of external torques acting on the system. This can be summarized as follows: the tensor is symmetric and composed of six independent terms:

$$\tau_{xy} = \tau_{yx} \qquad \tau_{xz} = \tau_{zx} \qquad \tau_{yz} = \tau_{zy} \qquad (3.2)$$

Consequently, the tensors can be written as the following vectors:

$$\epsilon = [\epsilon_x, \epsilon_y, \epsilon_z, \gamma_{yz}, \gamma_{xz}, \gamma_{xy}]^T \qquad (3.3)$$

$$\sigma = [\sigma_x, \sigma_y, \sigma_z, \tau_{yz}, \tau_{xz}, \tau_{xy}]^T \qquad (3.4)$$

Any alteration to the flux field's circumstances, such as the addition or removal of fluid, causes a strain in the solid matrix as well as a propagation of the perturbation in the fluid itself when the soil is fully saturated. Therefore, the average effective stress in the soil skeleton and the hydrostatic pressure in the voids cause the stresses to act on the water as well as the solid matrix. Terzaghi's effective stress principle describes how the two stages are divided:

$$\hat{\sigma} = \sigma - \alpha p i \qquad (3.5)$$

Where:

- $\hat{\sigma} = [\hat{\sigma}_x, \hat{\sigma}_y, \hat{\sigma}_z, \hat{\tau}_{xy}, \hat{\tau}_{yz}, \hat{\tau}_{xz}]^T$ is the vectorial form of the tensor of total stresses,
- $\sigma = [\sigma_x, \sigma_y, \sigma_z, \tau_{yz}, \tau_{xz}, \tau_{xy}]^T$ is the vectorial form of the tensor of effective stresses,
- α is the Biot's coefficient. This describes the interaction between a porous material and the fluid contained within its pores. It represents the coupling between the solid skeleton and the pore fluid in response to changes in pore pressure. In simple terms, the Biot coefficient quantifies how much the solid matrix of a porous material deforms in response to changes in pore pressure. A Biot coefficient of 1 indicates full coupling between the solid and fluid phases, meaning that changes in pore pressure lead to corresponding deformations in the solid matrix. A Biot coefficient

of 0 signifies the absence of coupling, indicating that changes in pore pressure exert no influence on the solid matrix.

$$\alpha = 1 - \frac{C_r}{C_b} \tag{3.6}$$

Where:
- C_r is the volumetric compressibility of grains,
- C_b is the bulk modulus.
- p is the pore fluid pressure,
- $i = [1, 1, 1, 0, 0, 0]^T$ is the vectorial form of the Kronecker delta.

Terzaghi's principle is important in the context of poro-elasticity theory, as it connects the pore water flow through the soil (which is controlled by pore fluid pressure) with the mechanical behavior of the solid skeleton (which is regulated by effective stress). Poro-elasticity theory can simulate phenomena such as consolidation settlement, where changes in pore water pressure affect the effective stress distribution and vice versa, by considering both the solid and fluid phases (Terzaghi, 1925).

Thus, Terzaghi's principle provides a conceptual framework for understanding the relationship between mechanical deformation and fluid flow when applying poro-elasticity theory to saturated soil problems, ultimately facilitating the analysis and prediction of behaviors such as consolidation settlement.

The usual sign convention is in use: a positive pressure acts normally to and in the direction of the body's surface, whereas a negative stress indicates tension, respectively.

A set of equations is required to completely explain the theory of poro-elasticity. It contains structural equations that describe the equilibrium of the soil as well as the flow equation for a fluid in a porous media. The following subsections provide these models' mathematical justification.

3.1.1. Elastic Equilibrium of the Porous Medium

As mentioned in previous topics, poro-elasticity theory uses a mathematical framework to characterize soil behavior, providing a simplified but effective solution. However, its effectiveness depends on certain assumptions that streamline the analysis while maintaining relevance. Those are:

- The behavior of the soil is linearly elastic. It is assumed that the porous media behaves in a linearly elastic way. It can be described through Hooke's law. This indicates that within the material, the relationship between stress and strain is still linear. Neglect is given to non-linear effects (such as finite deformations),
- It is expected that the porous material is isotropic, meaning that all orientations would experience the same mechanical characteristics (like stiffness).
- It is assumed that the porous medium will undergo small deformations. The governing equations can now be linearized as a result.
- It is assumed that the solid skeleton, or matrix, is incompressible. Deformation-related volume variations are minimal.
- Since Terzaghi's principle is valid, changes in the effective intergranular stress are the only factor influencing the porous matrix's deformation.

Regarding an elementary cubic volume of porous media (Figure 3.1), where the lateral faces are oriented parallel to the direction of the main axis, Terzaghi's principle (3.5) can be employed to characterize the components of the stress tensor:

$$
\begin{array}{lll}
\hat{\sigma}_x = \sigma_x - \alpha p & \hat{\tau}_{yz} = \tau_{yz} & \hat{\tau}_{zy} = \tau_{zy} \\
\hat{\sigma}_y = \sigma_y - \alpha p & \hat{\tau}_{xz} = \tau_{xz} & \hat{\tau}_{zx} = \tau_{zx} \\
\hat{\sigma}_z = \sigma_z - \alpha p & \hat{\tau}_{xy} = \tau_{xy} & \hat{\tau}_{yx} = \tau_{yx}
\end{array}
\qquad (3.7)
$$

Where:

- σ is normal stress, with the index indicating the direction in which it develops.
- τ is the shear stress, the first index indicates the direction normal to the plane containing the elements in question, while the second index indicates the direction along which they develop.
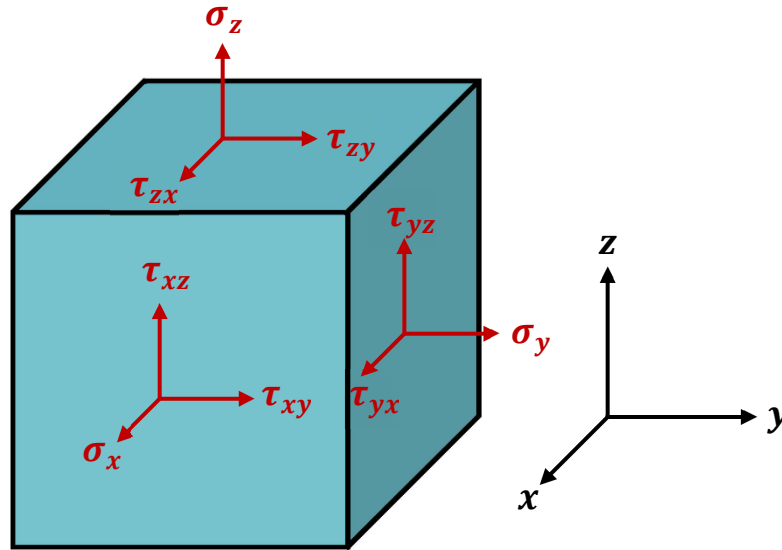
Figure 3.1. Cubic elementary volume with indications of stress components

The volumetric forces and the stresses in the soil need to be balanced. The Cauchy equations can be used to express this relationship.

$$\frac{\partial \hat{\sigma}_x}{\partial x} + \frac{\partial \hat{\tau}_{yx}}{\partial y} + \frac{\partial \hat{\tau}_{zx}}{\partial z} + F_x = 0$$

$$\frac{\partial \hat{\tau}_{xy}}{\partial x} + \frac{\partial \hat{\sigma}_y}{\partial y} + \frac{\partial \hat{\tau}_{zy}}{\partial z} + F_y = 0 \qquad (3.8)$$

$$\frac{\partial \hat{\tau}_{xy}}{\partial x} + \frac{\partial \hat{\tau}_{yz}}{\partial y} + \frac{\partial \hat{\sigma}_z}{\partial z} + F_z = 0$$

Where F_x, F_y and, F_z are three components of the strengths per unit volume.

Each variable shows the increase in stress from the original undisturbed state, assuming that the initial stress tensor is in equilibrium. Additionally, a new system is obtained that is described in terms of effective stresses and pressures by substituting equations (3.7) into equations (3.8):

$$\frac{\partial \hat{\sigma}_x}{\partial x} + \frac{\partial \hat{\tau}_{yx}}{\partial y} + \frac{\partial \hat{\tau}_{zx}}{\partial z} = \alpha \frac{\partial p}{\partial x}$$

$$\frac{\partial \hat{\tau}_{xy}}{\partial x} + \frac{\partial \hat{\sigma}_y}{\partial y} + \frac{\partial \hat{\tau}_{zy}}{\partial z} = \alpha \frac{\partial p}{\partial y} \qquad (3.9)$$

$$\frac{\partial \hat{\tau}_{xy}}{\partial x} + \frac{\partial \hat{\tau}_{yz}}{\partial y} + \frac{\partial \hat{\sigma}_z}{\partial z} = \alpha \frac{\partial p}{\partial z}$$

24

Nonetheless, the flow model's unknowns are stated in terms of displacements rather than stresses. Hooke's law, which applies to isotropic soil, states the relationship between stress and strain as follows:

$$\epsilon_x = \frac{1}{E}\left[\sigma_x - v(\sigma_y + \sigma_z)\right] \qquad\qquad \gamma_{yz} = \frac{\tau_{yz}}{2G}$$

$$\epsilon_y = \frac{1}{E}\left[\sigma_y - v(\sigma_x + \sigma_z)\right] \qquad\qquad \gamma_{xz} = \frac{\tau_{xz}}{2G} \qquad\qquad (3.10)$$

$$\epsilon_z = \frac{1}{E}\left[\sigma_z - v(\sigma_y + \sigma_x)\right] \qquad\qquad \gamma_{xy} = \frac{\tau_{xy}}{2G}$$

Where:

- ϵ_i and γ_{ij} are the strain vector components for the shear and normal stresses, respectively, shown in the equation (3.3),
- E is Young's modulus. It is defined as the ratio of the stress (force per unit area) applied to an object and the resulting axial strain (displacement or deformation) in the linear elastic region of the material (Boresi & Schmidt, 2002),
- v is Poisson's ratio. It is a measure of the Poisson effect, the phenomenon in which a material tends to expand in directions perpendicular to the direction of compression (Boresi & Schmidt, 2002),
- G is the shear modulus. It is the elastic shear stiffness of a material. It quantifies how resistant a material is to shear deformation (sliding or twisting) when subjected to an applied shear stress (McNaught, 1997).

The shear modulus is related to E and v through the formula:

$$G = \frac{E}{2(1 + v)} \qquad\qquad (3.11)$$

Therefore, under the small displacement hypothesis, the strain vector can be written as follows:

$$\begin{bmatrix} \epsilon_x \\ \epsilon_y \\ \epsilon_z \\ \gamma_{yz} \\ \gamma_{xz} \\ \gamma_{xy} \end{bmatrix} = \begin{bmatrix} \dfrac{\partial}{\partial x} & 0 & 0 \\ 0 & \dfrac{\partial}{\partial y} & 0 \\ 0 & 0 & \dfrac{\partial}{\partial z} \\ 0 & \dfrac{\partial}{\partial z} & \dfrac{\partial}{\partial y} \\ \dfrac{\partial}{\partial z} & 0 & \dfrac{\partial}{\partial x} \\ \dfrac{\partial}{\partial y} & \dfrac{\partial}{\partial x} & 0 \end{bmatrix} \begin{bmatrix} u \\ v \\ \omega \end{bmatrix} = Lu \qquad (3.12)$$

Where the L is the first-order differential operator relating strains and displacement.

Equation (3.10) provides the explicit stress components. Next, the elastic equilibrium equations are written in terms of the displacements u, v, and ω are as follows, considering the assumption of small displacements and small strains (Verruijt, 1969):

$$G\nabla^2 u + (\lambda + G)\frac{\partial \epsilon}{\partial x} = \frac{\partial p}{\partial x}$$

$$G\nabla^2 u + (\lambda + G)\frac{\partial \epsilon}{\partial y} = \frac{\partial p}{\partial y} \qquad (3.13)$$

$$G\nabla^2 u + (\lambda + G)\frac{\partial \epsilon}{\partial z} = \frac{\partial p}{\partial z}$$

Where:

- λ is one of the Lamé constants. Which is equal to:

$$\lambda = \frac{vE}{(1 - 2v)(1 + v)} \qquad (3.14)$$

- ∇^2 is the Laplace operator and it is equal to:

$$\nabla^2 = \frac{\partial^2}{\partial x^2} + \frac{\partial^2}{\partial y^2} + \frac{\partial^2}{\partial z^2} \qquad (3.15)$$

The most prevalent assumption in reservoir geomechanics is an isotropic stress-strain relation since, often, only the vertical component of the land displacement or in situ deformation is available for model calibration (Settari, 2008; Teatini, et al., 2000). In the case of an isotropic elastic medium, the constitutive matrix D, as underlined by Teatini et al (2011), which relates the effective stress tensor $\boldsymbol{\sigma}$ to the displacement u via the strain tensor $\boldsymbol{\epsilon}$, is given by:

$$D = \frac{E(1-v)}{(1+v)(1-2v)} \begin{bmatrix} 1 & \dfrac{v}{1-v} & \dfrac{v}{1-v} & 0 & 0 & 0 \\ \dfrac{v}{1-v} & 1 & \dfrac{v}{1-v} & 0 & 0 & 0 \\ \dfrac{v}{1-v} & \dfrac{v}{1-v} & 1 & 0 & 0 & 0 \\ 0 & 0 & 0 & \dfrac{1-2v}{2(1-v)} & 0 & 0 \\ 0 & 0 & 0 & 0 & \dfrac{1-2v}{2(1-v)} & 0 \\ 0 & 0 & 0 & 0 & 0 & \dfrac{1-2v}{2(1-v)} \end{bmatrix} \qquad (3.16)$$

E stands for Young's modulus. The established relationships between c_M and the mechanical parameters E, G, λ, and v are as follows:

$$c_M = \frac{(1+v)(1-2v)}{E(1-v)}, \qquad (3.17)$$

$$c_M = \frac{v}{\lambda(1-v)}, \qquad (3.18)$$

And,

$$c_M = \frac{v}{\lambda(1-v)} \qquad (3.19)$$

3.2. Fault Mechanics

A fault, also known as a ground fracture or a geological fault, can be defined as a discontinuity within a three-dimensional porous substance comprising two friction surfaces in contact with

one another. The contact surface model is generally more appropriate for regional-scale simulations and for characterizing the likely fault activation with the onset of localized discontinuous displacements, while alternative techniques are also conceivable (Jha & Juanes, 2014). In this instance, contact mechanics principles can be employed to elucidate the mechanical behavior of defects.

In general, contact problems arise when portions of the boundary of one body come into contact with portions of the boundary of the same or another body. These contacts are subject to specific restrictions, such as friction and the non-compenetrability of solid bodies, which are described by the governing constitutive law. A fault can be regarded as an inner boundary embedded in a continuous body where a relative displacement between corresponding points is allowed whenever the stress state violates a certain failure criterion. Relative displacements can occur between matching sites when the stress states deviate from a failure criterion, which is often the Coulomb frictional law. In this situation, compenetration is not allowed (Franceschini, et al., 2016).

The acting strength for every point x along the fault can be split into its two components, σ_n and τ_s, which act tangentially and normally to the surface, respectively. The Coulomb failure criterion can therefore be expressed as follows:

$$\tau_s \leq \tau_L = c - \sigma_n \tan\varphi \qquad (3.20)$$

Where φ and c are friction angle and cohesion, respectively, and τ_L is the limit shear stress. Typically, compression is indicated by a negative normal stress. The shear stress. can no longer rise when the equation (3.20) $\tau_s = \tau_L$, and slippage, i.e., a relative surface displacement along the fault plane may happen. Usually, it is considered cautiously that faults are incapable of withstanding tensile strengths so that σ_n cannot be positive. It is possible to represent the friction coefficient φ as a non-linear function of the fault slippage. Usually, laboratory experiments of frictional sliding on rock surfaces serve as the basis for these models. Without this data, it is typical to assume a static friction model in which φ is a constant.

3.3.   Variational Formulation

The virtual work equation can be employed to address the issue of determining the displacement $u(x)$ in equilibrium with a given set of external forces. In instances where the Mohr-Coulomb criterion (3.20) is satisfied, the Lagrange multipliers λ in the context of contact problems physically represent the strengths operating on the discontinuity surfaces and guarantee the continuation of the displacement u across the fault. According to Franceschini et al. (2016), the Lagrange multipliers are defined as the physical strengths operating on the interface between the fault surfaces. In this context, the vectors representing the normal and tangential components of the contact strengths are referred to as $\lambda_n(x)$ and $\lambda_s(x)$, respectively.

In practice two scenarios can occur:

- Since the Coulomb criteria (3.20) is satisfied, the multipliers will guarantee that the displacement $u(x)$ is continuous.

- When either $\tau_s = L$ or $\tau_n = 0$, the Mohr-Coulomb criterion gets violated and the fault strengths are known while the surfaces are free to move.
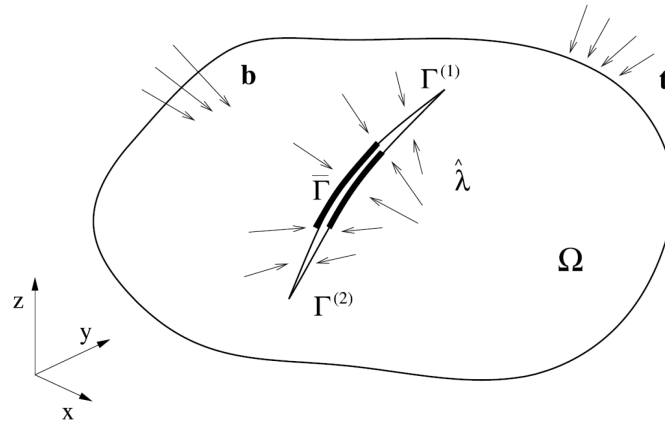
Figure 3.2. A conceptual scheme for the fault modeling (Franceschini, et al., 2016).

Consider a 3D domain $\boldsymbol{\Omega}$ that is subject to the set of body forces **b** and surface tractions $\boldsymbol{t}$, and is bordered by the frontier $\boldsymbol{\partial\Omega}$ (Figure 3.2). Two inner surfaces, $\boldsymbol{\Gamma^1}$ and $\boldsymbol{\Gamma^2}$, with strengths $\boldsymbol{\lambda}$ such that displacement continuity is guaranteed wherever condition (3.20) is confirmed, designate the fault Γ in Ω. In contrast, the fault region represented by $\bar{\Gamma} \subseteq \Gamma$ is where a relative displacement between the contact surfaces can occur and condition (3.20) is not verified.

According to standard definitions, the relative displacement u_r is the movement $\hat{u}^2$ of Γ^2 with regard to $\hat{u}^1$ that occurs on Γ^1:

$$u_r = u_2 - u_1 \qquad (3.21)$$

The virtual work concept is typically expressed as follows:

$$\delta W_i + \delta W_f - \delta W_e = 0 \qquad (3.22)$$

Where δW_i, δW_f, and δW_e are the internal, fault, and external virtual works, respectively. Let us proceed to an analysis of each term in turn.

The internal virtual work can be expressed as:

$$\delta W_i = \int_\Omega \delta \epsilon^T \hat{\sigma} dV \qquad (3.23)$$

Where ϵ is the strain vector and $\hat{\sigma}$ is the total stress vector which has shown in equation (3.3) and (3.4). In consideration of Terzaghi's principle for porous media (3.5), it is possible to substitute this into the equation (3.23), which yields the following result:

$$\delta W_i = \int_\Omega \delta \epsilon^T \sigma dV - \int_\Omega \delta \epsilon^T i\alpha p dV \qquad (3.24)$$

The virtual work associated with a fault is divided into two sections. The first section corresponds to the portion of the fault where continuity is maintained, while the second section shows the portion of the fault where sliding and openings have occurred. The relationship between the two sections is expressed as follows:

$$\delta W_f = \int_{\Gamma \backslash \overline{\Gamma}} \delta u_r^T \lambda dS + \int_{\Gamma \backslash \overline{\Gamma}} \delta u_r \lambda^T dS + \int_{\overline{\Gamma}} \delta u_r^T \tau_L dS \qquad (3.25)$$

It is important to note that in the case of an opening, the open part of the fault $\overline{\Gamma}$ does not contribute to the virtual work, as the normal and shear strengths are null ($\lambda_n = \lambda_s = 0$). Conversely, if there is sliding, only the shear strength λ_s provides a non-zero contribution.

The external virtual work considers the body force *b* and the surface traction t and can be express as:

$$\delta W_e = \int_\Omega \delta u^T b dV + \int_{\partial\Omega} \delta u_T t dS \qquad (3.26)$$

The final expression of the working principle is then:

$$\int_\Omega \delta\epsilon^T \sigma dV + \int_{\Gamma\backslash\overline{\Gamma}} \delta u_r^T \lambda dS + \int_{\Gamma\backslash\overline{\Gamma}} \delta u_r \lambda^T dS + \int_{\overline{\Gamma}} \delta u_r^T \tau_L dS =$$
$$\int_\Omega \delta\epsilon^T i\alpha p dV + \int_\Omega \delta u_T b dV + \int_{\partial\Omega} \delta u^T t dS \qquad (3.27)$$

3.4. Numerical Modelling

3.4.1. The Finite Element Method

One widespread technique for solving differential equations (covered in the previous sections) numerically, employed in engineering and mathematical modeling, is the finite element method (FEM). For solving partial differential equations in two or three spatial variables, or some boundary value problems, the FEM represents a general numerical approach. The FEM splits a complex system into smaller, more manageable components, known as finite elements, to solve a problem. This is achieved by creating a mesh of the object, which is the numerical domain for the solution and contains a finite number of points, to execute a specific space discretization in the space dimensions. A system of algebraic equations is the ultimate consequence of formulating a boundary value problem using the finite element method. Over the domain, the approach approximates the unknown function. (Logan, 2011). The local equations that model these finite elements are then assembled into a larger system of equations that models the entire problem. As a result, nodes or points are found within domain N that correspond to the vertices of the elements.

Since the interpolation functions have been identified in advance, in accordance with Franceschini (2014), it is possible to proceed from the original unknowns, which are functions, to the model unknowns, which are the nodal values. The problem can be stated as a nonlinear

system of equations in the form of $r(u)\, u = f$, where $r(u)$ is the discretized residual, u vector of unknowns (i.e., nodal displacements), and f is the vector of external forces.

The tetrahedra with linear base functions are the finite elements selected for this thesis. For a generic element e defined by the four nodes i, j, k, and m (Figure 3.3), as described by Gambolati and Ferronato (2015), the shape function ξ_i^e linked to the node i is

$$\xi_i^e = \frac{a_i + b_i x + c_i y + d_i z}{6V^e} \tag{3.28}$$

Where V^e is the element volume taken with its sign and it is

$$V^e = \frac{1}{6} \det \begin{bmatrix} 1 & x_i & y_i & z_i \\ 1 & x_j & y_j & z_j \\ 1 & x_k & y_k & z_k \\ 1 & x_m & y_m & z_m \end{bmatrix} \tag{3.29}$$

And the other coefficients are:

$$a_i = \det \begin{bmatrix} x_j & y_j & z_j \\ x_k & y_k & z_k \\ x_m & y_m & z_m \end{bmatrix} \tag{3.30}$$

$$b_i = -\det \begin{bmatrix} 1 & y_j & z_j \\ 1 & y_k & z_k \\ 1 & y_m & z_m \end{bmatrix} \tag{3.31}$$

$$c_i = \det \begin{bmatrix} 1 & x_j & z_j \\ 1 & x_k & z_k \\ 1 & x_m & z_m \end{bmatrix} \tag{3.32}$$

$$d_i = -\det \begin{bmatrix} 1 & x_j & y_j \\ 1 & x_k & y_k \\ 1 & x_m & y_m \end{bmatrix} \tag{3.33}$$
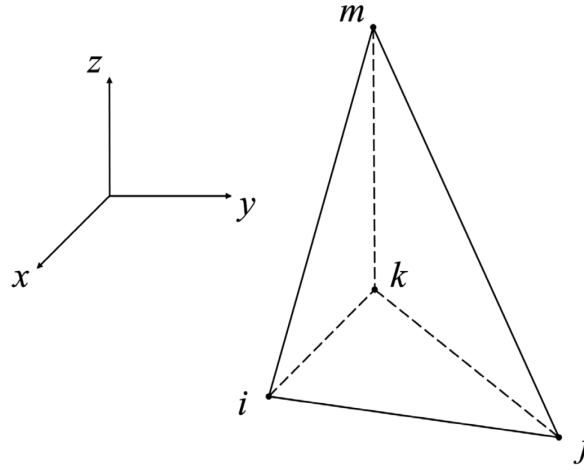
Figure 3.3. Tetrahedral finite element.

With three displacement components for each node, the displacements can be used as the main unknowns in the problem expression. If we choose a finite element, we may express in vector form the displacement of any arbitrary point within the element. If we assume that $\boldsymbol{u}$ represents the displacement vector of a point inside the element, we may write it as follows:

$$u = [\, N_1\ N_2\ N_3\ N_4\,] \begin{bmatrix} u_1 \\ u_2 \\ u_3 \\ u_4 \end{bmatrix} \qquad (3.34)$$

where N_i are the matrices that result from multiplying the identity matrix $N_i = \xi_i I_3$ the form function. The displacements, written as $u_i = \begin{bmatrix} u_{x,i}, u_{y,i}, u_{z,i} \end{bmatrix}^T$, are vectors composed of three components, u_x, u_y, and u_z, which describe the displacement in the three directions.

To express all variables as a function of the displacements, the strain vector ϵ, as defined in equation (3.12), can be written in a compact form as

$$\epsilon = Lu \qquad (3.35)$$

In agreement, each element's stresses are constant since the strains within it are constant. Therefore, the constitutive model, which may be represented in the incremental form as follows, expresses the effective stress σ as follows:

$$do = D_t d\epsilon \qquad (3.36)$$

where D_t is the tangent constitutive matrix.

Which can be explicated by

$$
\begin{Bmatrix}
d\sigma_x \\
d\sigma_y \\
d\sigma_z \\
d\sigma_{xy} \\
d\sigma_{yz} \\
d\sigma_{xz}
\end{Bmatrix}
=
\begin{bmatrix}
a_{11} & a_{12} & a_{13} & 0 & 0 & 0 \\
a_{12} & a_{11} & a_{13} & 0 & 0 & 0 \\
a_{13} & a_{13} & a_{33} & 0 & 0 & 0 \\
0 & 0 & 0 & g_1 & 0 & 0 \\
0 & 0 & 0 & 0 & g_3 & 0 \\
0 & 0 & 0 & 0 & 0 & g_3
\end{bmatrix}
\begin{Bmatrix}
d\epsilon_x \\
d\epsilon_y \\
d\epsilon_z \\
d\epsilon_{xy} \\
d\epsilon_{yz} \\
d\epsilon_{xz}
\end{Bmatrix}
\qquad (3.37)
$$

$$a_{11} = \frac{\beta - v^2}{1 - (\gamma v)^2} \qquad a_{12} = \frac{v(v + \beta\gamma)}{1 - (\gamma v)^2} \qquad a_{13} = \frac{v}{1 - \gamma v} \qquad a_{33} = 1 \qquad (3.38)$$

And

$$g_1 = \frac{\beta(1 - \gamma v) - 2v^2}{2(1 - (\gamma v)^2)} \qquad g_3 = \frac{g_1}{\theta} \qquad (3.39)$$

The parameters involved are $v = v_v$, $\beta = E_h/E_v$, $\gamma = v_h/v_v$, $\theta = G_h/G_v$, where E stands for Young modulus, v for the Poisson modulus and, G for the shear modulus defined for horizontal h and vertical v directions.

The incremental relation in terms of deformations and tension for linear elastic is given by:

$$do = C_M^{-1} D d\epsilon \qquad (3.40)$$

To resolve the issue, it is necessary to define appropriate boundary conditions. Three main types of boundary conditions can be considered:

- Neumann Conditions: These are defined on the derivative of the unknown function, typically involving the stress tensor A and the normal direction n to the boundary. In structural mechanics, Neumann conditions represent applied forces or stresses on the boundary.

34

- Dirichlet conditions: These are defined about the unknown function u. In the context of structural mechanics, Dirichlet conditions correspond to imposed displacements on the boundary of the domain.

Only Dirichlet conditions are considered in the application detailed in this thesis. Considering the structural issue:

$$u = u_0 \ \text{ on } \ \Gamma_D \qquad\qquad (3.41)$$

where Γ_D is the portion of the boundary where displacements are specified, and u_0 is the prescribed displacement vector on Γ_D.

3.4.2. Solution Of the Structural Problem with Interface Elements

According to Franceschini et al. [2016], the variational problem (3.27) is numerically solved utilizing a node-to-node formulation and the recently introduced FE approach. Equation (3.34) states that the function $u^h(x) \in U^h$, where U^h is the Hilbert function space created by the piecewise polynomials l_i and $i = 1, \dots, n_\Omega$ as n_Ω is the number of nodes in Ω, can be used to approximate the displacement of a point $u(x)$:

$$u^h(x) = \begin{bmatrix} u_x^h(x) \\ u_y^h(x) \\ u_z^h(x) \end{bmatrix} = \begin{bmatrix} \sum_{i=1}^{n_\Omega} l_i(x)u_{x,j} \\ \sum_{i=1}^{n_\Omega} l_i(x)u_{y,j} \\ \sum_{i=1}^{n_\Omega} l_i(x)u_{z,j} \end{bmatrix} = N_u(x)u \qquad\qquad (3.42)$$

Similarly, the function $\lambda^h(x) \in L^h$ can also be used to approximate the fault strength $\lambda(cx)$, where L^h is a different Hilbert function space produced by the piecewise polynomials ϕ_j, with $j = 1, \dots, n_\Gamma$, where n_Γ is the number of nodes in Γ_T and Γ_B:

$$\lambda^h(x) = \begin{bmatrix} \lambda_x^h(x) \\ \lambda_y^h(x) \\ \lambda_z^h(x) \end{bmatrix} = \begin{bmatrix} \sum_{j=1}^{n_\Gamma} \phi_j(x)\lambda_{x,j} \\ \sum_{j=1}^{n_\Gamma} \phi_j(x)\lambda_{y,j} \\ \sum_{j=1}^{n_\Gamma} \phi_j(x)\lambda_{z,j} \end{bmatrix} = N_\lambda(x)\lambda_g \qquad (3.43)$$
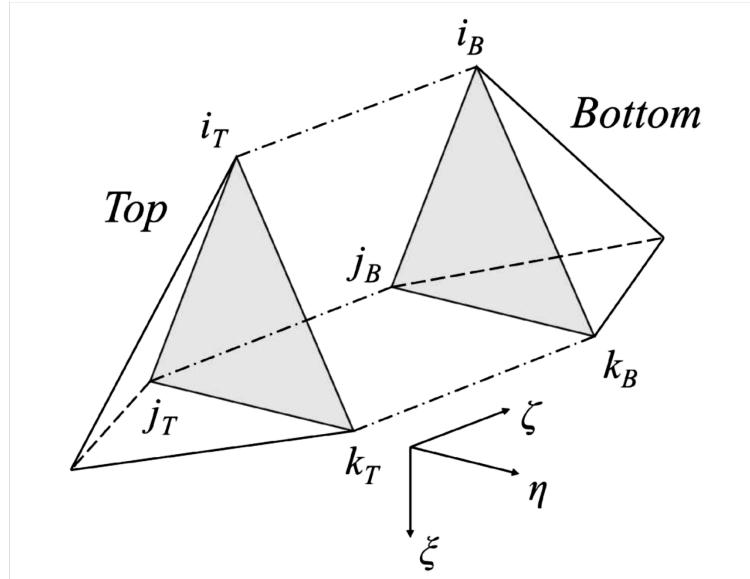
Figure 3.4. Interface element.

The Finite Element Method (FEM) necessitates the incorporation of a specific type of element, designated the Interface Element (IE), for the purpose of simulating the opening and sliding of faults within a discrete domain. These elements, initially proposed by Goodman et al. (1968), permit the violation of the congruence of displacements, which is otherwise consistently maintained by traditional finite elements.

The Interface Element is constituted by two triangular finite elements, each situated on one of the fault's contact surfaces. These elements are distinguished by their lack of thickness and may be used to imitate the discontinuities and relative motions along the fault line since their nodes are coupled and share the same coordinates (Figure 3.4).

The key features of Interface Elements include:

- No thickness: In the absence of thickness, interface elements can simulate the contact and relative motion between two surfaces without the need to introduce additional geometric dimensions, as they lack any physical thickness.

- Paired nodes: Each node in the interface is matched with an identical node on the opposite side, and the two nodes have the same spatial coordinates. This configuration enables the capture of discontinuities in the displacement field, which is essential for the precise simulation of fault mechanics.

- Displacement congruence violation: Interface elements permit discontinuities, in contrast to conventional finite elements that require displacement continuity across element boundaries. This functionality is necessary for the simulation of physical processes such as fault opening and sliding.

Mathematical analysis can be used to characterize the behaviour of interface elements by examining the relative displacements and stresses between paired nodes. This method captures the key elements of fault mechanics, including opening, closure, and sliding, and provides a scientific foundational framework for assessing the mechanical response of faults under different loading circumstances.

Finite element meshes are an effective tool for researching geomechanical problems involving faults and fractures because they can simulate fault behaviour more accurately and realistically when interface elements are integrated into the mesh.

To represent the fault strength, it is more convenient to consider a local reference system for the elements present on the surfaces Γ_T and Γ_B. The two ξ and η axes of the local system $\xi - \eta - \zeta$ are defined to complete the anticlockwise tern, while the other ζ axis is directed in the normal direction to the contact surface and typically orientated from Γ_T to Γ_B. To transition from the local strength λ to the global vector λ_g, a rotation matrix R is introduced in the following manner:

$$\lambda^h(x) = N_\lambda R \lambda = N_\lambda \lambda_g \qquad (3.44)$$

Considering equation (3.42),the relations (3.35) and (3.36) can be written as:

$$\epsilon^h = L u^h = L N_u u = B u \qquad (3.45)$$

$$dσ^h = D_t dε^h \qquad (3.46)$$

Where B is the strain matrix.

The virtual work of the defect is the cause of the new contribution to equation (3.27). In discrete space u^h, the relative displacement u_r^h along $\bar{Γ}$ is defined as follows:

$$u_r^h = u_B^h − u_T^h \qquad (3.47)$$

Where u_B^h and u_T^h are the restriction of u^h over $Γ_T$ and $Γ_B$, respectively. When the global nodal displacement vector u is mapped to the nodal displacements on the fault surfaces using the matrices S_1 and S_2, the outcome is:

$$u_r^h = N_u S_2 u − N_u S_1 u = N_u S u \qquad (3.48)$$

$$S = S_2 − S_1 \qquad (3.49)$$

Let us now examine the element-level matrices of the local unknowns. The displacement $u_r^{(e)}$ is as follows when one element e, such as the one depicted in Figure 3.3, is considered in conjunction with the relations (3.47) and (3.48).

$$u_r^{(e)} = \begin{bmatrix} u_{r,i} \\ u_{r,j} \\ u_{r,k} \end{bmatrix} = \begin{bmatrix} -I_3 & I_3 & 0 & 0 & 0 & 0 \\ 0 & 0 & -I_3 & I_3 & 0 & 0 \\ 0 & 0 & 0 & 0 & -I_3 & I_3 \end{bmatrix} \cdot \begin{bmatrix} u_{T,i} \\ u_{B,i} \\ u_{T,j} \\ u_{B,j} \\ u_{T,k} \\ u_{B,k} \end{bmatrix} = S^{(e)} u^{(e)} \qquad (3.50)$$

Where $u_{r,q}$ is the vector containing the tree component of the relative displacements along x, y and, z between the opposite nodes q_T and q_B, while I_3 is the identity matrix 3x3. The matrix $N_u^{(e)}(x)$ of the local basis functions is then equal to:

$$N_u^{(e)}(x) = \begin{bmatrix} ψ_i^{(e)} I_3 & ψ_j^{(e)} I_3 & ψ_k^{(e)} I_3 \end{bmatrix} \qquad (3.51)$$

Where the function $\psi_q^{(e)}(x)$ is the restriction on the interface elements e of the basis functions $l_{T,q}(x)$ and $l_{b,q}(x)$ as introduced in equation (3.42).

Starting with equation (3.44), the same method can be used to write $\lambda^{(e)}$ as:

$$\lambda^{(e)} = \begin{bmatrix} \lambda_i \\ \lambda_j \\ \lambda_k \end{bmatrix} \tag{3.52}$$

where λ_q is the vector containing the three components of nodal strength in the local axes ξ, η and ζ between the node's q_T and q_B. The local basis functions' matrix $N_\lambda^{(e)}(x)$, obtained using the rotation matrix $R^{(e)}$, is equal to:

$$N_\lambda^{(e)}(x) = \begin{bmatrix} \phi_i^{(e)} I_3 & \phi_j^{(e)} I_3 & \phi_k^{(e)} I_3 \end{bmatrix} \tag{3.53}$$

Where the function $\phi_q^{(e)}(x)$ is the restriction on the interface elements e of the basis function $\phi_{T,q}(x)$ and $\phi_{B,q}(x)$ as introduced equation (3.43). In particular, $\phi_q(x)$ is the piecewise constant function such that:

$$\phi_q(x) = \begin{cases} 1 \; if \; x \; \in \; A_q \\ 0 \; if \; x \; \notin \; A_q \end{cases} \tag{3.54}$$

Specifically in equation (3.54) A_q is the area associated to node q (Figure 3.5. Partitioning of the areas connected to one node.):

$$A_q = \sum_e \frac{A^{(e)}}{3} \tag{3.55}$$

Where $A^{(e)}$ is the area of the triangle e and the sum of performed considering all the triangles sharing the node q.
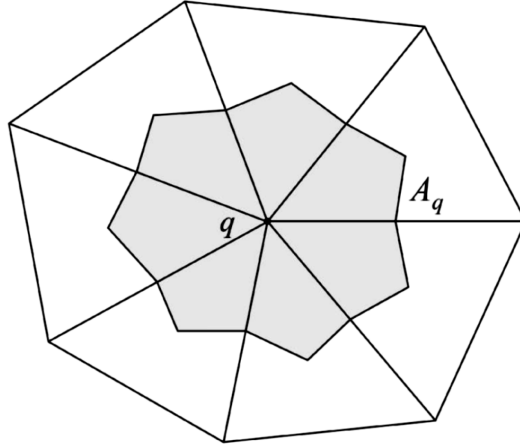
Figure 3.5. Partitioning of the areas connected to one node.

τ_L can be expressed as follows, considering the discrete function λ^h that is specified in equation (3.44) as well as the Coulomb criterion (3.20).

$$\tau_L = c - tan\varphi n^T N_\lambda R\lambda \qquad (3.56)$$

Where n is the normal vector to the fault surface $\bar{\Gamma}$, conventionally oriented from Γ_T to Γ_B. Using the maximum plastic dissipation, the expression of τ_L^h becomes:

$$\tau_L^h = (c - tan\varphi n^T N_\lambda R\lambda)\frac{N_u Su}{\sqrt{u^T S^T N_u^T N_u Su}} \qquad (3.57)$$

The final numerical model may be derived by substituting all approximations previously defined in the general equation of the virtual work principle (3.27) and express as:

$$\delta u^T \int_\Omega B^T \sigma^h dV + \delta u^T \int_{\Gamma\backslash\bar{\Gamma}} S^T N_u^T N_\lambda R\lambda dS + \delta u^T \int_{\Gamma\backslash\bar{\Gamma}} R^T N_\lambda^T N_u Su dS$$

$$+ \delta u^T \int_{\bar{\Gamma}} dS (c - tan\varphi n^T N_\lambda R\lambda)\frac{Hu}{\|u\|_H} dS \qquad (3.58)$$

$$= \delta u^T \int_\Omega B^T i\alpha p dV + \delta u^T \int_\Omega N_u^T b dV + \delta u^T \int_{\partial\Omega} N_u^T t dS$$

As the virtual displacement δu and the virtual strength $\delta\lambda$ are variable, the equation (3.58) must be true for any other configuration. Hence defining C and f as follow:

$$C = \int_{\Gamma\backslash\overline{\Gamma}} S^T N_u^T N_\lambda R\lambda dS \qquad (3.59)$$

$$f = \int_\Omega B^T i\alpha p dV + \int_\Omega N_u^T b dV + \int_{\partial\Omega} N_u^T t dS \qquad (3.60)$$

Equation (3.58) can be expressed as a non-linear system, with u and λ as the unknowns:

$$\begin{cases} \int_\Omega B^T i\alpha p dV + C\lambda + \int_{\overline{\Gamma}} (c - tan\varphi n^T N_\lambda R\lambda)\dfrac{Hu}{\|u\|_H} dS - f \\ \qquad\qquad\qquad C^T u = 0 \end{cases} \qquad (3.61)$$

The system can be defined in a more compact way as:

$$\begin{cases} F_1(u,\lambda) = 0 \\ F_2(u,\lambda) = 0 \end{cases} \qquad (3.62)$$

Equation (3.62) can be solved using the classical Newton scheme. The Jaccobian matrix $J(u,\lambda)$ is composed of four blocks.

$$J(u,\lambda) = \begin{bmatrix} \dfrac{\partial F_1}{\partial u} & \dfrac{\partial F_1}{\partial \lambda} \\ \dfrac{\partial F_2}{\partial u} & \dfrac{\partial F_2}{\partial \lambda} \end{bmatrix} = \begin{bmatrix} J_{11} & J_{12} \\ J_{21} & J_{22} \end{bmatrix} \qquad (3.63)$$

Chapter 4

4. Model Set-up

The previously described finite element–interface element (FE-IE) simulator has been employed to investigate the geomechanical behavior of the study area. Accurate geological data is critical for effectively representing earth fissures within the geological model. As reported in Section 2, the available data for Sarıgöl and its vicinity lacks precise information regarding the geological setting, with different interpretations depending on the type of information used. As fault dip is a key parameter in governing the reactivation of discontinuity surfaces, two primary models using different reference sources for interface elements are used in this thesis work. The subsequent sections detail the processes of mesh constructions, model calibrations, and the application of the GEPS3D simulator on both geologic configurations.

The model settings used in this study were derived from the available surveys carried out in the past. Previously, geophysical surveying operations were carried out in the Alaşehir Plain for various objectives. The transects typically run from north to south and encompass the entire plain. One such geoelectrical section crosses our focus area, i.e. the Sarıgöl district as highlighted in Figure 4.1, HAT-112 alignment (Figure 2.11). A second model is based on the seismic profile crossing the plain along the A-A alignment shown in Figure 4.1, see Figure 2.13.
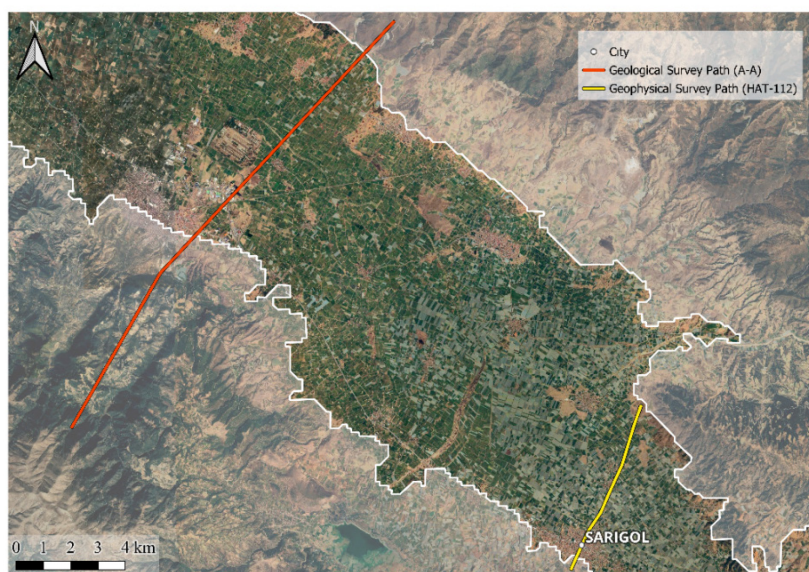
Figure 4.1. Geophysical (HAT-112) and geological (A-A) survey paths.

4.1. Mesh Set-up

The initial stage of the modeling process involves defining and discretizing the computational domain. It is essential to ensure that the domain size is sufficiently large to prevent the imposed boundary conditions from influencing the modeling outcomes within the fault zones. Additionally, a higher mesh resolution is required in the fault zones of interest to accurately replicate the geological structure and compute more accurate displacement and stress fields. As mentioned in the previous section, two different meshes were created for the geomechanical model.

The model domains are constituted by 2D vertical sections crossing the valley following the geophysical acquisitions. However, as GEPS3D needs a 3D mesh, each 2D domain was extruded along the direction orthogonal to the acquisition alignment, substantially in the west-east direction. The same model extent of approximately 9.0 km (along the horizontal direction) by 0.36 km (along the vertical direction) was selected but with different fault planes depending on the implemented information.

The first mesh (M1) was created based on the Figure 2.11. The 2D elements, which are triangles, typically measure between 15 and 20 m in size around faults and increase up to approximately 70 to 150 m near the boundary (being larger along the horizontal direction than the vertical one). The 2D mesh was constructed using Argus ONE software (Argus Holdings, 1997), totaling 7,977 elements and 4,199 nodes (Figure 4.2 and 4.3).

The second mesh (M2) was created based on the work by Ciftci et al. (2010), utilizing transverse geological cross-sections that depict the geometry of cross-sections A-A in Figure 2.13-b and the research of Koca et al. (2011) on the Sarıgöl fault. Differently from M1, Fault-4 in M2 is redefined adopting a more vertical orientation than Fault-3 in M1 (Figure and 4.5). The properties of the remaining portions of the mesh model are the same as those of mesh Model 1 (M1), including its material composition, structural integrity, geometric configuration, and boundary conditions. The 2D mesh is made of 7,977 triangular elements and 4,199 nodes.
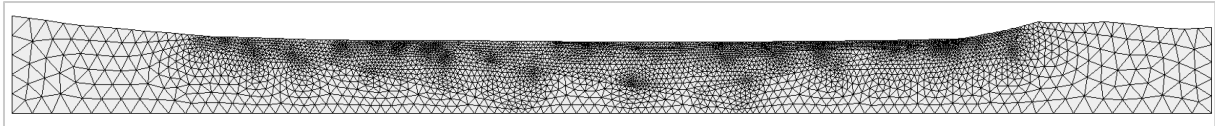
Figure 4.2. The entire 2D mesh of M1.
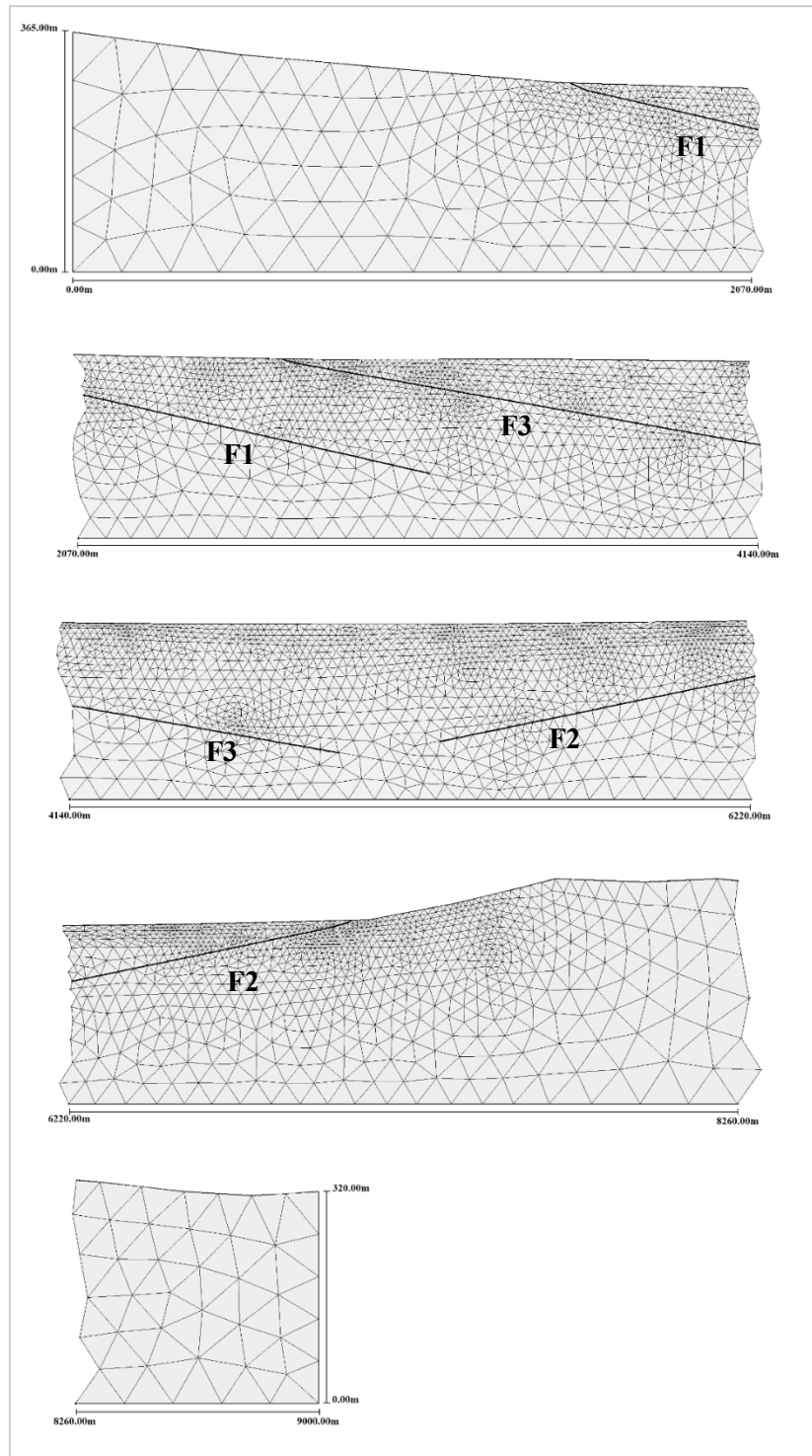
Figure 4.3. The 2D mesh is used to build the 3D mesh for M1. The faults are located on the bold lines where the mesh is more refined. F(n) represents the fault's names.
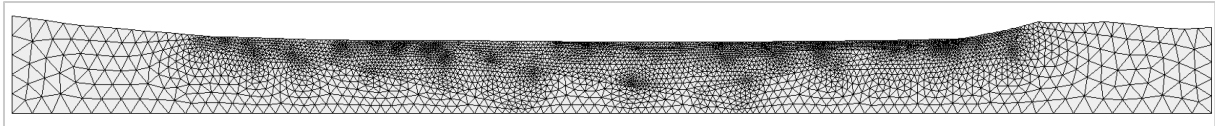
Figure 4.4. The entire 2D mesh of M2.
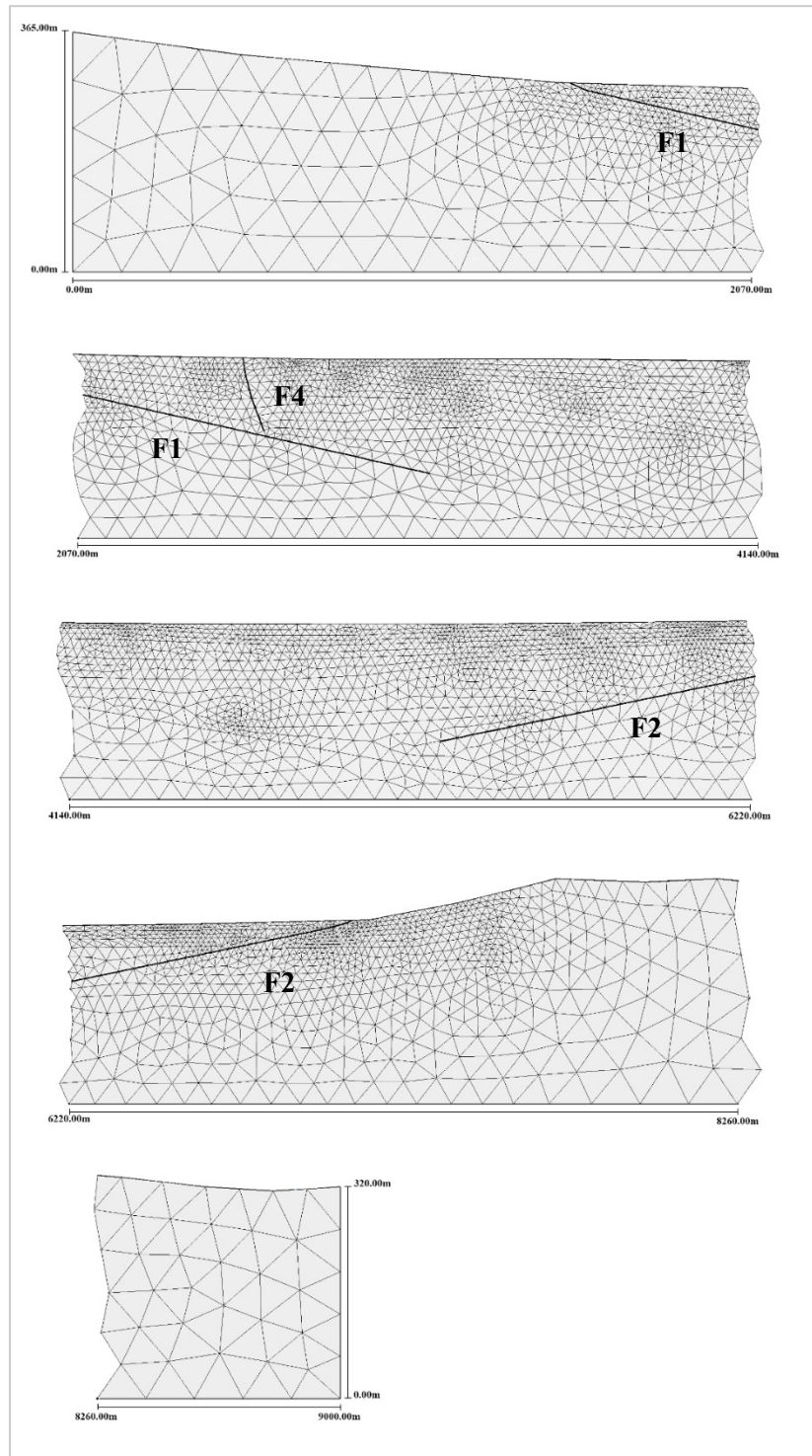
Figure 4.5. The 2D mesh is used to build the 3D mesh for model M2. The faults are located on the bold lines where the mesh is more refined. F(n) represents the fault's names.

The 3D meshes were constructed using the GEN3D generator for 2 meshes. The software essentially projects the 2D mesh nodes in the direction orthogonal to the vertical plane section, considering the stratigraphy. The aquifer system was delineated based on the geological model by Alper et al. (2022) and borehole drill log (Figure 2.12) data from the survey cross-section and the alluvial deposits was subdivided into six layers. The 3D mesh, as obtained by an 800 m projection of M1 and M2 in the horizontal direction, is shown in Figure 4.7 and 4.8.
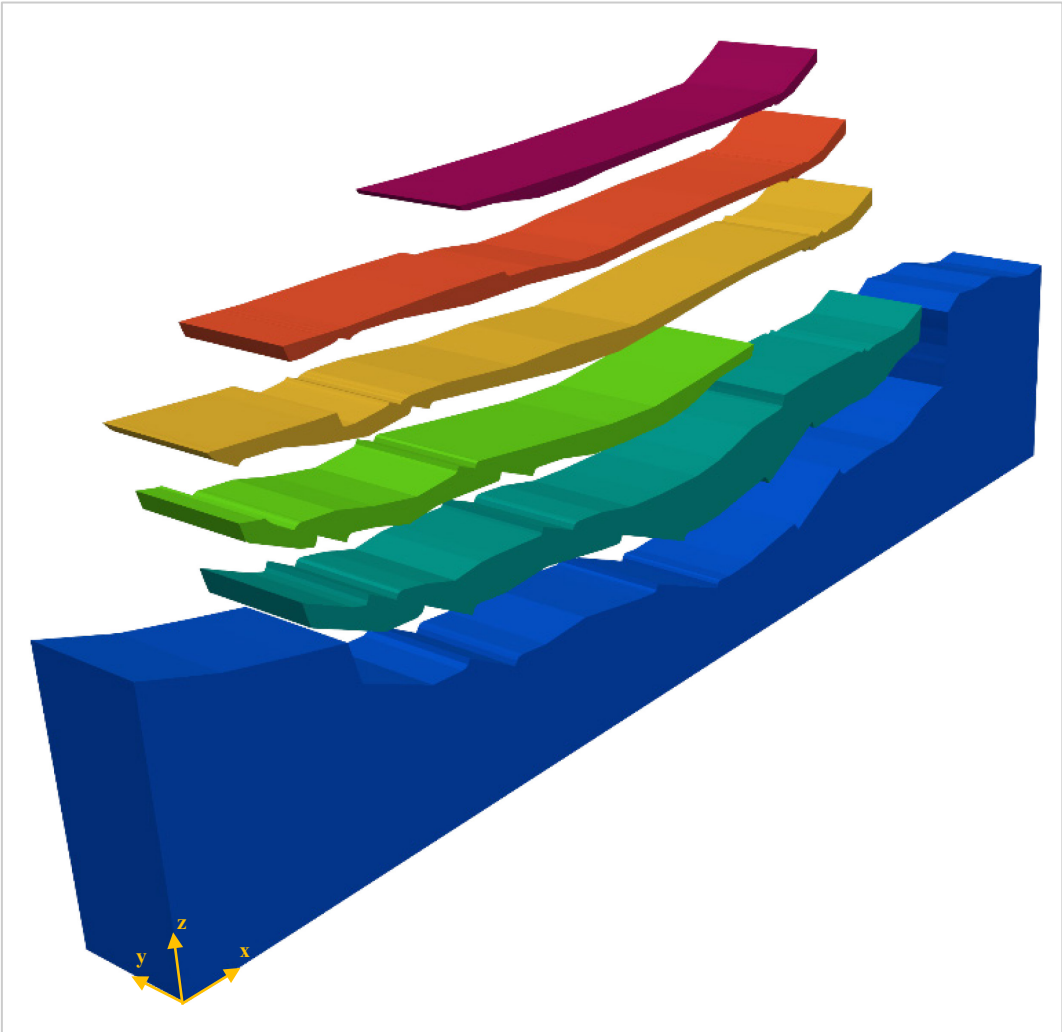
Figure 4.6. An expanded model of a 3D model for only material system of M1 and M2
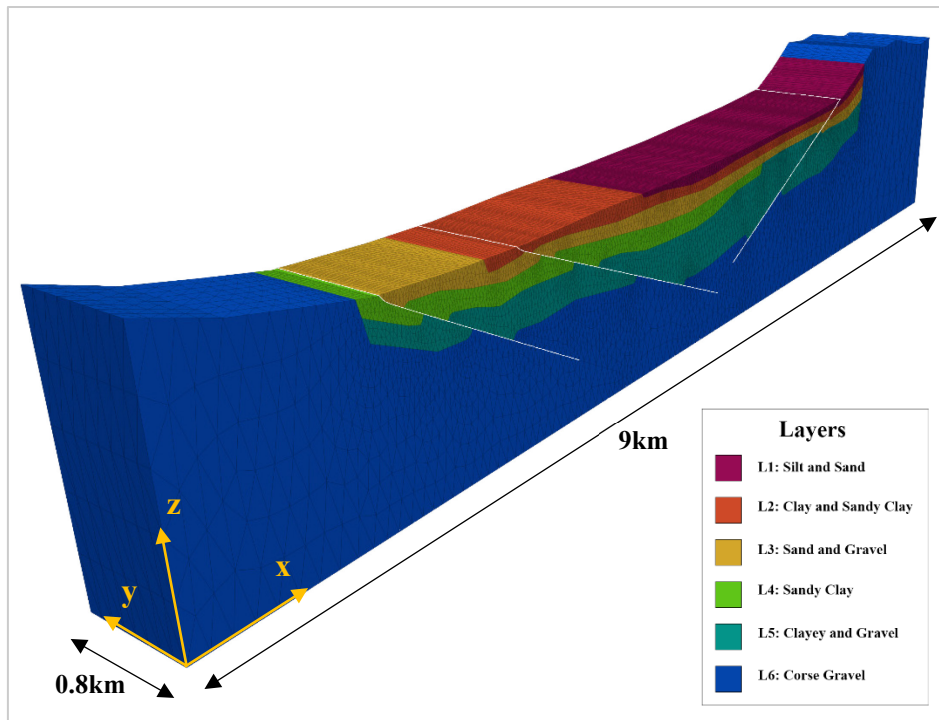
Figure 4.7. Axonometric view of the 3D FE continuous model for M1. White lines represent faults. The vertical scale (z-axis) is exaggerated by a factor of 5 with respect to the horizontal one.
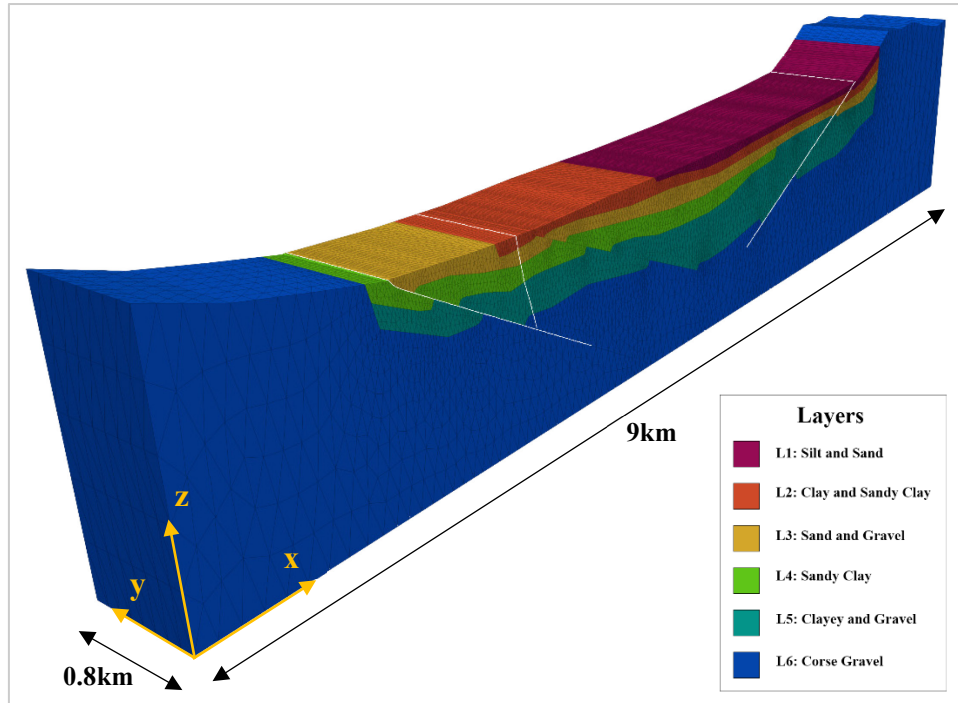
Figure 4.8. Axonometric view of the 3D FE continuous model for M2. White lines represent faults. The vertical scale (z-axis) is exaggerated by a factor of 5 with respect to the horizontal one.

Six lithological units, comprising alternating coarse-fine deposits, were identified through the combination of geophysical surveying and drill log analysis. The topmost layer (L1) is thought to be permeable due to the presence of silty sand elements, representing an unconfined aquifer. The confining layer is made up of clays and sandy clay composes layer L2. The most productive aquifer layer is L3, made primarily of sand and gravel. This is followed by L4, a confined layer made primarily of sandy clay. The lowest unit (L5) is a clayey gravel layer that sits over the bedrock from the Neogene (Figure 2.12). The two primary aquifer units in the study area are L3 and L5, with L3 containing the majority of groundwater production wells (Elçi, et al., 2022).

The faults intercepting the aquifer system require the addition of interface elements along their surfaces. This results in a total number of nodes that increases since the nodes are replicated for each IE at all points. The final 3D meshes for the continuous model include 37,791 nodes and 191,448 tetrahedral elements. For the discontinuous model, M1 has 39,681 nodes (1,890 interface elements seen in Figure 4.9-a) and 191,448 tetrahedral elements, M2 has 39,006 nodes (1,215 interface elements seen in Figure 4.9-b) and 191,448 tetrahedral elements.
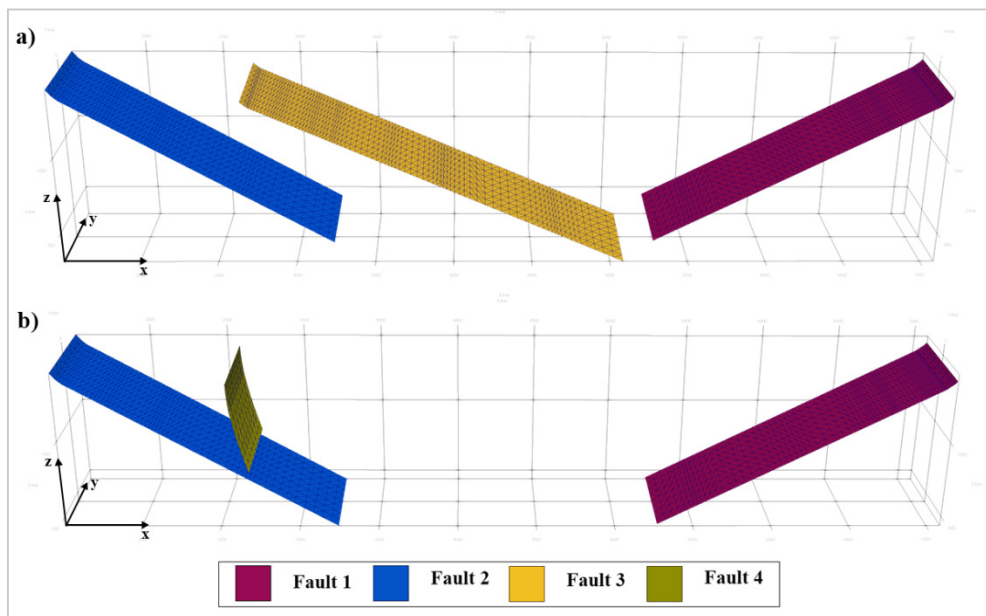
Figure 4.9. Axonometric view of interface elements for M1 (a) and M2 (b).

Figure 4.10 illustrates the approximate location of the Sarıgöl district center with respect to models 1 and 2.

Figure 4.10. Approximate location of Sarıgöl on model 1 and model 2. Figure has merged faults (F1, F2, F3 and, F4) for all models.

Chapter 5

5. Model Results

5.1. Geomechanical Model Calibration

The geomechanical model is used to predict stresses and displacement fields caused by excessive groundwater pumping. Proper boundary conditions must be specified to apply to the model. In this study, the domain's lateral and bottom surfaces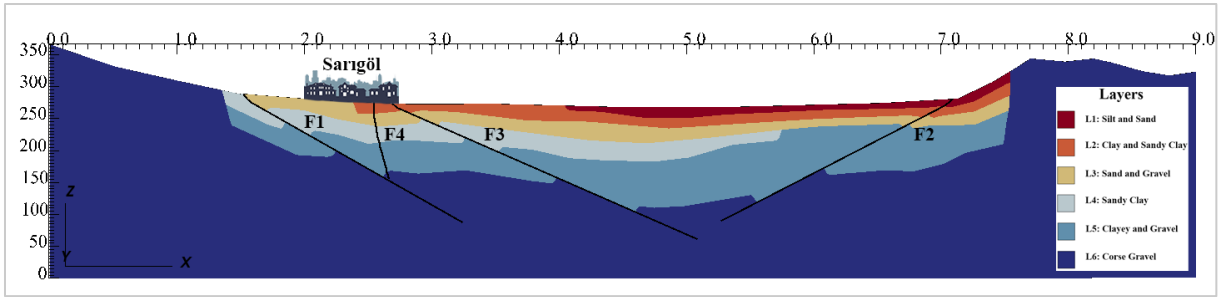 are characterized by Dirichlet boundary conditions, with zero displacements on the bottom and the North and South lateral surfaces corresponding to the bedrock. Along the two lateral surfaces parallel to the geologic section, only the horizontal component orthogonal to the section itself has been precluded. The top of the model, representing the land surface, is a traction-free boundary. Variations in pressure are being used as external forces. The model is first applied to the continuous situation, i.e., without the interface elements; the faults and their potential activation are addressed in the discontinuous simulations during a second phase.

The calibration has been performed using the land displacement dataset made available by the RESERVOIR project using the P-SBAS algorithm. P-SBAS is an advanced Interferometric Aperture Radar technique for monitoring ground deformation, which was used on a stack of Sentinel-1 SAR images in both descending and ascending orbits acquired from June 2016 to July 2020 (Navarro-Hernández, et al., 2023).

Several constitutive laws for the soil mechanical behavior can be used in GEPS3D; the linear elastic and hypo-plastic laws are the most widely used constitutive relationships. The primary distinction is that in the former law, the compressibility c_M is constant during the simulation, whereas in the latter, it also depends on the actual stress state. Due to the lack of specific information, it has been decided to use a linear elastic law in this modeling study.

The model was run using average geomechanical values from previous modeling studies in the area (Li, 2024; Elçi, et al., 2022); To calibrate the model, a uniform pressure change was applied to units L2 to L5. The pressure change was determined based on the groundwater head change from the observation well closest to the study area (Figure 5.1). Figure 5.2 shows the observed

groundwater head and the simulated values by the RESERVOIR groundwater model (Elçi, et al., 2022). Consequently, a 10 m head drop was imposed on the model over a period of 8 years.
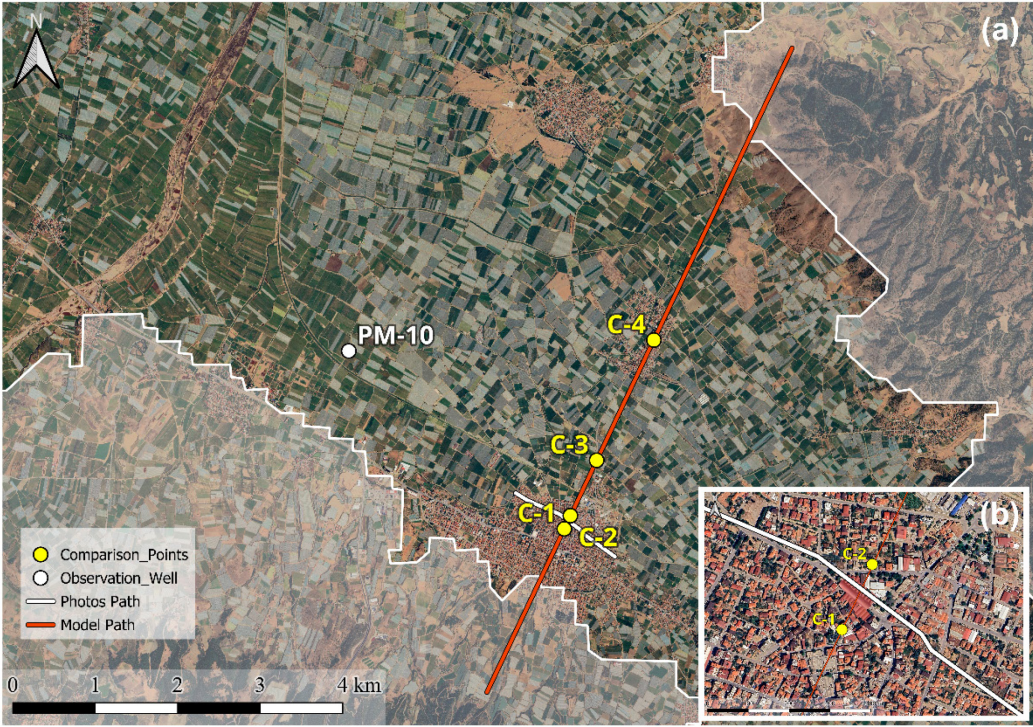

Figure 5.1. a) Location of the observation well PM-10 and comparison points for calibration. b) Closer view of comparison points C-1 and C-2 separated by a fault.
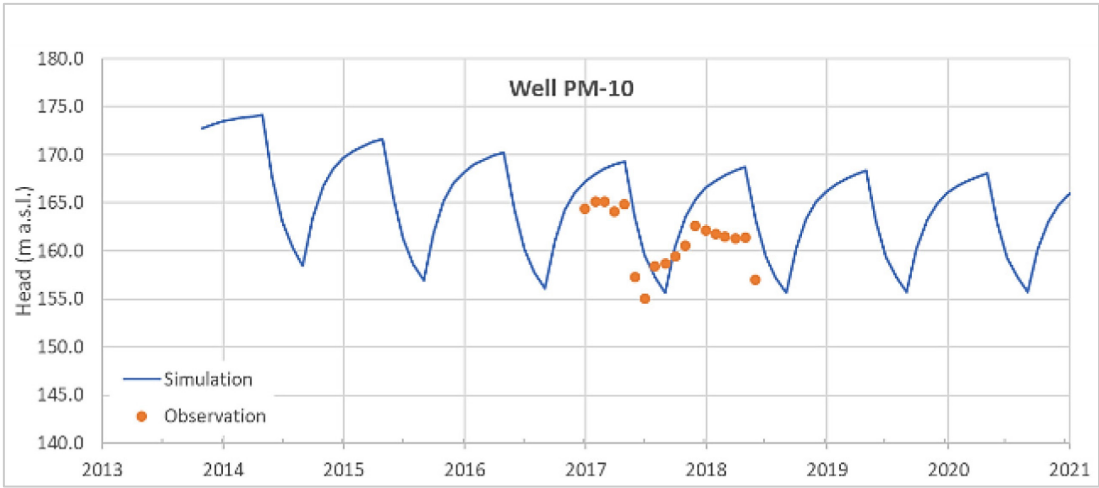
Figure 5.2. Hydrographs of the observed and simulated hydraulic head for a selected observation well PM-10 in the GRB alluvial aquifer as provided by the RESERVOIR project (Elçi, et al., 2022)

The geomechanical parameter values used for the various aquifer units are given in Table 5-1. The results were compared with the available land displacements in correspondence with the four exemplificative locations shown in Figure 5.1. Figure 5.3 shows the measured vertical displacements for those four locations as provided by Sentinel-1 data.
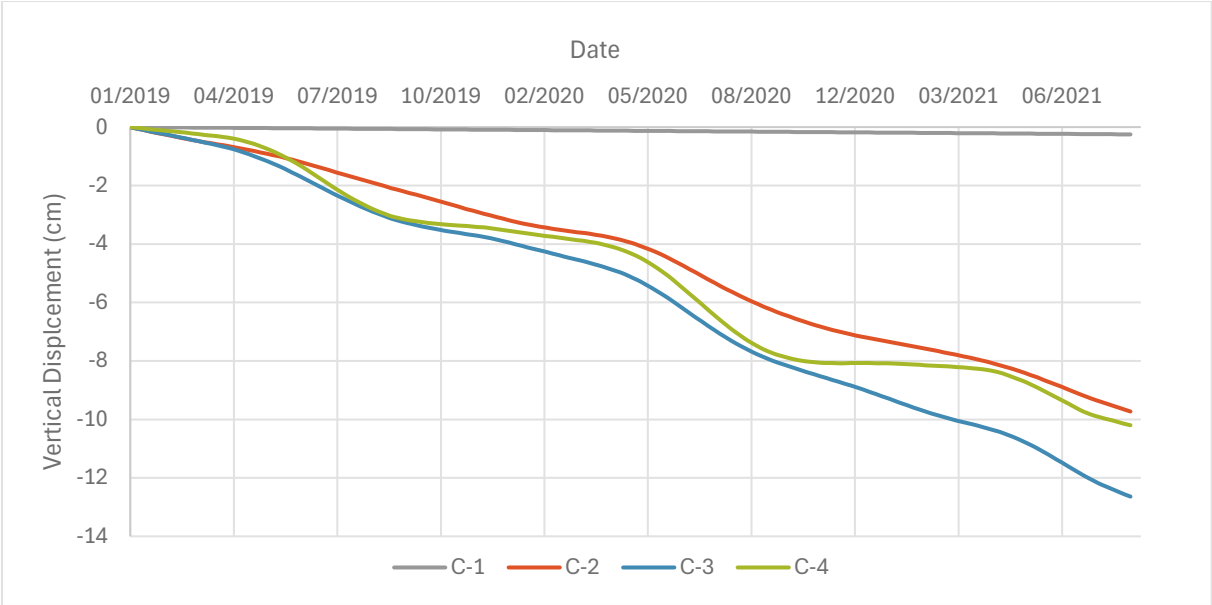
Figure 5.3. Measured data at four locations in the study area for 2019 (Navarro-Hernández, et al., 2023). Maximum vertical displacements are -10.20 cm for C-1, -12.64 cm for C-2, -14.45 cm for C-3, and -0.25 cm for C-4.

Following several trials, keeping fixed the aquifer (layer 3 and layer 5) compressibility based on previous works (Li, 2024; Elçi, et al., 2022) and adjusting the value for the aquitards, a final test was designed to change the compressibility of material in the aquitard and the aquifer layers. Additionally, layer 6 (coarse gravel) has been selected for its low compressibility. This was achieved by varying the value of c_M in the geological layers Figure 2.11).

It is well known that aquitards are typically more compressible than aquifers. Therefore, the initial values for the compressibility of aquitards (c_M) were set to be five times greater than the compressibility of aquifers. Initially, these values were increased by 25% over three simulations (S2 to S4); however, the results deviated significantly from the InSAR measurements at the selected comparison points. Subsequently, the c_M values were decreased by 25% over five simulations (S5 to S9) (see the Table 5-1). The comparison between the measurements and the model results, relative to four locations (Figure 5.1) selected along the surface trace, are shown in Figures 5.4, 5.5, 5.6, and 5.7. The results of Scenario 9 (S9) demonstrated the better match

with the measurements for the period between 2019 and 2021 at points C-2, C-3, and C-4 compared to other scenarios. Notice that land subsidence at C-1 is largely overestimated irrespective of the scenario.

Table 5-1. Compressibility for each layer of different scenarios for calibration model.

Layer Number	Materials	c_M (kPa^{-1})								
		S1 (Initial)	S2	S3	S4	S5	S6	S7	S8	S9
1	Silt and clay	5.00E-05	6.25E-05	7.81E-05	9.77E-05	3.75E-05	2.81E-05	2.11E-05	1.58E-05	1.19E-05
2	Clay and sandy clay	5.00E-05	6.25E-05	7.81E-05	9.77E-05	3.75E-05	2.81E-05	2.11E-05	1.58E-05	1.19E-05
3	Sand and gravel	1.00E-05	1.00E-05	1.00E-05	1.00E-05	1.00E-05	1.00E-05	1.00E-05	1.00E-05	1.00E-05
4	Sandy clay	5.00E-05	6.25E-05	7.81E-05	9.77E-05	3.75E-05	2.81E-05	2.11E-05	1.58E-05	1.19E-05
5	Clayey and gravel	1.00E-05	1.00E-05	1.00E-05	1.00E-05	1.00E-05	1.00E-05	1.00E-05	1.00E-05	1.00E-05
6	Coarse gravel	1.00E-08	1.00E-08	1.00E-08	1.00E-08	1.00E-08	1.00E-08	1.00E-08	1.00E-08	1.00E-08

Figure 5.4. Comparison between InSAR measurements and the simulated vertical displacement at point C-1 (see Figure 5.1 for the location) for Scenario 1, 2, 5, 7 and 9. The measured data ranges from 2019 to 2021.

Figure 5.5. Comparison between InSAR measurements and the simulated vertical displacement at point C-2, (see Figure 5.1 for the location) for Scenario 1, 2, 5, 7 and 9. The measured data ranges from 2019 to 2021.

Figure 5.6. Comparison between InSAR measurements and the simulated vertical displacement at point C-3, (see Figure 5.1 for the location) for Scenario 1, 2, 5, 7 and 9. The measured data ranges from 2019 to 2021.
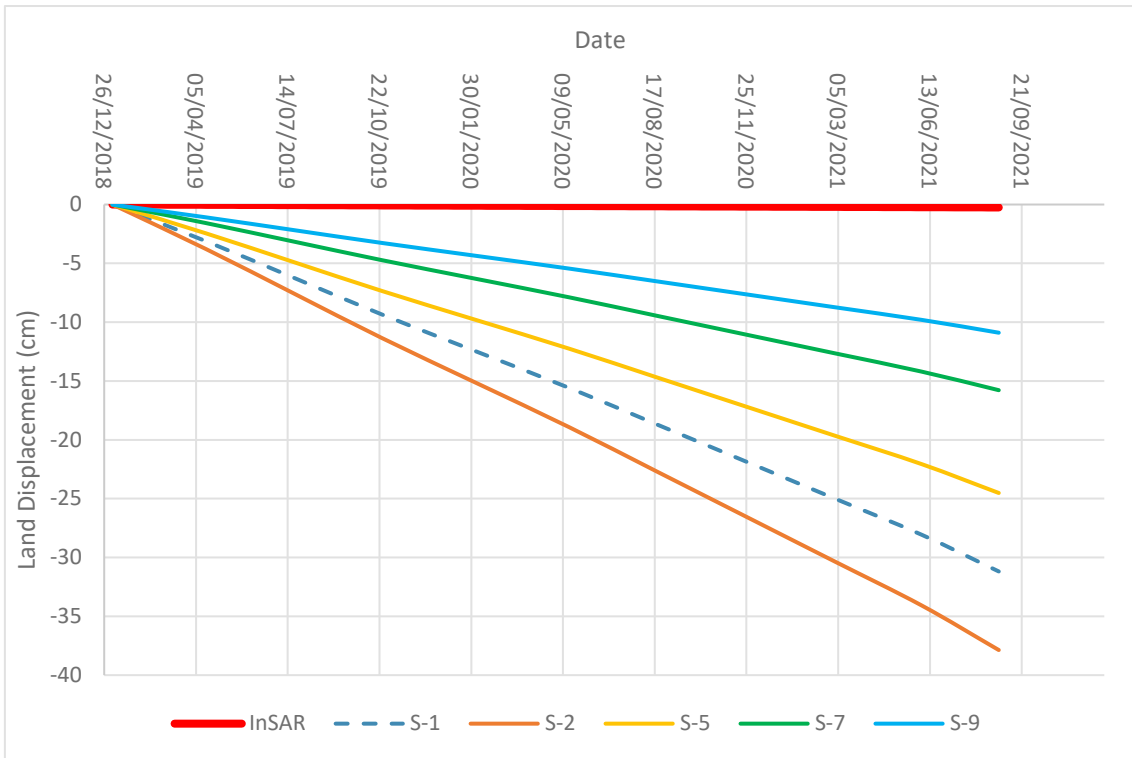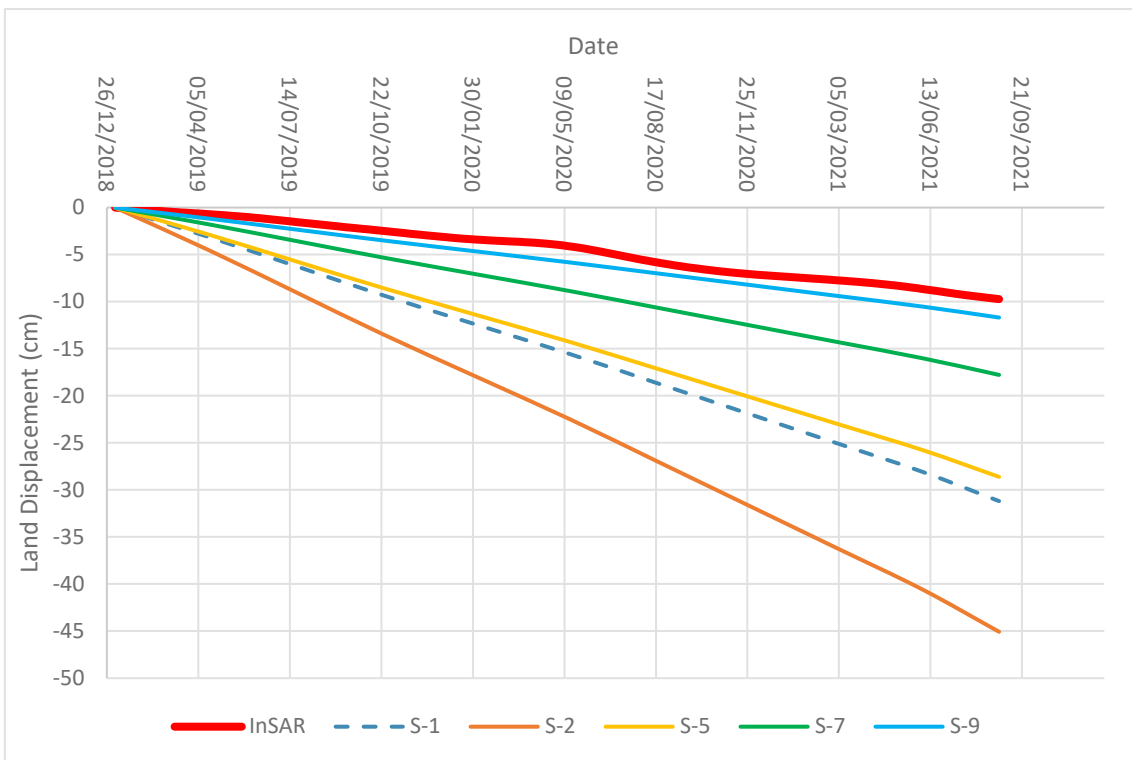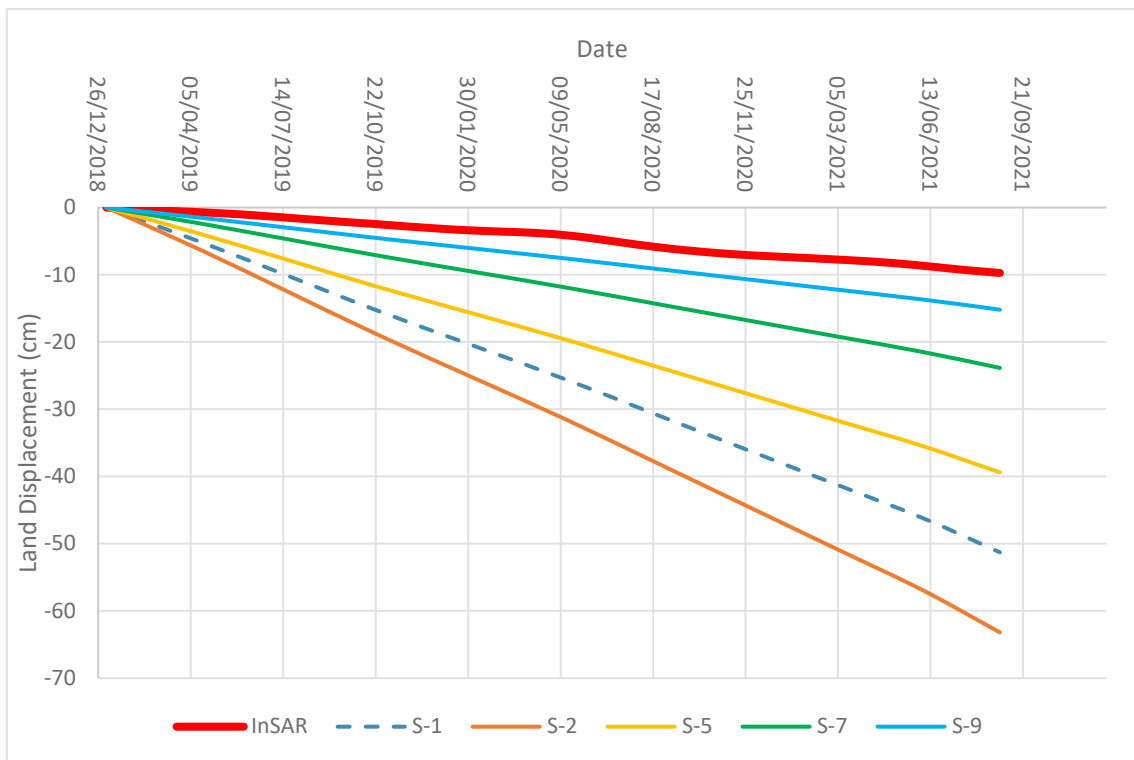

Figure 5.7. Comparison between InSAR measurements and the simulated vertical displacement at point C-4, (see Figure 5.1 for the location) for Scenario 1, 2, 5, 7 and 9. The measured data ranges from 2019 to 2021.
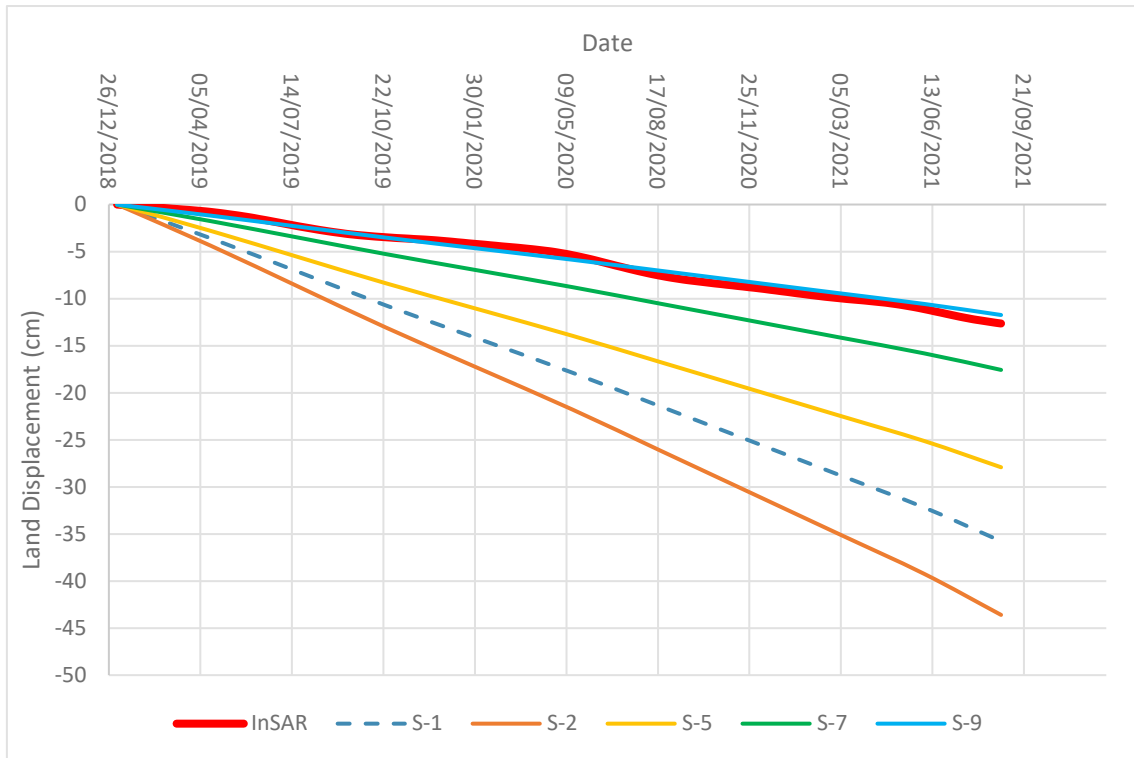
Scenario 9 yielded results that were better capturing the InSAR measurements compared to the other scenarios. Consequently, the material compressibility values from Scenario 9 were selected for the remainder of the simulations in this work. This indicates that the aquitards (L1, L2, and L4) are 19% more compressible than the aquifer. The main parameters are presented in Table 5-2.

Table 5-2. Calibrated layer parameters for 3D geomechanical model.

Layer Number	Materials	Properties	
		c_M	ν
1	Silt and clay	1.19E-05	0.3
2	Clay and sandy clay	1.19E-05	0.3
3	Sand and gravel	1.00E-05	0.3
4	Sandy clay	1.19E-05	0.3
5	Clayey and gravel	1.00E-05	0.3
6	Coarse gravel	1.00E-08	0.3

5.2. The Geomechanical Response to the Pressure Changes from the RESERVOIR Groundwater Model

The groundwater flow data from the RESERVOIR project were utilized to estimate the effect of hydraulic pressure change on the geomechanical model. The RESERVOIR project, developed by Dokuz Eylül University in Turkey, provided a simulation of the groundwater flow model for the pilot area (shown in Figure 2.2). The project examined fluctuations in groundwater levels over an eight-year simulation period, aiming to identify regions within the domain with significant groundwater level declines due to exploitation.

Figure 5.8 shows the simulated drawdown in Layer 2 and Layer 3 from September 2013 to June 2021. These results highlight areas within the research domain where groundwater storage in the aquifer has decreased.
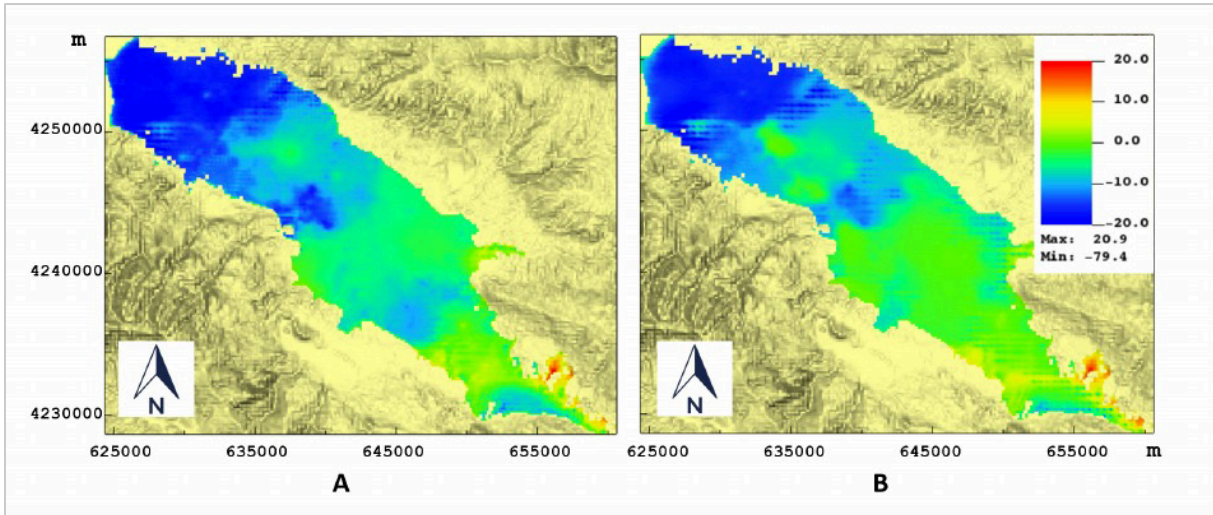
Figure 5.8. Hydraulic head change ΔH (m) as obtained by the calibrated groundwater model A) within aquifer L2 and B) within aquitard L3 over the time interval spanned by the InSAR analysis (Li, 2024).

The 3D models developed during the thesis (Figure 4.2 and Figure 4.4) were matched against the RESERVOIR project modeling outputs, and basic interpolation was applied to determine changes in the groundwater hydraulic head for each element of meshes M1 and M2. Using this data, hydraulic pressure changes were obtained for each element over the 8-year period.

The data acquired from the RESERVOIR model were used to derive the pressure changes (Δp) along the vertical section of the geomechanical model (Figure 5.9 and 5.10).
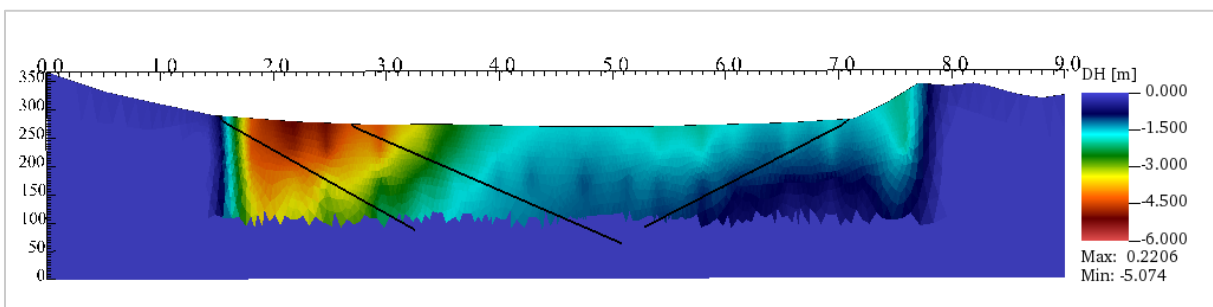
Figure 5.9. Hydraulic head changes for M1 as obtained from groundwater flow model of the RESERVOIR project along the selected Sarıgöl section in the GRB alluvial aquifer. The pressure change refers to the end of the simulation. The vertical scale is exaggerated by a factor of 5 with respect to the horizontal one.

57
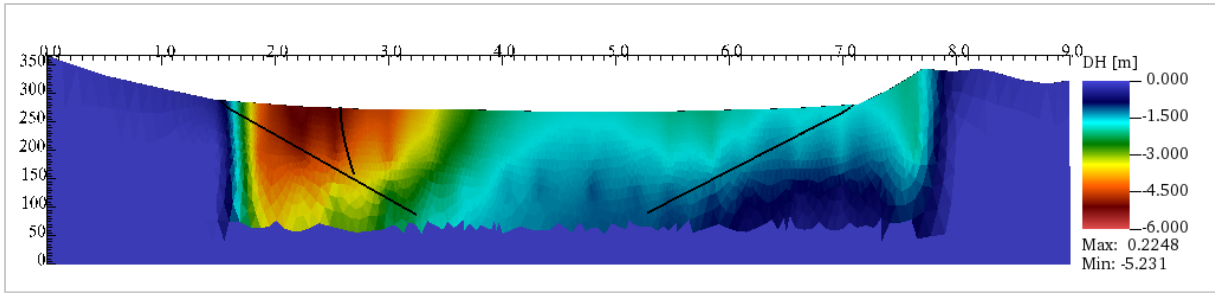
Figure 5.10. Hydraulic head changes for M2 as obtained from groundwater flow model of the RESERVOIR along of the selected Sarıgöl section in the GRB alluvial aquifer. The pressure change refers to the end of the simulation. The vertical scale is exaggerated by a factor 5 with respect to the horizontal one.

Inspection of the simulated groundwater head from the RESERVOIR project reveals that there is a lack of correlation between the INSAR land displacements and the pressure changes in the Sarıgöl district. It is also known that in the middle of the basin, land use is dominated by vineyards. This means that groundwater use would be relatively higher here than at the edge of the alluvial basin. But only looking at the simulation results, the hydraulic head drop around the city is about 5 m and in the middle of the alluvial basin, it is close to 1 m.

Based on these simple notes, the expectation of matching the InSAR measurements with the outcome of the geomecanical model is quite low. Indeed, the GEPS3D results are described in the following.
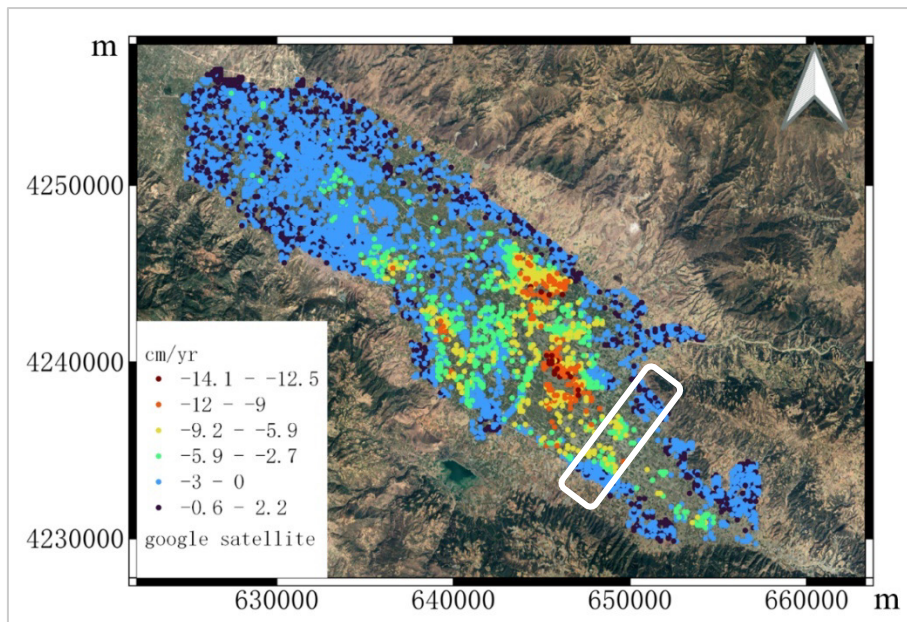
Figure 5.11. InSAR vertical land displacement rates for GRB (Li, 2024). White polygon represents the study area.

58

The results of the simulation in terms of land displacements and stress fields (with compressive stress characterized by negative values) are analyzed with the main focus on the possible activation of faults.

Recalling Section 3, the activation of a fault is related to the limited shear stress τ_L defined in Eq. (3.20). Therefore, the safety factor can be calculated as

$$\chi = \frac{|\tau_s|}{\tau_L} = \frac{|\tau_s|}{c - \sigma_n tan\varphi} \qquad (5.1)$$

where τ_s is the actual shear strength.

5.2.1. Model 1

Figure 5.12 shows the vertical (a) and horizontal (b) displacements obtained from the geomechanical simulation from September 2013 to June 2021 for Model 1. The largest land displacement occurs between faults 1 and 3 at the ground surface. In terms of vertical displacements, the largest movements are near the settlement area and do not exceed 5 cm at the end of the simulation (Figure 5.12-a). The horizontal movements are in the order of a few millimeters in the x-direction (northeast). Horizontal ground movement near the land surface is observed to move away from the faults towards the center of the alluvial basin, where horizontal displacements are zero (Figure 5.12-b).

This model ran with an 8-year groundwater flow simulation as mentioned above. As a result, less than 1 cm/year of vertical land subsidence was observed in Figure 5.12-a and the main subsidence bowl is located between fault1 and fault 3 in correspondence of Sarıgöl. However, this finding is not supported by the InSAR displacement rates, which indicate the largest displacements rates, mostly ranging between 2.7 and 5.9 cm per year, in the central part of the valley (Figure 5.11).

Figure 5.12. Vertical (a) and horizontal (b) displacements obtained from the geomechanical simulation, Model 1, using the hydraulic head changes as provided by RESERVOIR from September 2013 to June 2021.

The observed earth fissures (Figure 2.4) are located along fault 3 for M1. Consequently, our attention is focused on fault 3. The initial normal stress and shear stress for the faults are illustrated in Figure 5.13. Upon closer examination of fault 3, it can be observed that the maximum normal stress is -20.97 kPa near the surface and the minimum is -4074 kPa at a depth of 210 m. Conversely, the minimum shear stress is 8.29 kPa at the surface, while the maximum is 532.10 kPa at a depth of 210 m.

Figure 5.13. Initial normal stress (a) and shear stress (b) on the fault surfaces for Model 1. Notice that compressive stresses are negative.

Based on both shear and normal stress, the safety factor was calculated for the model, with a maximum value of 0.2 (Figure 5.14). It can be concluded that, for this model, the use of the

simulated hydraulic data from the RESERVOIR project does not indicate fault reactivation. The value of χ remains far from the critical bound equal to 1, which implies fault activation and earth fissure development.
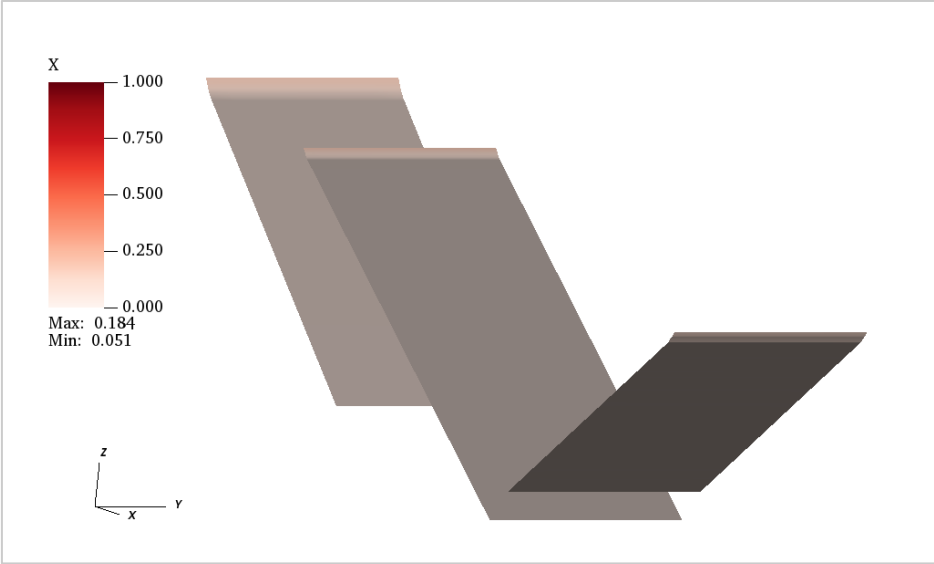
Figure 5.14. Value assumed by the safety factor on the faults considering the hydraulic head-dropping simulation from September 2013 to June 2021 for Model 1.

5.2.2. Model 2

Figure 5.15 illustrates the displacements in both vertical and horizontal directions as computed by GEPS3D using the hydraulic head changes provided by the RESERVOIR Project over the period from September 2013 to June 2021. The largest land displacement occurs between faults 1 and 4 close to the ground surface. In terms of vertical displacements, the largest movements near the settlement area do not exceed 6 cm at the end of the simulation. The horizontal movements are in the order of a few millimeters in the x-direction (northeast).

Similar to Model 1, also Model 2 provides a subsidence quantification that do not match the available measurements. Again, the loss of land elevation is faster in correspondence of Sarıgöl, between fault 1 and fault 4 (Figure 5.15-a). However, InSAR displacement rates mostly ranged between 2.7 and 5.9 cm per year, with central areas showing 5.9 to 9.2 cm per year (Figure 5.11).
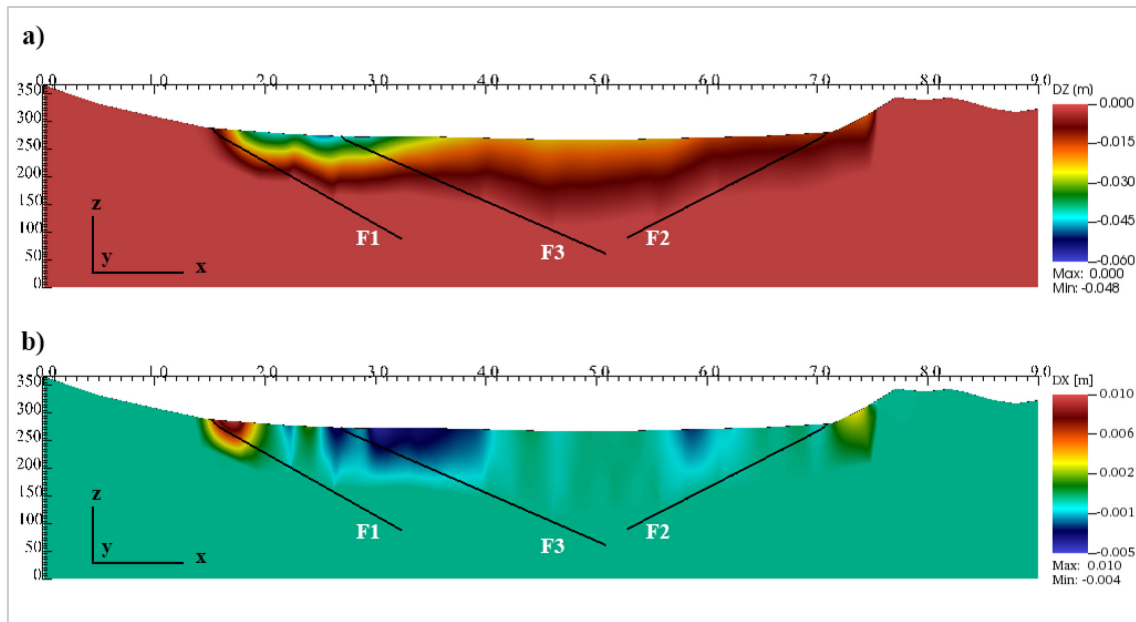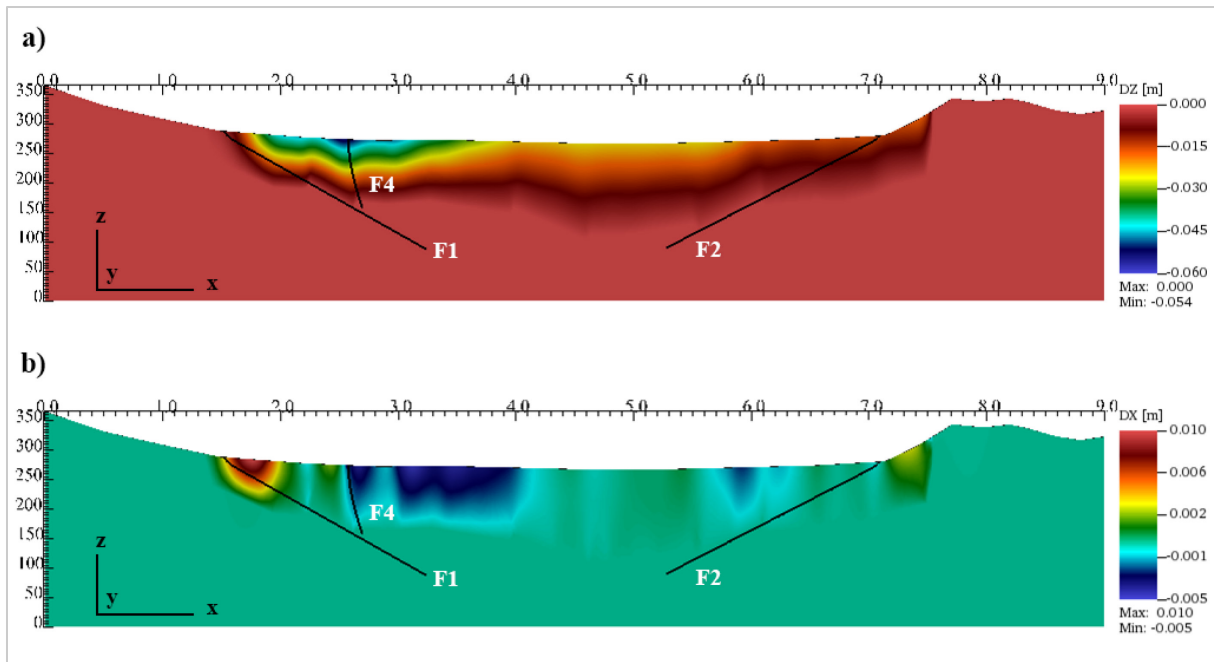
Figure 5.15. Vertical (a) and horizontal (b) displacements obtained from the geomechanical simulation, Model 2, using the hydraulic head changes as provided by RESERVOIR from September 2013 to June 2021.

The observed earth fissures (Figure 2.4) are located near fault 4 for M2. Consequently, our attention is focused on fault 4. The initial normal and stress for all faults is illustrated in Figure 5.16. Upon closer examination of fault 4, it can be observed that the maximum normal stress is -7.87 kPa at the surface and the minimum is -1379.35 kPa at a depth of 116 m. Conversely, the minimum stress is 1.27 kPa near the surface, while the maximum is 753.82 kPa at a depth of 116 m.
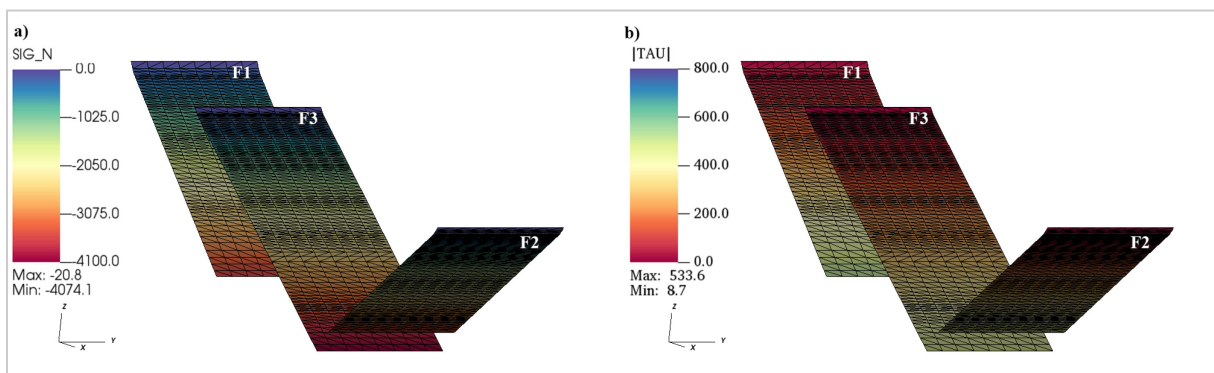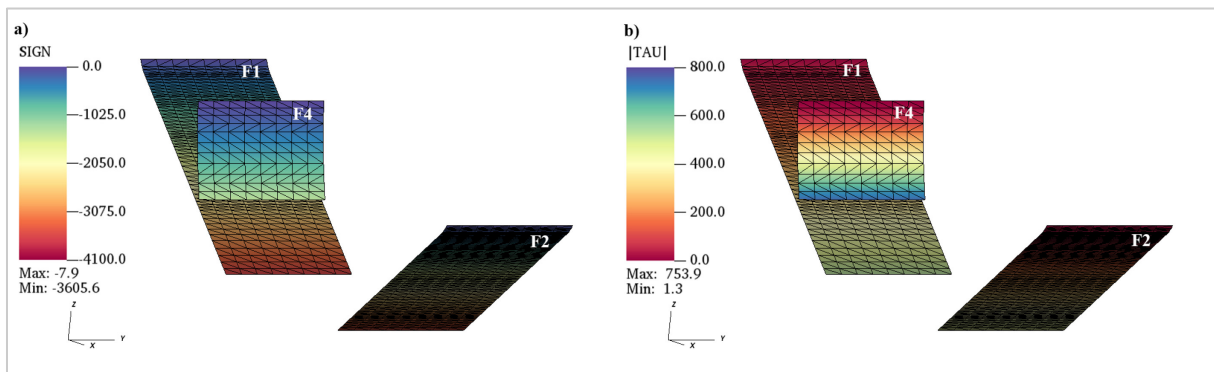

Figure 5.16. Initial normal (a) and share stress (b) on the fault's surfaces for Model 2.

Based on both shear and normal stress, the safety factor for the model was calculated, reaching a maximum value of 0.3 (Figure 5.17). This indicates that the simulated hydraulic data from the

RESERVOIR project does not suggest fault reactivation. The value of χ remains significantly below the critical threshold of 1, which is required for fault activation and the development of earth fissures. Additionally, this underscores the importance of fault geometry in the safety factor. Compared to Model 1, which has a more horizontal fault (Figure 5.14), our safety factor χ is closer to 1 on the interested fault in this model, indicating a higher proximity to the critical threshold and thus a greater potential for fault reactivation.
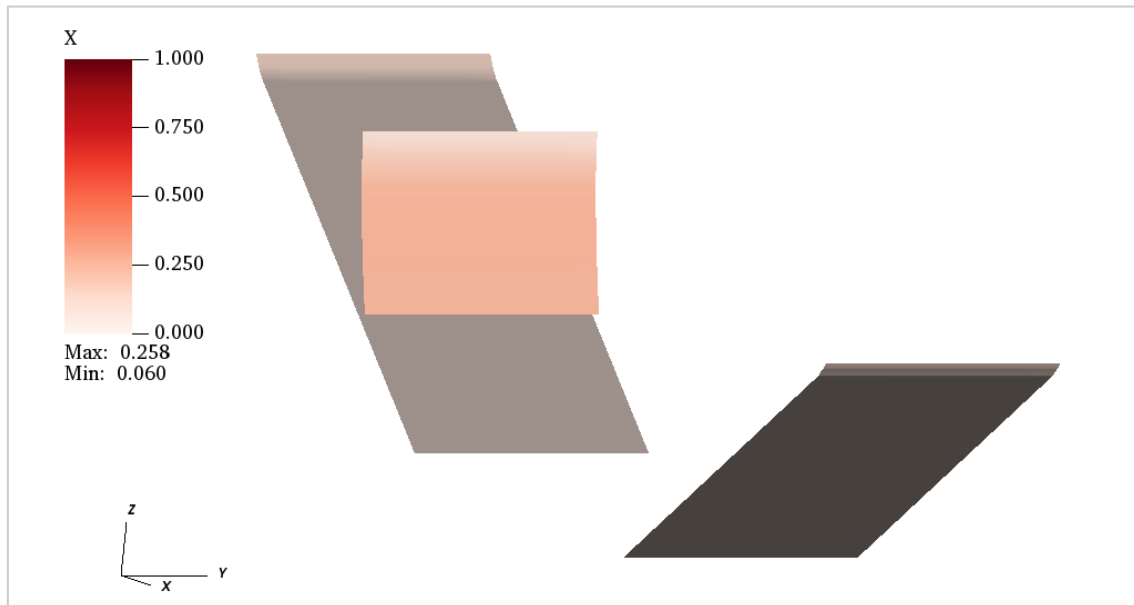
Figure 5.17. Value assumed by the factor of safety on the faults considering the hydraulic head-dropping simulation from September 2013 to June 2021 for Model 2.

5.3. Results from the EF-IE Models with Reasonable Pressure Change

To gain i) a deeper understanding of the relationship between groundwater pressure changes with continuous (land subsidence) and discontinuous (earth fissures associated with fault reactivation) displacements, and ii) to test the possibility that the observed earth fissures in Sarıgöl can be caused by aquifer overexploitation, a last set of simulations was carried out by applying a reasonable hydraulic head change to layers from L2 to L5, but restricted to:

- the portion of the aquifer between faults 2 and 3 for M1 (Figure 5.18).
- the portion of the aquifer between faults 2 and 4 for M2 (Figure 5.19).
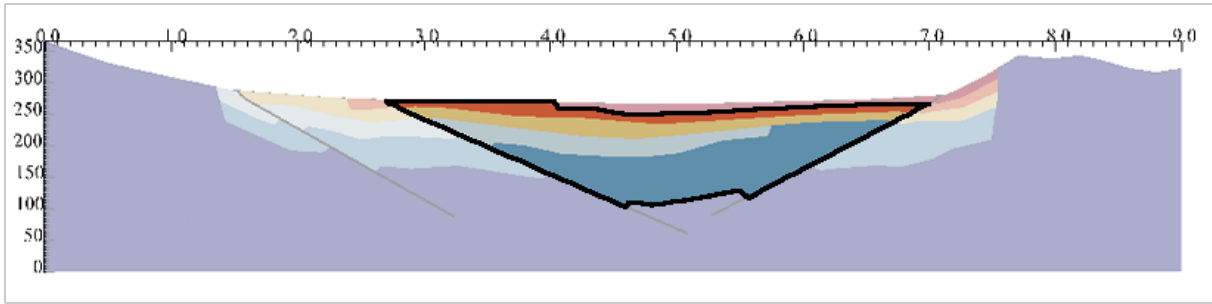
Figure 5.18. Area subject to Uniform hydraulic head change for M1 (bounded by black polygon).
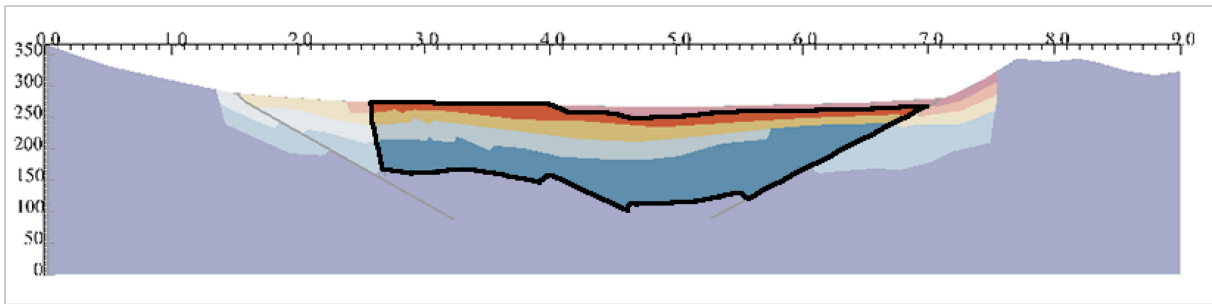
Figure 5.19. Area subject to Uniform hydraulic head change for M2 (bounded by black polygon).

As discussed above, the rationale for selecting this specific volume is based on the understanding that significant groundwater overpumping mainly occurs in the central region of the alluvial basin. In fact, overpumping is primarily driven by intensive agricultural activities, including crop and livestock production, which require significant water resources. In order to thoroughly assess the impact of this over pumping, three different scenarios of pressure change over the reference period of 8 years were investigated:

- Scenario 1 (S1): uniform pressure changes equal to -10 m, in agreement with the value recorded at the observation well PM-10 (Figure 5.2),

- Scenario 2 (S2): uniform pressure changes equal to -15 m, i.e. 50% more than the value recorded at the observation well PM-10,

- Scenario 3 (S3): uniform pressure changes equal to 20 m, twice the value recorded at the observation well PM-10.

The simulations are aimed to check if sliding can occur along fault 3 and fault 4, where earth fissures have clearly compromised the safety of structures and infrastructures in the Sarıgöl district (Figure 4.10).

5.3.1. Model 1

The geomechanical model was run for a less realistic uniform hydraulic head drawdown. Figures 5.20, 5.21 and, 5.22 shows the model outcomes in terms of land displacement, in both the vertical and horizontal directions, with the uniform drawdown as defined in S1, S2, and S3, respectively. As anticipated, the uniform drawdown results in a notable increase in vertical displacement (with respect to the values obtained using the head change provided by the RESERVOIR Project), particularly in the central basin area. This is logical when considering the geological context, as illustrated in Figure 2.7 and 2.14. These figures show that the central basin area has a deeper alluvial layer, and the majority of registered wells are used for irrigation purposes. The maximum subsidence predicted 15 cm for a groundwater hydraulic head drawdown of -10 m, 22 cm for a drawdown of -15 m, and 30 cm for a drawdown of -20 m, with an almost linear trend. The maximum horizontal displacement occurs in the vicinity of faults 2 and 3 on the surface.
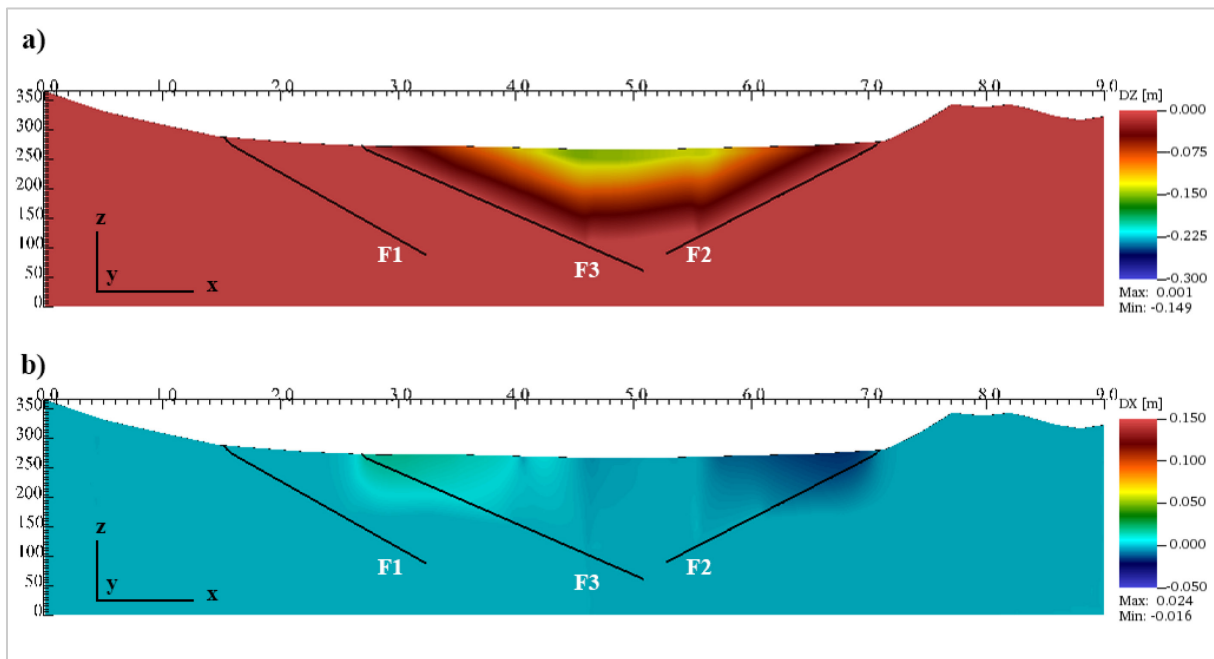
Figure 5.20. Model 1: vertical (a) and horizontal (b) displacements obtained from the geomechanical simulation applying a uniform hydraulic head drawdown of -10 m (S1) over 8 years.
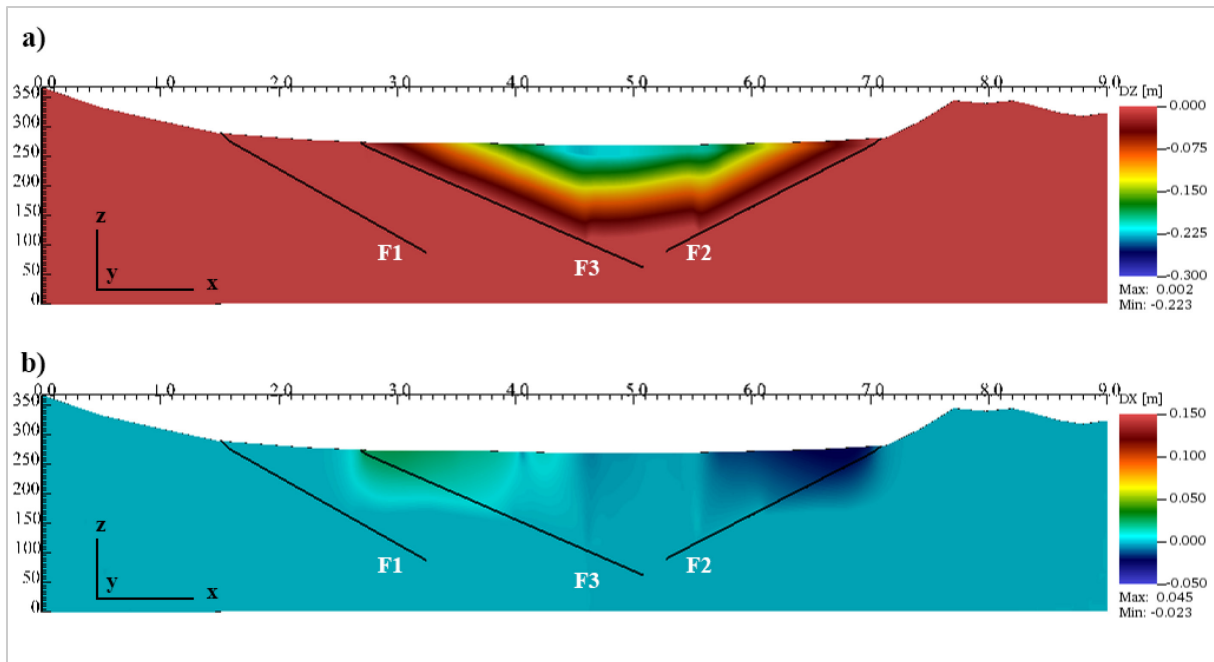
Figure 5.21. Model 1: vertical (a) and horizontal (b) displacements obtained from the geomechanical simulation applying a uniform hydraulic head drawdown of -15 m (S2) over 8 years.
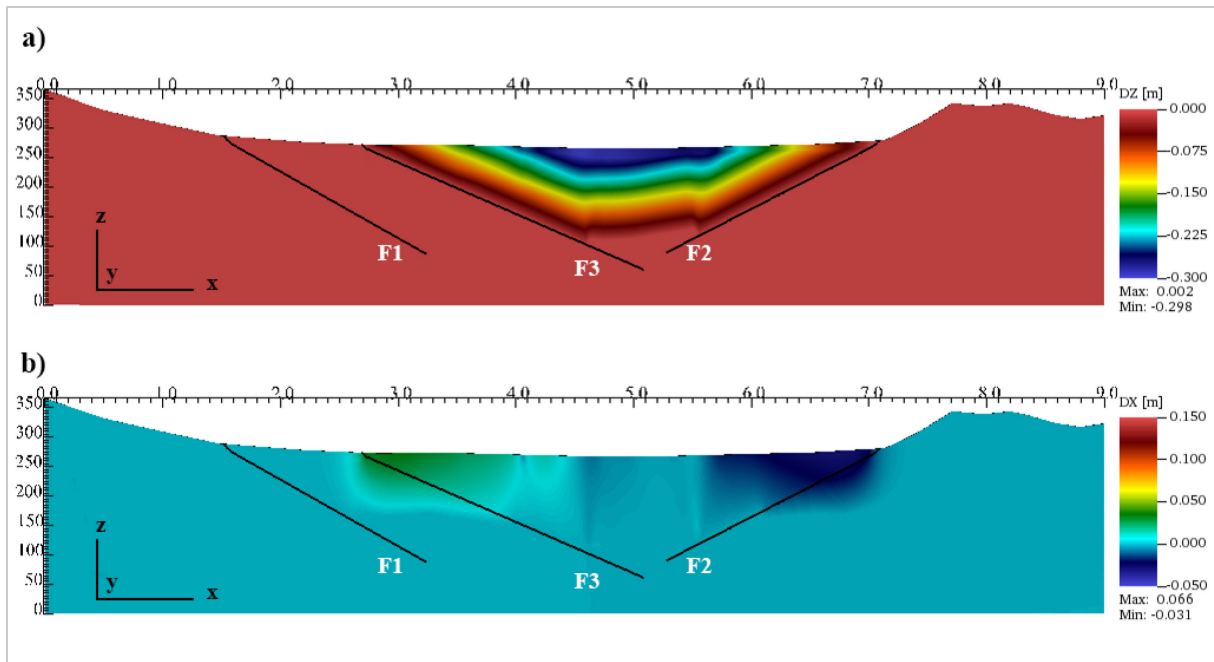
Figure 5.22. Model 1: vertical (a) and horizontal (b) displacements obtained from the geomechanical simulation applying a uniform hydraulic head drawdown of -20 m (S3) over 8 years.

As previously stated, Model 1 was constructed based on the hydogeophysical surveys, as illustrated in Figure 2.11. Accordingly, Fault 3 reaches the surface with a markedly low slope angle (approximately 6.5 degrees), which is a rare occurrence at shallow depth. Figure 5.23 provides insight into the morphology of the discontinuity down to a depth of 16 m.

It is evident that observed earth fissures (Figure 2.4) are situated near fault 3 for model 1. Consequently, to facilitate a comparative analysis of three distinct scenarios of uniform hydraulic head drawdown, four distinct points have been selected on fault 3.
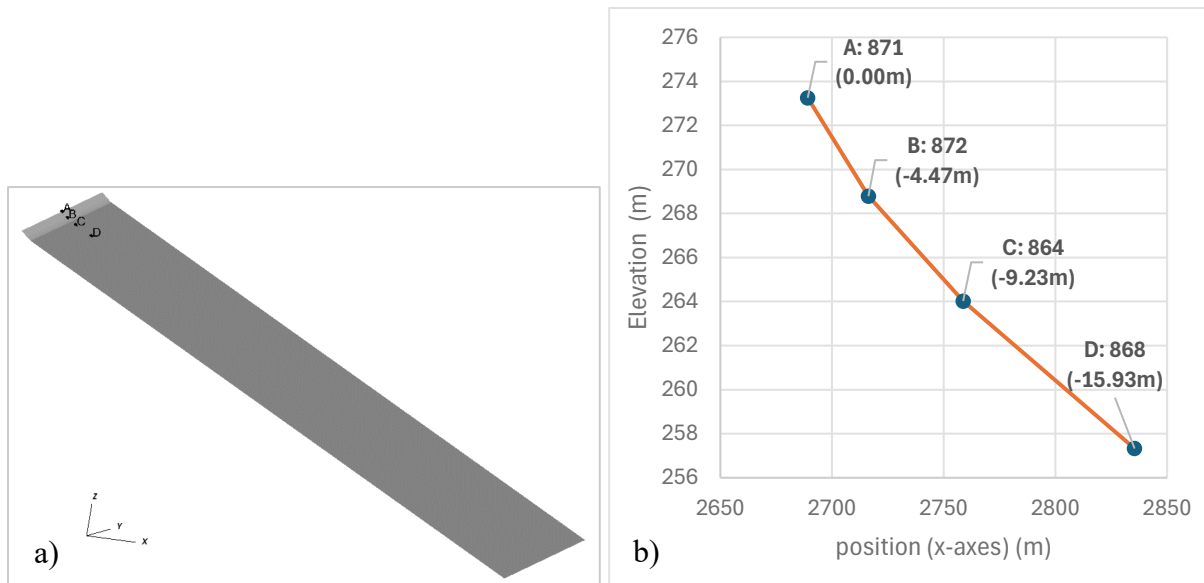
Figure 5.23. a) Location of the points on fault 3 used to compare the outcomes for the three scenarios (Model 1). Point A is located on the surface. b) Depth and ID of the selected points on fault 3.

Figure 5.24 illustrates the relationship between the limit shear stress (τ_L) and the actual shear stress (τ) over time for the three scenarios (S1, S2, and S3) at selected nodes on fault 3. The data reveal that τ_L increases with depth more significantly than τ.

In the surface plot (Figure 5.24-a), it is evident that τ exceeds τ_L from the hydraulic drawdown starting at S1 up to S2, indicating that sliding occurs earlier with an increasing pressure change. This suggests that the fault is more susceptible to sliding at lower depths, also with moderate pressure changes.

Conversely, in the deeper locations (see Figure 5.24-b, c, and d), τ does not intersect with τ_L, indicating that the shear stress remains insufficient to induce sliding under the given scenarios. However, the trend shows that with increased pressure change, τ approaches τ_L, implying an increased likelihood of fault failure as pressure changes continue to rise.

The comparison of these scenarios demonstrates that while surface portions of fault 3 may experience earlier sliding with moderate changes in hydraulic drawdown, the deeper fault requires significantly higher shear stress to reach the limit shear stress, suggesting a differential response to pressure changes based on depth.

68
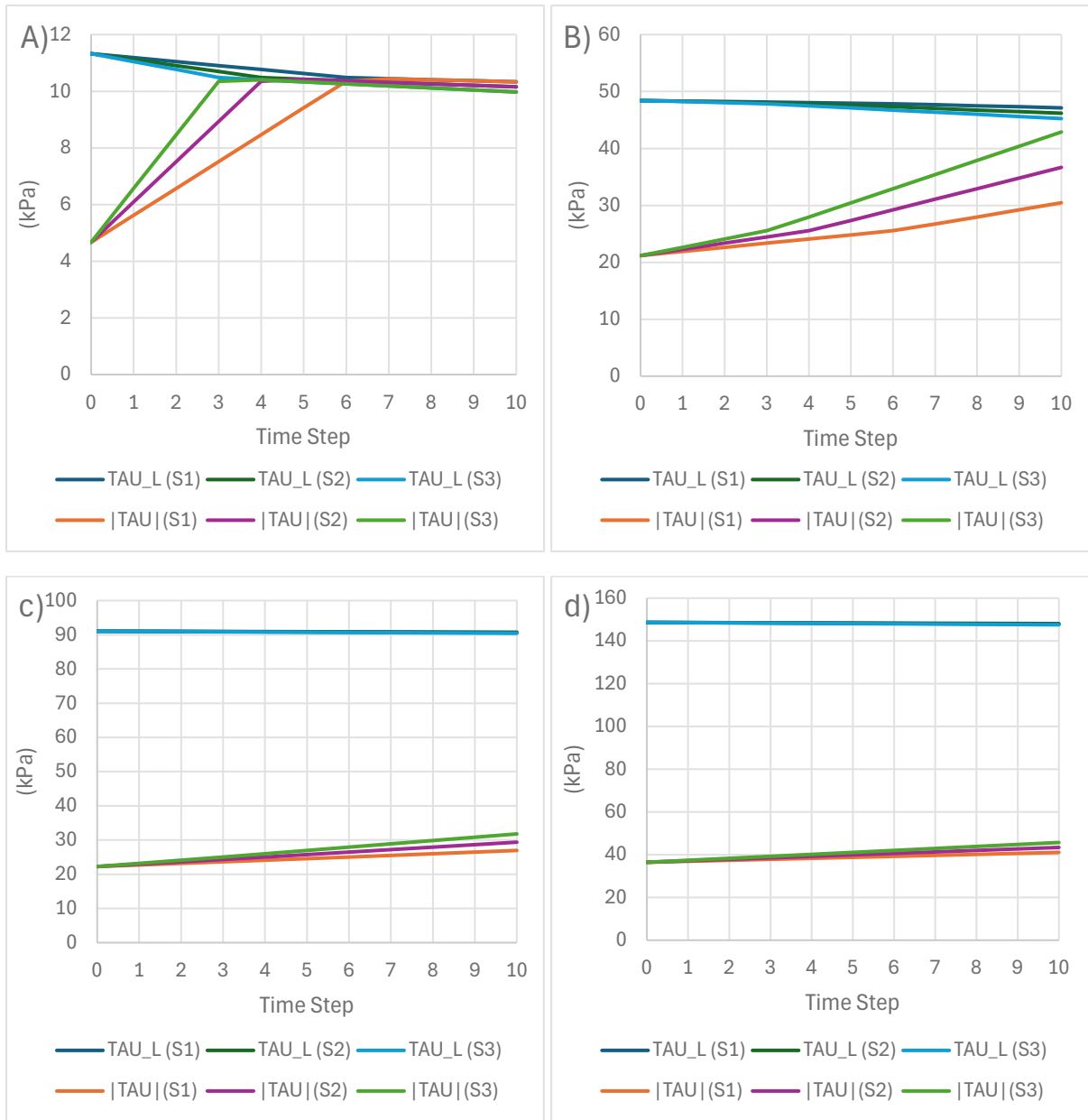
Figure 5.24. Model 1: comparison between the limit shear stress (TAU_L) - defined in Eq. (3.20)- and the actual shear stress (|TAU|) for different scenarios (S1: Scenario 1, S2: Scenario 2, and, S3: Scenario 3) at selected nodes 871 (a), 872 (b), 864 (c) and 868 (d) (see in Figure 5.23) on fault 3 .

Figure 5.25 illustrates the comparative analysis of sliding on fault 3 under the three scenariosS1, S2, and S3. The results show that sliding is observed exclusively at node 871 (on the free surface).

Figure 5.26 further quantifies this observation by depicting the relationship between sliding displacement and pressure change scenarios at node 871. This graph clearly demonstrates that sliding occurs when the actual shear stress (τ) surpasses the limit shear stress (τ_L). Additionally,

it is evident that the magnitude of sliding displacement increases with greater pressure changes, indicating a direct correlation between pressure dynamics and fault activity. This highlights how hydraulic drawdown significantly impacts fault stability and behavior, making faults more prone to sliding and displacement as pressure changes
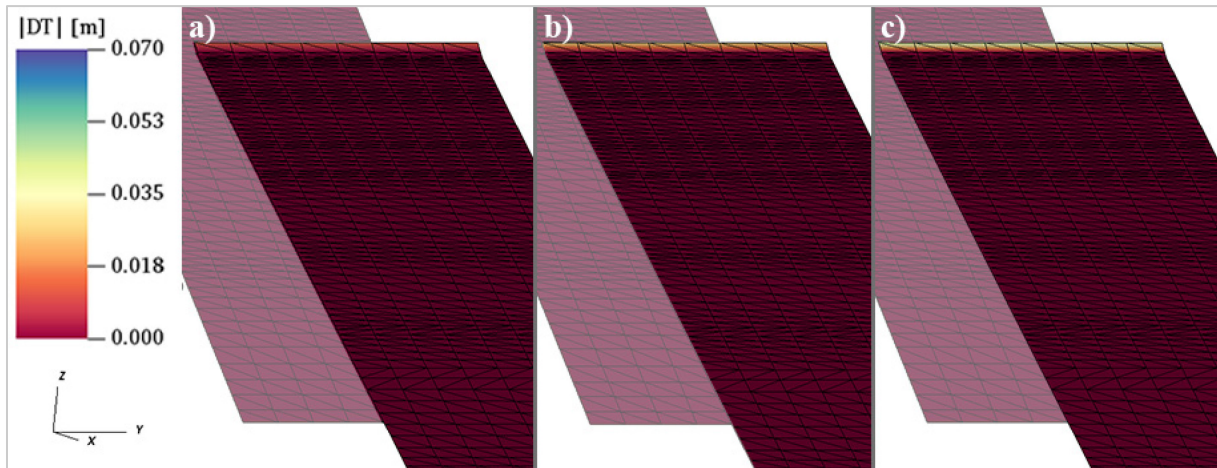
Figure 5.25. Model 1: sliding of fault 3 as obtained by the IEs for a) Scenario 1, b) Scenario 2, and c) Scenario 3.
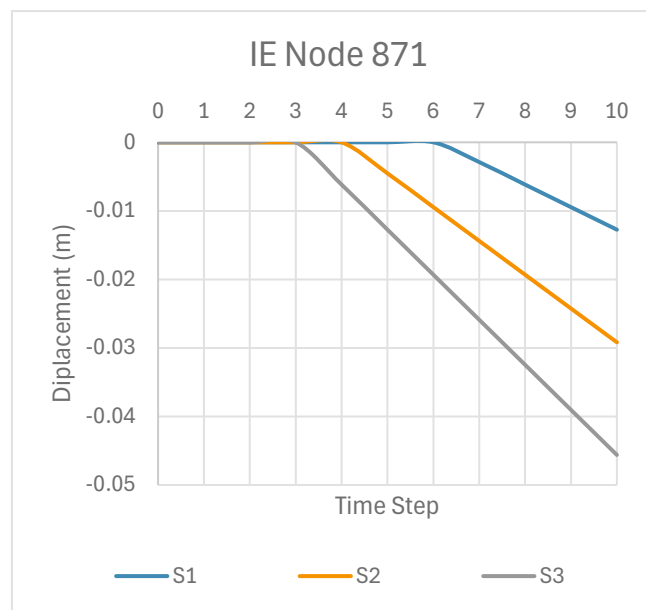
Figure 5.26. Model 1: comparison between sliding (m) and pressure change scenarios (S1, S2, and S2) for node 871 on fault 3 for model 1.

5.3.2. Model 2

Figures 5.27, 5.28 and, 5.29 show land displacement along the vertical and horizontal directions increases as obtained with the scenarios S1, S2, and S3 with the uniform drawdown of the hydraulic head applied in the area highlighted in Figure 5.19. With this second model, the maximum subsidence is 15 cm for the -10 m drawdown, 22 cm for the -15 m drawdown, and 30 cm for the -20 m drawdown of the groundwater hydraulic head. The horizontal displacements in the second model reach their maximum values around fault 4, indicating a significant localized response in that area. The computed maximum horizontal displacements amount to 8 cm, 11 cm, and 14 cm in scenarios S1, S2, and S3, respectively.
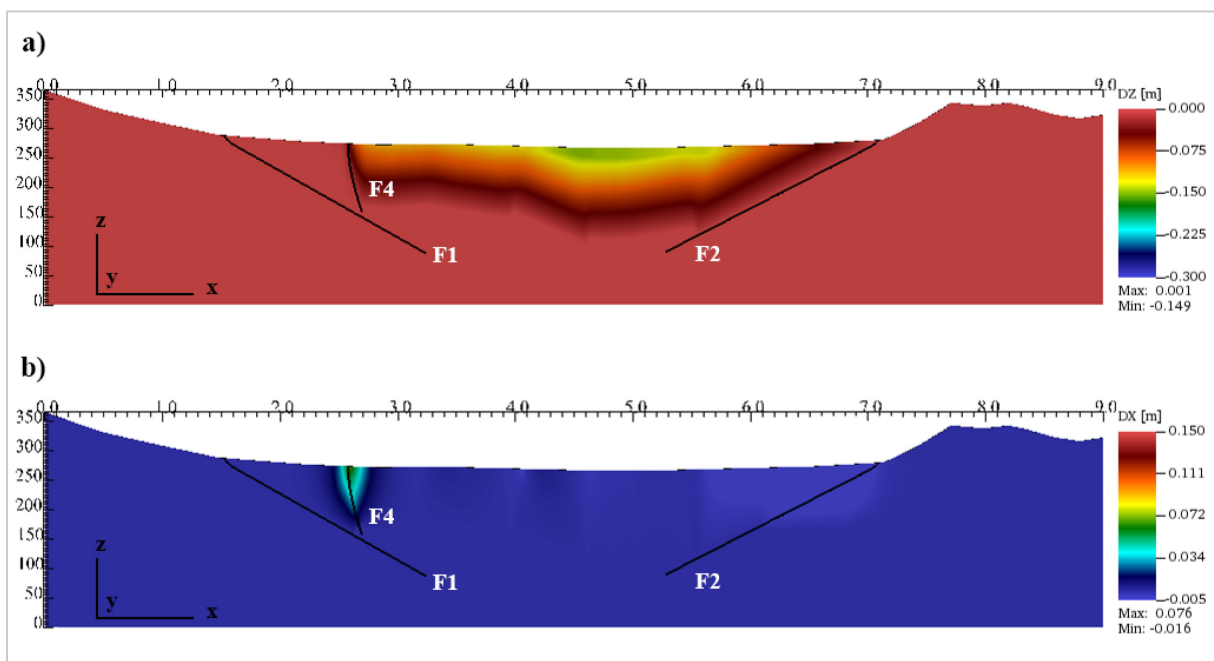
Figure 5.27. Model 2: vertical (a) and horizontal (b) displacements obtained from the geomechanical simulation applying a uniform hydraulic head drawdown of -10 m (S1) over 8 years.
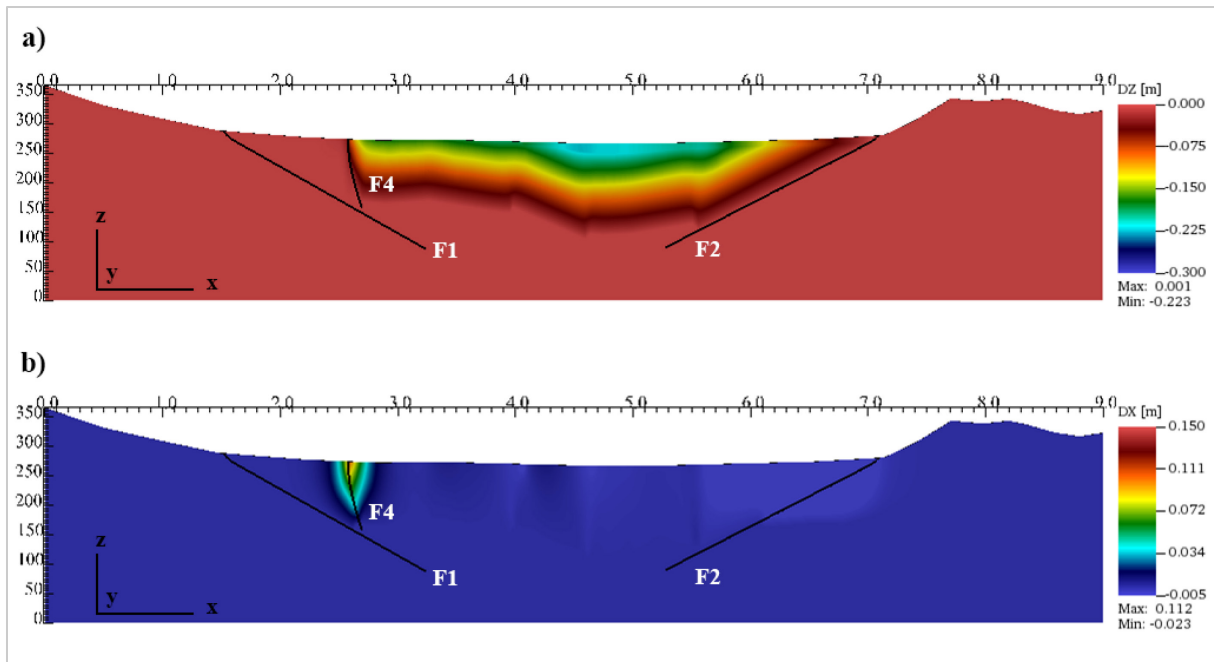
Figure 5.28. Model 2: vertical (a) and horizontal (b) displacements obtained from the geomechanical simulation applying a uniform hydraulic head drawdown of -15 m (S2) over 8 years.
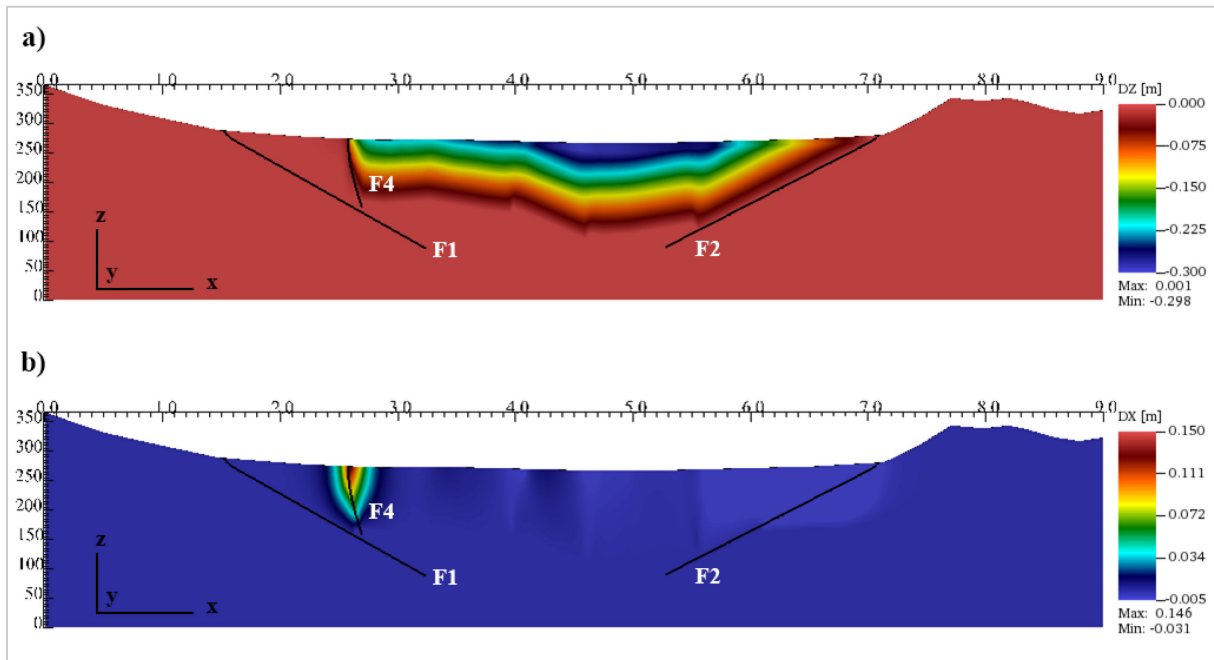
Figure 5.29. Model 2: vertical (a) and horizontal (b) displacements obtained from the geomechanical simulation applying a uniform hydraulic head drawdown of -20 m (S3) over 8 years.

In the case where fault 4 is reconstructed based on the seismic acquisitions after Ciftci et al. (2010) and Koca et al. (2011) (Figure 2.13), the fault becomes significantly steeper, with a slot of approximately 80 degrees at the land surface (Figure 5.30). As before, to facilitate a comparative analysis of three distinct scenarios of uniform hydraulic head drawdown, four distinct points have been selected on fault 4 (Figure 5.30).
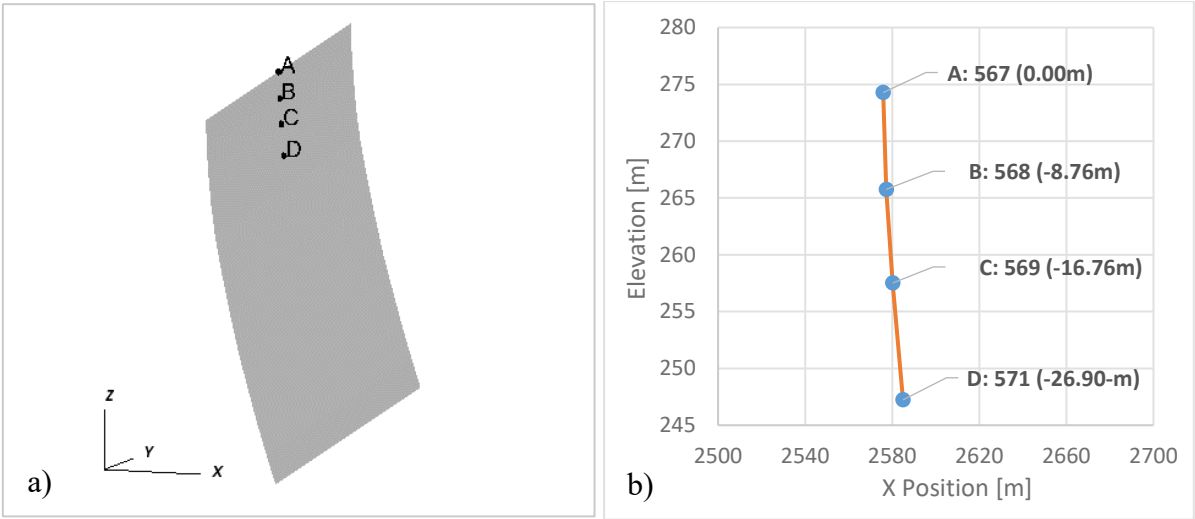
Figure 5.30. a) Location of the points on fault 4 used to compare the outcomes for the three scenarios (Model 2). Point A is located on the surface. b) Depth and ID of the selected points on fault 4.

Figure 5.31 demonstrates that with Model 2, when subjected to increased hydraulic head drop, the actual shear stress (τ) approaches the limit shear stress (τ_L) at deeper locations in comparison to those obtained in Model 1. This can be explained by considering the geometry of the fault: as the fault 4 is more vertical than fault 3, the normal stress σ_n is smaller (absolute value) at a same depth, which in turn lowers the shear limit stress τ_L based on equation (3.20). Hence, the fault is more likely to approach the shear limit stress. Moreover, the different fault dip increases the rise of actual shear stress.

The graphs demonstrate that for scenarios S1, S2, and S3, while τ intersects τ_L at shallower depths (nodes 567, 568 and 569), it approaches τ_L without intersection at greater depths, as observed in nodes 569, and 571 (Figure 5.31). This trend highlights the critical influence of hydraulic head changes on the stability of faults, particularly at shallower levels. Notice also the nonlinear behavior of τ over time at nodes 568 and 569 despite the linear variation of the

pressure heat. This is associated to the nonlinear response of the system occurring when the fissure develops (i.e., the fault is reactivated) in the overlying point.
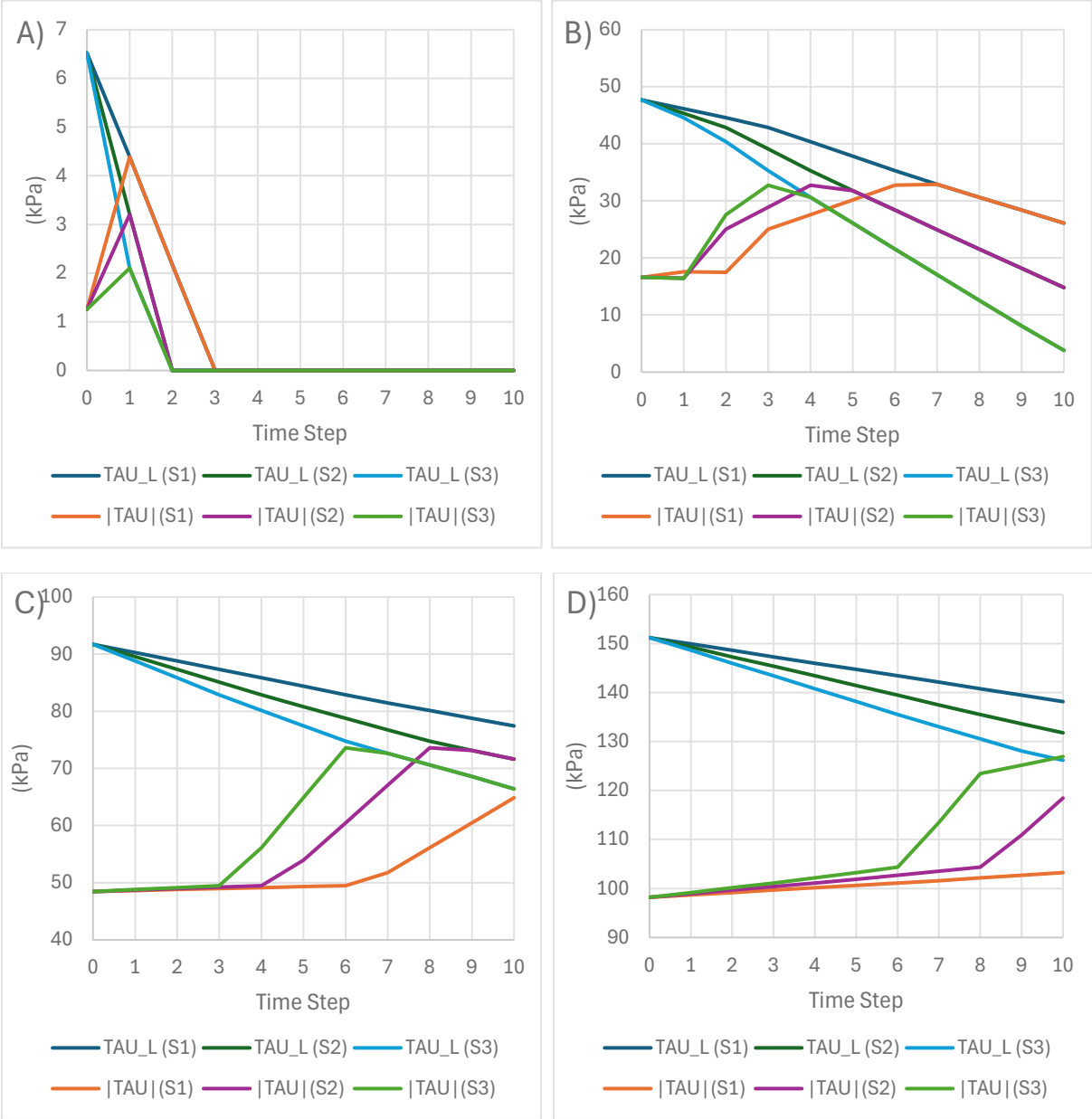
Figure 5.31. Model 2: comparison between the limit shear stress (TAU_L) - defined in Eq. (3.20)- and actual shear stress (|TAU|) for different scenarios (S1: Scenario 1, S2: Scenario 2, and, S3: Scenario 3) at selected nodes 567 (A), 568 (B), 569 (C) and 571 (D) (see in Figure 5.30) on fault 4.

Figure 5.32 shows that increased hydraulic head drawdown results in sliding occurring at shallower locations along fault 4 in Model 2.

Figure 5.33 provides a comparison of the sliding amount at different nodes as obtained with the three scenarios for Model 2. The most significant sliding is observed at surface node 567, with the magnitude of sliding decreasing with depth. At node 568, located at a depth of 8 m (Figure 5.30), the magnitude of sliding is reduced by approximately 23% compared to node 567. If we move a further 8 m deeper (node 568), the sliding magnitude is reduced by approximately 46% compared to node 567, and if we move a further 8 m deeper (node 569), there is no fault 4 that remains stacked regardless of the scenario.

These observations highlight the critical influence of hydraulic head changes on fault stability, with shallower regions of the fault becoming increasingly susceptible to sliding as the hydraulic head drawdown intensifies. The reduction in sliding magnitude with depth underscores the complex interplay between shear stress, normal stress, and fault geometry
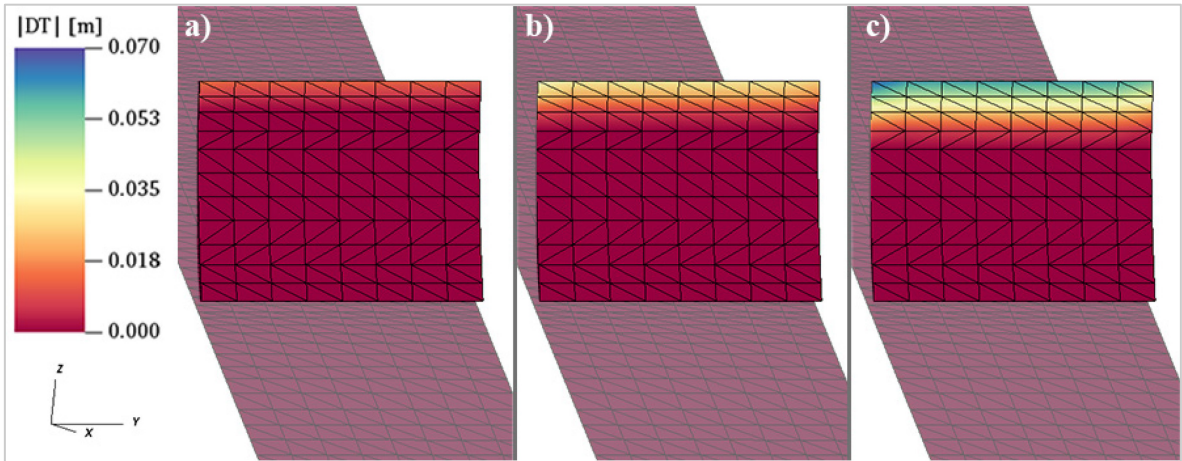
Figure 5.32. Model 2: sliding of fault 4 as obtained by the IEs for a) Scenario 1, b) Scenario 2, and c) Scenario 3.
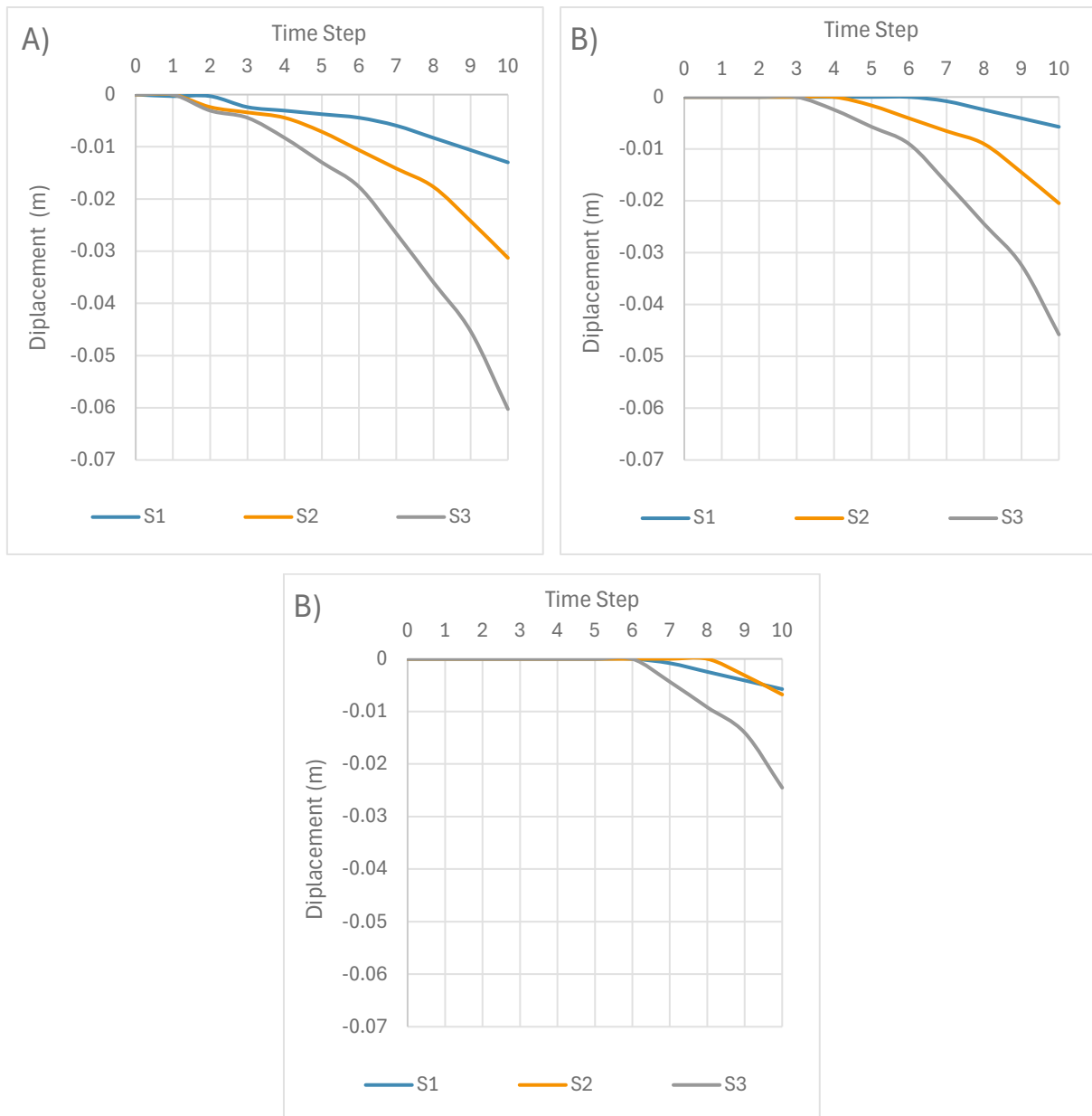
Figure 5.33. Model 2: comparison between sliding (m) and pressure change scenarios (S1, S2, and S2) for nodes 567 (A), 568 (B), and 569 (C) on fault 4.

A critical comparison between the simulated earth fissures and the field estimates obtained during our survey indicates that the fissures likely originated earlier than 2013. Given the steep inclination of Fault 4 and the continuous groundwater drawdown observed, it is plausible that the earth fissures are, at least partially, a result of aquifer overexploitation. However, this conclusion remains preliminary due to several uncertainties, including the precise timing of fissure initiation.

The qualitative agreement between the model predictions and field observations suggests a significant anthropogenic influence on fault reactivation and land subsidence. This relationship warrants further investigation to provide a more definitive understanding. Continued monitoring and more detailed studies are essential to fully elucidate the role of aquifer overexploitation in causing earth fissures in the Alaşehir-Sarıgöl sub-basin.

Chapter 6

6. Conclusions

This thesis has focused on modelling land subsidence and fault reactivation due to groundwater pumping in the Alaşehir-Sarıgöl sub-basin in Turkey using the GEPS3D simulator.

The Alaşehir-Sarıgöl sub-basin has experienced significant land subsidence, mainly due to extensive groundwater extraction for agricultural irrigation. Sentinel-1 SAR imagery revealed subsidence rates in excess of 5 cm/year from 2018 to 2021, which is alarming for both urban and agricultural areas in the region (Li, et al., 2021). The basin is controlled by a complex system of faults parallel to the main axis of the valley.

Demirtaş (2008) investigated the mechanisms behind the current surface deformations, identifying the surface faulting of the 1969 Salihli-Alaşehir earthquake, and traced older earthquakes prior to 1969. The study aimed to determine the fault mechanism and geometry, assess whether the surface fractures indicate deeper faulting in alluvial soils, and determine the width of the fault buffer zone. According to Demirtaş's research, local residents reported that these surface fractures had been present since the 1969 earthquake, with an increased rate of movement between 1998 and 2008. Since 1969, differential displacements of up to 40-60 cm have occurred along these fractures.

Figure 6.1, 6.2, and 6.3 allow a comparison between the photographs taken by Demirtaş (2008) and those taken by Yüksel (2024). At these locations, Demirtaş recorded a vertical differential displacement (fissure slip) of about 50 cm, while Yuksel up to about 100 cm. This suggests an annual sliding rate of the fissure of about 4 cm, with an increase of almost 100% over the 16-year period.

Figure 6.1. Comparison photos of land subsidence in the Sarıgöl district for same location (for photo locations, see Figure 2.3-6). a) Photographed by Demirtaş (2008). b) Photographed by Yüksel (2024).

Figure 6.2. Comparison photos of land subsidence in the Sarıgöl district for same location (for photo locations, see Figure 2.3-6). a) Photographed by Demirtaş (2008). b) Photographed by Yüksel (2024).

Figure 6.3. Comparison between photos of differential land subsidence in the Sarıgöl district for same locations (for photo locations, see Figure 2.3-7). a) Photographed by Demirtaş (2008). b) Photographed by Yuksel (2024).

After a preliminary calibration of the aquifer system compressibility, a set of initial simulations have been carried out based on the groundwater levels changes from the RESERVOIR project. No significant correlation was observed between the simulated land displacements and the InSAR data in the Sarıgöl district. The simulation results obtained with "Model 2", which is based on a geologic interpretation of seismic surveys and assumes a most likely geometry of the surface faults, indicated that the maximum land displacement did not exceed 5 cm, which corresponds to less than 1 cm/year for the simulated groundwater period between 2013 and 2021.

Subsequent simulations incorporating more likely pressure changes as derived from piezometric records and considerations on water needs in the area, have provided more interesting outcomes, with a clear link between pressure changes in the aquifer system and fault reactivation. Considering a groundwater drawdown of 10, 15 and 20 m, the geomechanical model computes an annual average land subsidence of 2.5 cm, 3.5 cm and 4.6 cm, respectively, with Model 2. These results are in good agreement with the available InSAR data and, partially, with the comparison between the localized displacement gradients derived from photos taken by Demirtaş (2008) and the thesis's author in Sarıgöl in 2024.

The decrease of aquifer pressure head due to groundwater pumping has a significant impact in terms of land subsidence and consequently on fault stability, potentially leading to fault reactivation even in the absence of significant tectonic plate movement. However, it is important to recognize that the Gediz River Basin (GRB) is one of the young and tectonic active

basins in Turkey. Based also on the modelling outcomes, it can be concluded that fault reactivation and the observable earth fissures cannot solely be attributed to anthropogenic land subsidence. Most likely, also tectonic movements are responsible for the shallow fault reactivation observed in this region.

The use of the GEPS3D simulator provided a detailed understanding of the displacement areas within the study region. Calibration of the geomechanical model with observed data ensured the reliability of the simulations and emphasized the importance of using high resolution data for model accuracy.

Data provided by the Manisa Provincial Water and Sewerage Administration show that there are 52 irrigation wells and 66 public water wells in the RESERVOIR study area (Figure 2.14). However, it is also known that there are many unregistered wells. Developing strategies to balance groundwater extraction with natural recharge rates is crucial to preventing further land subsidence and maintaining the stability of the region's geological structures. Exploring alternative water sources for irrigation and implementing advanced irrigation techniques can help reduce dependence on groundwater. In this way, subsidence caused by over-pumping can be reduced.

The following stages of this work could include but are not limited to, a sensitivity analysis of the most relevant parameters. Considering the parameters that have not yet been calibrated, the result could lead to a more accurate knowledge of the response of the subsurface to human activities. Also, the simulated hydraulic head drawdown from the groundwater flow model provided by the RESERVOIR project was not representative of the local drawdown with their simulated hydrograph. In addition, the analysis of possible fault reactivation was limited by the lack of detailed geological and seismic data from the field. With more detailed data and calibration, the relationship between fault reactivation and land subsidence may be less uncertain.

In conclusion, this study has provided valuable insights into the complex interactions between groundwater abstraction, land subsidence, and fault reactivation in the Alaşehir-Sarıgöl sub-basin. The methods and results presented here can serve as a basis for future studies and policy-making aimed at sustainable groundwater management and mitigation of subsidence-related risks.

Bibliography

Argus Holdings, L. (1997). Argus ONE User's Guide. Jericho, NJ, USA. Retrieved from http://www.argusone.com/pub/OnLineDocs/ArgusONE_UsersGuide.pdf.

Arikan, M., Hooper, A., & Hanssen, R. (2010). Radar time series analysis over. *Fringe 2009 Workshop* (pp. 1-6). ESA, Noordwijk.

AZGS, (. G. (2015). *Locations of mapped earth fissure traces in Arizona (DI-39 v. 01.29.2015). Tucson, AZ: Arizona*. Retrieved from https://azgs.arizona.edu/publication/locations-mapped-earth-fissure-traces-arizona-v-06012019

Batchelor, G. K. (1967). *An introduction to fluid dynamics.*

Biot, M. (1964). General theory of three-dimensional consolidation. *Applied physics 12, no. 2*, 155-164. doi:10.1063/1.1712886

Bonì, R., Rygus, M., Bordoni, M., Pilla, G., Meisina, C., Teatini, P., . . . Hreisha, H. (2022). *Conceptual model at the pilot sites.* RESERVOIR (Sustainable groundwater resources management by integrating earth).

Boresi, A. P., & Schmidt, R. J. (2002). *Advanced mechanics of materials.* John Wiley & Sons.

Çakmak, Ö., Duru, B., Yargıcı, A. F., Gültekin, O. Ş., Topçu, C., Yetiş, Ü., & ... Dilek, F. B. (2018). Management of groundwater quality and quantity: Gediz River Basin pilot Study. *Turkish Journal of Water Science and Management, 2(2)*, 84-109. doi:10.31807/tjwsm.423465

Carreón-Freyre, D., Cerca, M., Ochoa-González, G., Teatini, P., & Zuniga, F. R. (2016). Shearing along faults and stratigraphic joints. *Hydrogeology Journal 24(3)*, 657-674. doi: 10.1007/s10040-016-1384-0

Ciftci, N., & Bozkurt, E. (2010). Structural evolution of the Gediz Graben, SW Turkey: Temporal and spatial variation of the graben basin. *Basin Research*, 846-873. doi:10.1111/j.1365-2117.2009.00438.x

Copernicus. (2018). *Corine Land Cover*. Retrieved from https://land.copernicus.eu/pan-european/corine-land-cover/clc2018

Demirtaş, R., Yavuz, M., & Şahin, B. (2008). *Manisa ili, Sarıgöl ilçesi İmar Planı Sınırları içerisinde geçen Gediz Çöküntüsüne ait fay zonunun Paleosimolojik ve Yüzey Faylanması Tehliike Zonu Açısından Değerlendirilmesi.*

DSI. (2014). *Hydrogeological Study of the Gediz Watershed*. Retrieved from State Hydraulic Works of Turkey: https://www.dsi.gov.tr

Elçi, A., Batkan, E., Çaylak, B., Bayırtepe, M., & Ören, A. (2022). *Groundwater Flow Model for the Gediz River Basin Alluvial Aquifer (Turkiye).* Izmir.

Elçi, A., Şimşek, C., Gündüz, O., Baba, A., Acinan, S., Yıldızer, N., & Murathan, A. (2015). Simulation of groundwater flow in the Gediz River Basin. *EWRA 9th World Congress, June 1–12*. Retrieved from https://doi.org/10.13140/RG.2.1.4694.6404

Emre, Ö., Özalp, S., & Duman, T. (n.d.). *Active Fault Map Series of Turkey, 1:250,000 Scale Uşak (NJ35-8) Quadrangle. Serial Number: 11.* Ankara: General Directorate of Mineral Research and Exploration.

F., P., K.O., H., F., K., I., T., O., T., M., D., . . . R., S. (2019). Determination of the block movements in the eastern section of the Gediz Graben (Turkey) from GNSS measurements. *Journal of Geodynamics*, 38-48. doi:10.1016/j.jog.2018.11.001

Fillunger, P. (1936). *Erdbaumechanik Selbstverlag des Verfassers.* Wien.

Franceschini, A. (2014). *Formulazione lagrangiana del problema del contatto applicato a faglie geologiche.* PhD thesis, Università degli Studi di Padova.

Franceschini, A., Ferronato, M., Janna, C., & Teatini, P. (2016). A novel Lagrangian approach for the stable numerical simulation of fault and fracture mechanics. *Journal of Computational Physics, 314*, 503-521. doi:10.1016/j.jcp.2016.03.032

Gambolati, G., & Ferronato, M. (2015). *Lezioni di metodi numerici per l'ingegneria.* (Progetto, Ed.)

Gambolati, G., Gattonm, P., & Ricceri, G. (1986). Land subsidence due to gas-oil removal in layered anisotropic soils by finite elements. *Land Subsidence: Proceedings of the Third International Symposium on Land Subsidence Held at Venice, March 1984*, (pp. 29-41). Venice.

Geertsma, J. (1966). Problems of rock mechanics in petroleum production engineering. *Proceedings of the of 1st ISRM Congress*, (pp. 585-594). Lisbon, Portugal.

Goodman, R. E., Taylor, R. L., & Brekke, T. L. (1968). A Model for the Mechanics of Jointed Rock. *Journal of the Soil Mechanics and Foundations Division*, 637-659. doi:10.1061/JSFEAQ.0001133

Hacıoğlu, Ö., Başokur, A., & Diner, Ç. (2021). Geothermal potential of the eastern end of the Gediz basin, western Anatolia, Turkey revealed by three-dimensional inversion of magnetotelluric data. *Geothermics 91 (May 2020).* doi:10.1016/j.geothermics.2020.102040

Hernandez-Marin, M., & Burbey, T. J. (2010). Controls on initiation and propagation of pumping-induced earth fissures: insights from numerical simulations.,. *Hydrogeology Journal, 18(8)*, 1773-1785. doi:10.1007/s10040-010-0642-9

Herrera-García, G., Ezquerro, P., Tomas, R., B´ejar-Pizarro, M., L´opez-Vinielles, J., Rossi, M., . . . Wang, H. (2021). Mapping the global threat of land subsidence. *Science 371*, 34–36. doi:10.1126/science.abb8549

Jachens, R. C., & Holzer, T. L. (1979). Geophysical investigations of ground failure related to groundwater withdrawal - Picacho Basin, Arizona. *Ground Water 17(6)*, 574-585. doi:10.1111/j.1745-6584.1979.tb03358.x

Jachens, R. C., & Holzer, T. L. (1982). Differential compaction mechanism for earth fissures near Casa Grande, Arizona. *Geological Society of America Bulletin, 93*, 998-1012. doi:10.1130/0016-7606(1982)93<998:DCMFEF>2.0.CO;2

Jaeger, J. C., Cook, N., & Zimmerman, R. (2009). *Fundamentals of rock mechanics.* John Wiley & Sons.

Jha, B., & Juanes, R. (2014). Coupled multiphase flow and poromechanics: A computational model of pore pressure effects on fault slip and earthquake triggering. *Water Resources Research*, 3776 - 3808. doi:10.1002/2013WR015175

Koca, M., Sözbilir, H., & Uzel, B. (2011). Sarıgöl fay zonu boyunca meydana gelen deformasyonların nedenleri üzerine bir araştırma. *Jeoloji Mühendisliği Dergisi*, 151-174.

Li, Y. (2024). *Uncertainty quantification of the continuous and discontinuous geomechanical response in over-exploited aquifers.* PhD thesis, Università degli Studi di Padova.

Li, Y., Teatini, P., Yu, J., Franceschini, A., Frigo, M., Zoccarato, C., & Ye, S. (2021). Aseismic Multifissure Modeling in Unfaulted Heavily Pumped Basins: Mechanisms and Applications. *Water Resources Research, 57*. doi:10.1029/2021WR030127

Liu, M., Suo, S., Wu, J., Gan, Y., Hanaor, D. A., & Chen, C. Q. (2019). Tailoring porous media for controllable capillary flow. *colloid and interface science, 539*, 279-387. doi:10.1016/j.jcis.2018.12.068

Logan, D. L. (2011). *A first course in the finite element method.* Thomson.

McNaught, A. D. (1997). *Compendium of chemical terminology.* Oxford: Blackwell Science.

Navarro-Hernández, M., Tomás, R., Valdes-Abellan, J., Bru, G., Ezquerro, P., Guardiola-Albert, C., & ... & Rygus, M. (2023). Monitoring land subsidence induced by tectonic activity and groundwater extraction in the eastern Gediz River Basin (Türkiye) using Sentinel-1 observation. *Engineering Geology*, 237. doi:10.1016/j.enggeo.2023.107343

Ochoa-González, G., Carreón-Freyre, D., Franceschini, A., Cerca, M., & Teatini, P. (2018). Overexploitation of groundwater resources in the faulted basin of Queretaro, Mexico: 3D defermation and stress analysis. *Engineering Geology, 245*, 192-206. doi:10.1016/j.enggeo.2018.08.014

Özkaymak, Ç., Sözbilir, H., Tiryakioğlu, İ., & Baybura, T. (2017). Bolvadin'de (Afyon-Akşehir Grabeni, Afyon) Gözlenen Yüzey Deformasyonlarının Jeolojik, Jeomorfolojik ve Jeodezik Analizi. *Bülteni/Geological Bulletin of Turkey 60(2)*, 169–189. doi:10.25288/tjb.302914

Poyraz, F., & Hastaoğlu, O. (2020). Monitoring of tectonic movements of the Gediz Graben by the PSInSAR method and validation with GNSS results. *Arabian Journal of Geosciences 13*, 1-11. doi:10.1007/s12517-020-05834-5

Selim, H., & Yanik, G. (2009). Development of the Cambazlı (Turgutlu/MANISA) fissure-ridge-type travertine and relationship with active tectonics, Gediz Graben, Turkey. *Quaternary International*, 157-163. doi:10.1016/j.quaint.2008.04.009

Settari, A. A. (2008). Numerical techniques used for predicting subsidence due to gas extraction in the Northern Adriatic. *Petroleum Science and Technology, 26(10–11)*, 1205-1223. doi:10.1080/10916460701833889

Seyitoğlu, G., Çemen, İ., & Tekeli, O. (2000). Extensional folding in the Alaşehir (Gediz) graben, western Turkey. *Geological Society 6 (157)*, 1097–1100. doi:10.1144/jgs.157.6.1097

Sözbilir, H. (2002). Geometry and origin of folding in the Neogene sediments of Gediz graben, Western Anatolia, Turkey. *Geodin. Acta (5-6)*, 277-288. doi:10.1080/09853111.2002.10510761

Steeb, H., & Renner, J. (2019). Mechanics of Poro-Elastic Media: A Review with Emphasis on Foundational State Variables. *Transp Porous Med 130*, 437–461. doi:10.1007/s11242-019-01319-6

Tatar, O., Poyraz, F., Gürsoy, H., Cakir, Z., Ergintav, S., Akpinar, Z., . . . Yavasoğlu, H. (2012). Crustal deformation and kinematics of the Eastern part of the North Anatolian Fault Zone (Turkey) from GPS measurements. *Tectonophysics 518–521*, 55-62. doi:10.1016/j.tecto.2011.11.010

Teatini, P., Castelletto, N., Ferronato, M., Gambolati, G., Janna, C., Cairo, E., & Bottazzi, F. (2011). Geomechanical response to seasonal gas storage in depleted reservoirs: A case study in the Po River basin, Italy. *Journal of Geophysical Research: Earth Surface*, 116(F2). doi:10.1029/2010JF001793

Teatini, P., D., B., & G., G. (2000). Water-gas dynamics and coastal land subsidence over Chioggia Mare field, northern Adriatic Sea. *Hydrogeol. J., 8(5)*, 462-469. doi:10.1007/s100400000092

Terzaghi, K. (1925). Principles of Soil Mechanics. *Engineering News-Record*, 699-703.

Terzaghi, K. (1943). Calculating the permeability of the clay from the course of the hydrodynamic stress. appearances. *Meeting area Academic science Math. Natural Science Cl. Dept. 2A*, (pp. 105-124). Vienna.

Terzaghi, K. (1943). *Theoretical soil mechanics.* New York.

Üner, S., & Dogan, D. (2021). An integrated geophysical, hydrological, thermal approach to finite volume modelling of fault-controlled geothermal fluid circulation in Gediz Graben. *Geothermics 90.* doi:10.1016/j.geothermics.2020.102004

Verruijt, A. (1969). Elastic Storage of Aquifers. In R. D. Wiest, *Flow through Porous Media* (pp. 331-376). New York: Academic Press.

Ye, S., Franceschini, A., Zhang, Y., Janna, C., Gong, X., Yu, J., & Teatini, P. (2018). A novel approach to model earth fissure caused by extensive aquifer exploitation and its application to the Wuxi case, China. *Water Resources Research, 54*, 2249-2269. doi:10.1002/2017WR021872

Yılmaz, B., & Atmaca, K. (2017). Efficiency of Irrigation Associations in Gediz Basin, Turkey. *Politeknik Dergisi, 20(4)*, 837-842. doi:10.2339/politeknik.369025

Yılmazer, S., Pasvanoglu, S., & Vural, S. (2010). The relation of geothermal resources with young tectonics in the Gediz Graben (West Anatolia) and their hydrogeochemical analyses. *Proceedings world geothermal congress*, (pp. 1-10).